UNIVERSITÀ DEGLI STUDI DI PADOVA

Facoltà di Scienze MM.FF.NN.

Dipartimento di Fisica “G. Galilei”

TESI DI LAUREA IN FISICA

Design and construction of a microdosimetric detector for the International Space Station (ISS)

Relatore: Dottoressa Laura De Nardo

Correlatore: Dottore Davide Moro

Laureando: Guido Sbrogiò

Matricola: 603642

Anno Accademico 2010-2011

Contents

Chapter 6 - Detector construction and assembly

Introduction

Since the beginning of the earlier space manned missions the protection against radiation has become of primary importance in the planning of their length and orbital position. Outside the protective shield of the Earth's atmosphere the space is imbued with a complex field of radiation arising from galactic and extra-galactic sources, sun's physical processes and interaction between these and the Earth's magnetic field. The radiation field is composed of a complex mixture of particles and photons, ranging from few keV to 10^{12} MeV and even beyond. Particles are present in form of neutrons, electrons, protons and a vast variety of ions, from alpha particles to heavy ions nuclei. Space exploration is shifting ever more outside the envelope of Earth's magnetic field, directing its programs towards interplanetary space. The incoming take off of the first manned expedition to Mars has posed serious problems about the possibility to send humans aboard spacecraft in long missions without that they would suffer critical diseases and sickness during and afterward the mission. The Apollo missions ventured away from the Earth not more than 12 days, proposed missions to the moon in the coming future could last up to 200 days, and a possible mission to Mars could last up to 3 years, and it would lead to a total-body dose exposure of about 1-2 Sv.

The quantity of exposure is not the only critical factor because the biological effect of the radiation is strongly correlated to the type of radiation. For example we know that for the same dose neutrons are much more biological damaging than high-energy photon radiation. Thus in a variable complex field of ions, protons and neutrons is very difficult to investigate each contribution, given also the high range of energy considered, and therefore to obtain the biological effectiveness of each kind of radiation. Besides the risk assessment has been documented only by epidemiological data from radiation workers and patients exposed to low LET radiation such as γ-rays or x-rays, and from survivors of the atomic bomb in Japan exposed to neutrons. But we have no data about exposure to high energy protons and high charge and energy ions, and risk estimates for exposure to galactic cosmic rays and trapped protons in Low Earth Orbit (LEO) are thus entirely based on models and biophysical calculations. It is not possible

therefore know surely what are the real biological effects and rates of mortality for the bulk of the radiation spectra present in the space. Space agencies are thus interested to obtain more data about the biological effectiveness of space radiation for the safety of their crews aboard spacecraft and space stations.

Sun's solar cycle modulates the solar wind flux and this respectively modulates the galactic flux of cosmic rays, which are the major components of hazard for the astronauts in the Low Earth Orbit. Moreover solar wind affects directly the intensity of the Earth's magnetic field and the composition of the magnetosphere. This interconnected mechanism produces the radiation environment in which astronauts work every day in space stations or shuttles. Since it is variable with time and position and since it is a complex field, there are serious difficulties in the understanding of the biological injuries that it produces. Dosimetry is becoming thus a major disciplines in the survey of radiation environment aboard and outside the spacecraft. NASA and ESA require the absorbed dose *D* and equivalent dose *H* to be measured in order to provide new and specific shielding structures for spacecraft and new technologies for human radiation protection. In this contest arises the ESA project called EuCPAD (European Crew Personal Active Dosemeters) with the purpose of investigate and monitor the radiation environment inside the Columbus module of the International Space Station. It consists of personal dosemeters worn by astronauts, each one composed by a stack of five different passive radiation sensors, and a rack unit with a spherical Tissue-Equivalent Proportional Counter (TEPC), an active detector able to measure in real-time the absorbed dose of complex radiation field composed of high and low LET radiation. TEPCs can perform microdosimetric measurements of energy deposition due to a single particle, as it is able to simulate tissue volumes of micrometric size. Consequently a TEPC gives an absolute and direct measurement of the ionizations occurring inside the volume considered.

This thesis concerns just with the study and construction of a prototype of a spherical TEPC for ESA's EuCPAD project. AIT (Austrian Institute of Technology) in collaboration with the Department of Physics of Padova and CINEL and Tre-C industries have developed a new spherical TEPC adapted for the use in space and that will be inserted in the EuCPAD project. It can detect any kind of ionizing radiation, neutrons, protons, photons, measuring lineal energy in the range of

0.2-2000 KeV/μm. This thesis aim to describe the design, the first work of construction and characterization of a TEPC for the EuCPAD project.

Chapter 1 gives a general overview of the radiation environment in the solar system and more specifically in LEO, explaining what are the major sources of radiation hazard for the astronauts in spacecraft, their temporal variation and modulation.

Chapter 2 presents what is the biological effect of radiation and how is possible to determine its quality. Then it is presented an overview of the dosimetry instruments aboard ISS and of dosimetry measurements made in LEO by past spacecraft missions and aboard space stations.

Chapter 3 introduces microdosimetry and explains its theoretical basis. It is explained also how works a TEPC and its characteristics.

Chapter 4 describes the experimental set-up, the electronic chain and the acquisition system used, and how generate a microdosimetric spectra.

Chapter 5 deals with the design and study of the TEPC, pointing out the specifics of the TEPC gas chamber and the TEPC electronic, and considering how the constraints imposed by the use in a space environment and by space radiation affect the whole design.

The Chapter 6 concerns with the construction phase of the EuCPAD TEPC. It is presented a mechanical design overview and the first part of construction and testing. The discussion does not fulfill the entire process of construction since some delays with the project have occurred.

CHAPTER I

The space radiation environment

1.1 - The space radiation around Earth and its sources

The Earth's atmosphere enables a massive protection against radiation that comes from the space, and people that live at low altitude are very low affected by it. All the radiation that hits the atmosphere produces streams of secondary particles, called *particle shower*s. The primary particles are more commonly called *cosmic rays* and when they approach the atmosphere they collide with the nuclei of the gases present, mainly oxygen and nitrogen. Increasing with altitude the atmosphere becomes ever more tenuous, and at about 100 km the density scale of about six order of magnitude, being at sea level ~ 1.2 kg/m^3. The atmosphere has a mass of about $5 \cdot 10^{18}$ kg, three quarters of which is within about 11 km of the surface. The Karman line lies at ~100 km and is often regarded as the boundary between atmosphere and outer space. In Low Earth Orbit (LEO) the protective shell of the atmosphere become negligible (LEO is defined as the shell confined between the Earth's surface up to an altitude of 2,000 km), and even in the lower LEO, where the International Space Station (ISS) and in general the shuttles have their orbits (ISS orbit lies in average at 390-400 km above Earth's surface), one can neglect the effect of the atmosphere's gases.

In the following we shall see what are the sources of the radiation that come to the Earth and what are the processes implied, whereas in the next paragraphs we shall see what modules the flux of cosmic rays that arrives. We will see besides that Earth's magnetic field plays a central role in protection against cosmic rays in LEO but conversely it produces another phenomenon that creates further problems and risks for the astronauts in shuttles and space stations, the Van Allen radiation belt. The key point is to understand how all these aspects interact among them, producing a space-dependence of the radiation environment, and how the Sun's physical processes fuel moreover a time-dependent variation which

contributes to our ignorance of the total radiation effect on astronauts.

1.1.1 - Galactic cosmic rays

All the particles that impinge on the atmosphere, independently of their origin are called cosmic rays. Cosmic rays are a complex mixture of protons, neutrons, electrons, ions and high energy photons. Once they collide with the atmosphere secondary particles as muons, pions, positrons and even neutrinos are produced, and of course photons by electromagnetic cascades initiated by decay of neutral and charged mesons. G*alactic cosmic rays* (GCRs) are, instead, the component of cosmic rays that has extra-solar origin.

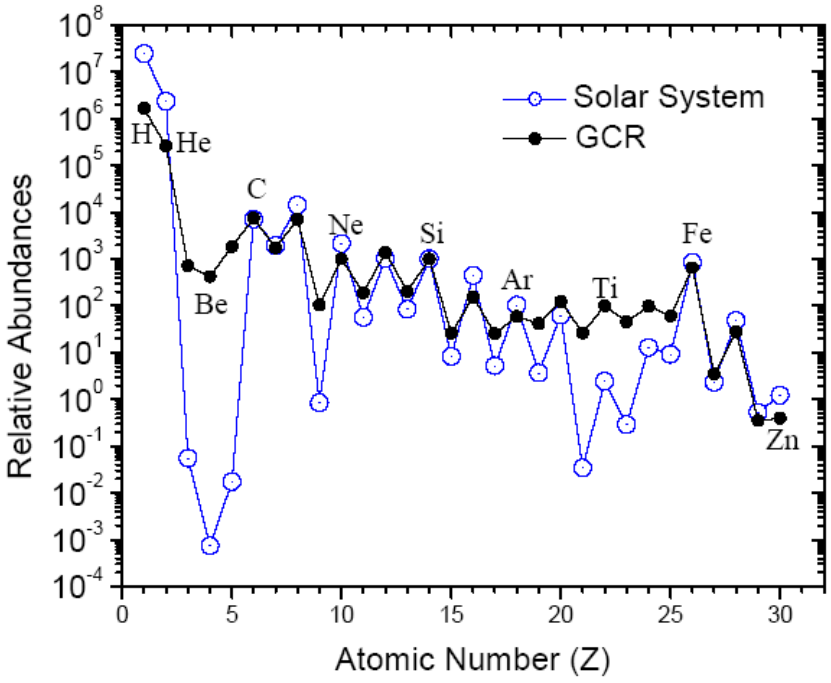

Figure 1.1 - GCRs relative abundance in comparison with that of the Solar System - NASA www.nasa.gov

It is not yet clarified by which source or sources they have their origin, but given that their energy spectra ranges from tens up to 10^{12} MeV (but in the high-energy tail of the distribution even higher), it is supposed that only very energetic events like supernovae explosion or active galactic nuclei processes could produce

particles of such energy. The GCRs spectra is composed of 85% protons, 12% helium ions, 1% of heavy ions from Li to U and the remaining of electrons and positrons. In the figure 1.1 the elemental abundance of GCRs at solar minimum is showed. The distribution is believed to be isotropic, at least inside the solar system. Solar wind act as a shield against GCRs, and there are observations made by the Voyager 2 probe that in the outer border of the Heliosphere GCRs flux is higher than in the region near the Sun [Burlaga, 1991]. The Interstellar Boundary Explorer (IBEX) has collected other data of this dependence of the GCRs flux in which is showed how the fraction of incident GCRs is reduced in the interior of the Heliopause, as showed in figure 1.2 (Heliopause is the border between the Heliosphere and the intergalactic space, where the pressure of the solar wind and of the interstellar wind is equal).

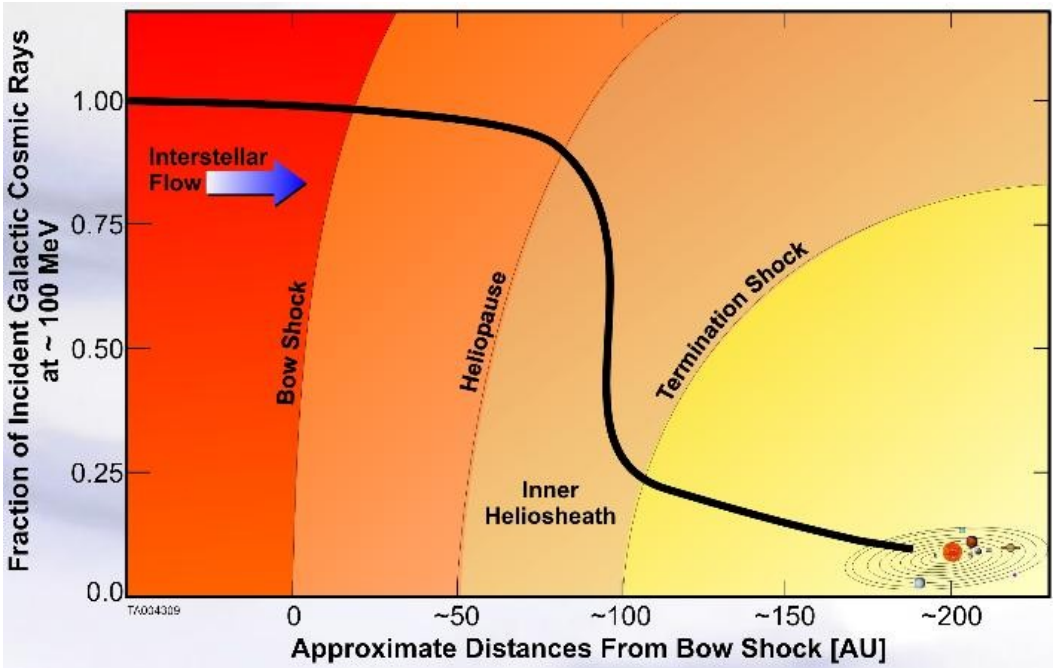

Figure 1.2 - GCRs flux modulation by solar wind – IBEX www.ibex.swri.edu

In proximity of LEO GCRs are affected by Earth's magnetic field. Since GCRs are composed by charged particles, they tend to follow the lines of the geomagnetic field. The geomagnetic field lines point towards the Earth's surface near the poles,

whereas are parallel along the equator. Therefore most of GCRs particles are deflected away at low terrestrial latitudes and funnelled ever closer to the poles, depending on the charge.

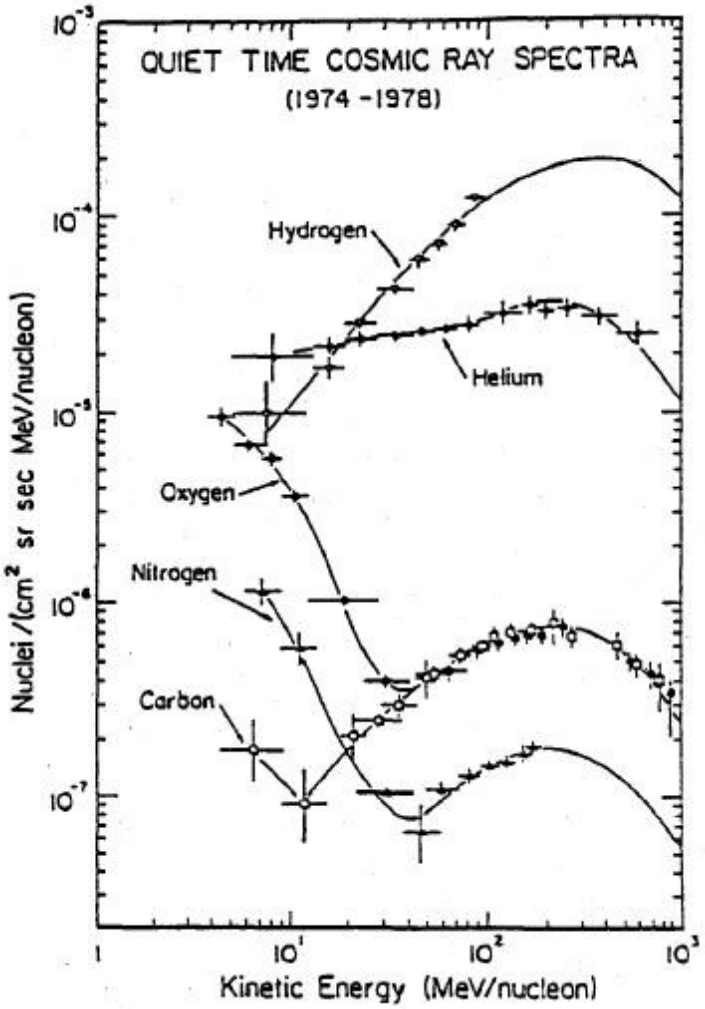

Figure 1.3 - GCRs flux during solar minimum for several elements [Feynman, 1996]

For this reason a spacecraft orbiting in LEO receives the most of GCRs in proximity of the poles. Spacecraft in LEO on low inclination orbit, about 30°, will not receive the lowest component in energy of GCRs, as the magnetic field lines funnel the lower energy particles toward the poles. Nevertheless the higher

component in energy penetrates the field lines and for this kind of radiation the Earth's magnetic field is not more a sufficient shield.

In figure 1.3 the typical flux of GCRs in the low energy range for various types of elements, during the solar minimum at 1 AU is showed (Astronomic Unit it's about $1{,}496{,}597 \cdot 10^{11}$m) [Feynman, 1996].

1.1.2 - Solar particle events

The solar wind is a stream of plasma of charged particles emitted from the corona of the Sun and consists of 95% electrons and protons, 5% alpha particles and a light trace of heavy ions. These particles have in general energy that range from few eV to 1 keV, with the flux that changes along with the solar cycle. The total number of particles carried away from the Sun by the solar wind is about $1.3 \cdot 10^{36}$ per second. Solar wind is not critic for the space travel given its low energy, and the current aluminium shielding of the spacecraft is able to protect the astronauts from its influence. We shall see in the following that nevertheless it has a strong influence in the shaping of the Earth's magnetic field and in the creation of the Van Allen radiation belt, which instead causes serious problem for the crews in spacecraft in LEO. On the other hand the Sun can produce impulsive events of radiation that can be very hazardous. These processes named *solar particle events* (SPEs) are not completely correlated with a precise source, but it has been largely accepted that they are generally associated with *coronal mass ejections* and *solar flares*. The major contribution of SPEs to the spectra of radiation detectable in spacecraft range from about 1 to 500 MeV and the composition resembles that of solar wind (which in turn has a composition similar to that of the Sun). From a space radiation health perspective we are most interested to protons, due to their major abundance and energy in the SPEs spectrum, and hereafter we will refer always to protons fluxes and fluences each time we deal with SPEs. There is a strong correlation between SPEs and the solar maximum. Solar maximum is defined by a strong activity of the Sun and an increment of number of solar spots during the 11-years solar cycle (figure 1.4). The active period extends from 2 years before the year of solar maximum to 4 years after.

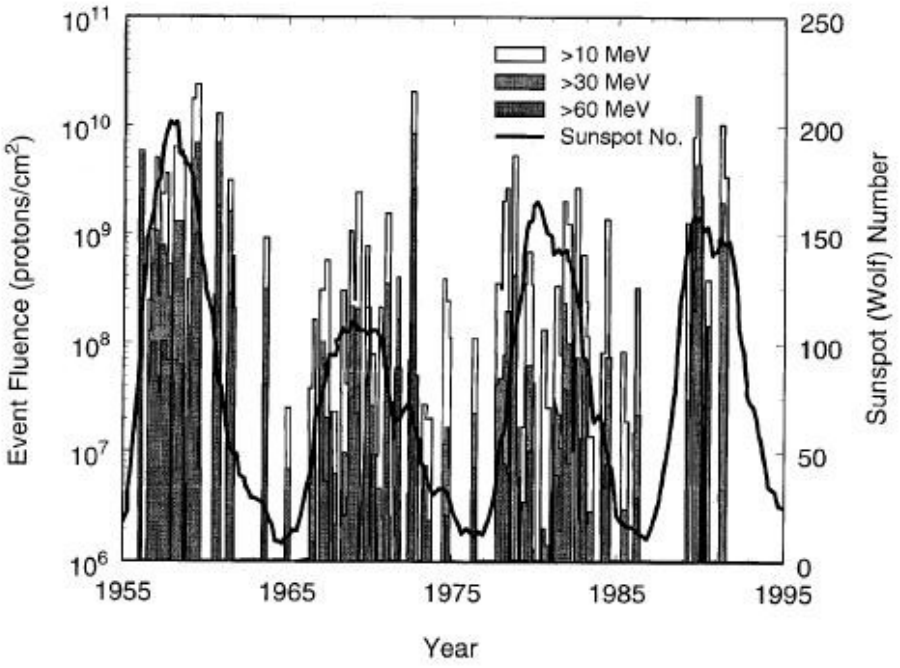

Figure 1.4 - Major SPEs detected in the last four solar cycle. It is evident like SPEs are strictly correlated with the Sunspot number[1] [Benton, 2001]

Data from SPEs usually are given as a fluence, that is a flux of particle per area integrated per a given period of time (usually the entire lifespan of the event) Although during a solar cycle the number of SPEs is variable, in average we can expect around 50 events for each period between two solar minimum. Fluences observed can be very variable, but we can set a bond of $1.5 \cdot 10^9$ protons/cm^2 with E > 10 MeV. Bigger fluences are very rare, but observed at least once - SPE of october 1989 has reached a fluence of about $1.3 \cdot 10^{10}$ protons/cm^2 [Feynman, 1996]. We can notice however that SPEs with a fluence greater than $3 \cdot 10^7$ protons/cm^2 with E > 10 MeV comprise only 1% of the total.

One can classify in practice two classes of SPEs with energy above 5 MeV,

1 The Sunspot number is counted by the Wolf number, which is a quantity that measures the number of sunspots and groups of sunspots present on the surface of the Sun. The Wolf number N_F of sunspots is $N_F = k(10g+s)$, where s is the number of individual spots, g is the number of sunspot groups and k is a factor depending by location and instrumentation.

corresponding to two different types of observed X-ray solar flares, that is *gradual SPE* and *impulsive SPE*. The gradual SPEs are associated to coronal mass ejections and the X-ray peak that occurs has a constant decay over many hours; on the other hand impulsive SPEs present a sharp peak (figure 1.5).

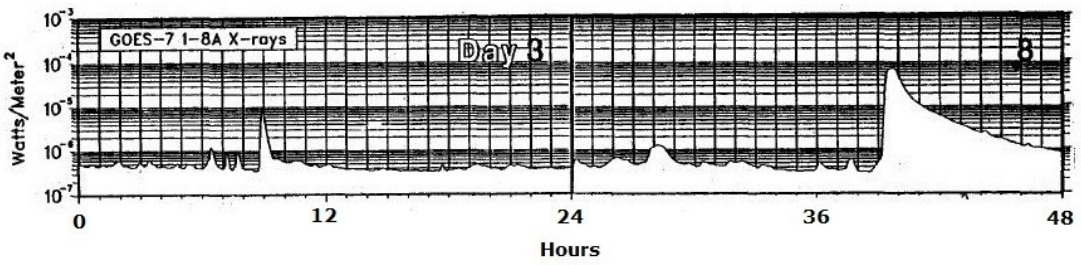

Figure 1.5 - X-ray events from SPEs. The vertical line counts the hours for each step. The spectra in the left show an impulsive event and the right one a gradual event [Feynman, 1996]

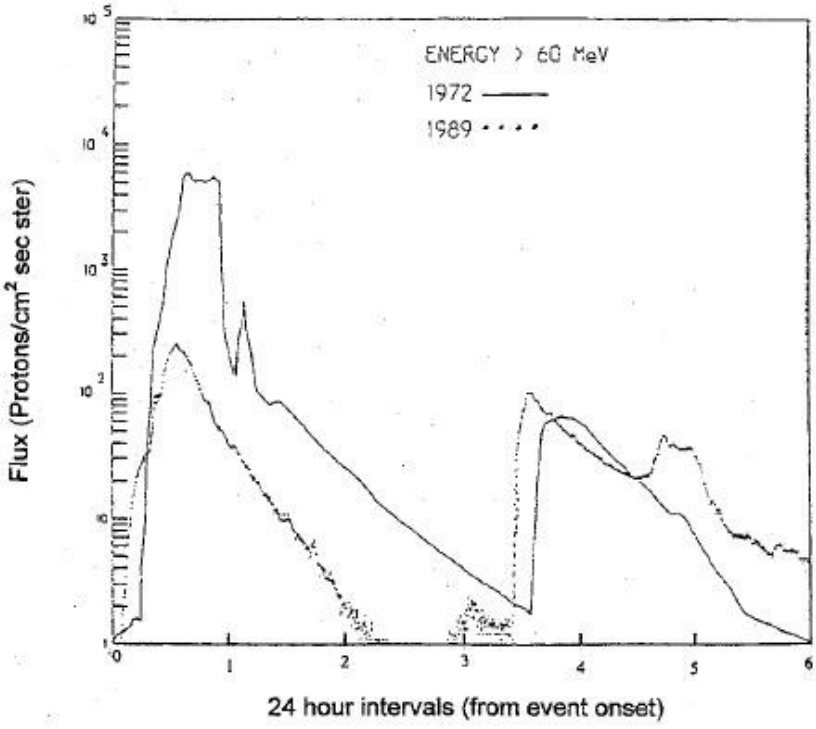

Figure 1.6 - Proton fluxes for two SPEs with E > 60 MeV [Feynman, 1996]

The gradual events have the largest particle fluences, and are composed especially by protons. The largest SPEs occur with gradual SPEs indeed. In general these events have fluxes that decay slowly, in order of days. Sometimes, for the bigger SPEs another increase is found, as showed in figure 1.6. Figure 1.7 shows the differential proton flux spectra measured by the NOAA Geostationary Observatory Environment Satellite (GOES) 7 [NGDC, 2001] during the October 1989 series of events (one of the largest SPE ever measured).

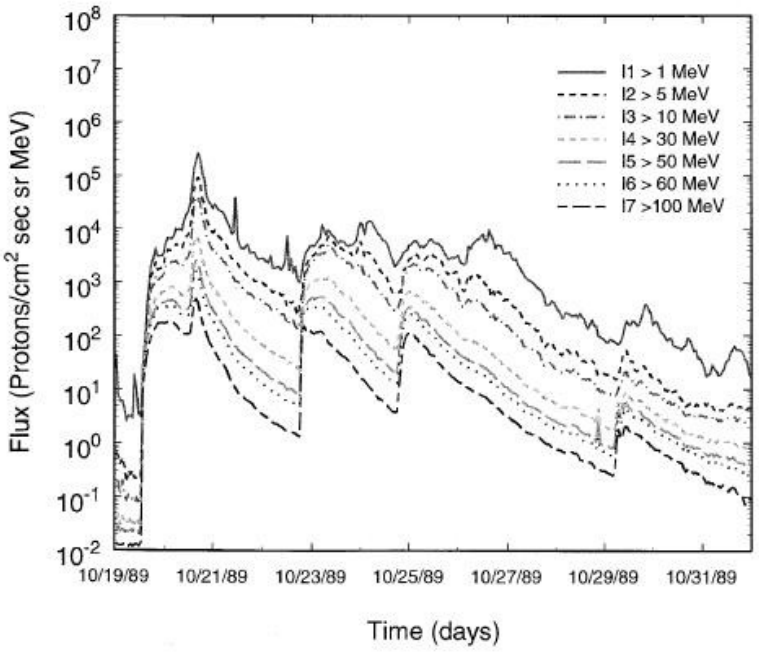

Figure 1.7 - Differential proton flux of a very energetic SPE [Benton, 2001]

The impulsive events have lower fluences, span in shorter period (few hours or even less) and are characterized by large fluxes of electrons. Compared with gradual events they present enhancements of heavy ions and smaller proton fluxes.

1.1.3 - Earth's magnetic field

Earth's magnetic field allows a protection against the radiation and permit to reduce the flux that arrives to the Earth's surface and in LEO as well. It is approximately a magnetic dipole and it extends infinitely from the Earth, weakening with distance from its source. The magnetic field work as a shield against solar wind as well, but the arriving particles compress the field lines on the side Sun-facing. In the night side instead the line of the field are opened and extends infinitely – the *magnetic tail*. In the figure 1.8 the magnetic field lines and the solar wind particle trajectories interacting with the magnetic field are depicted.

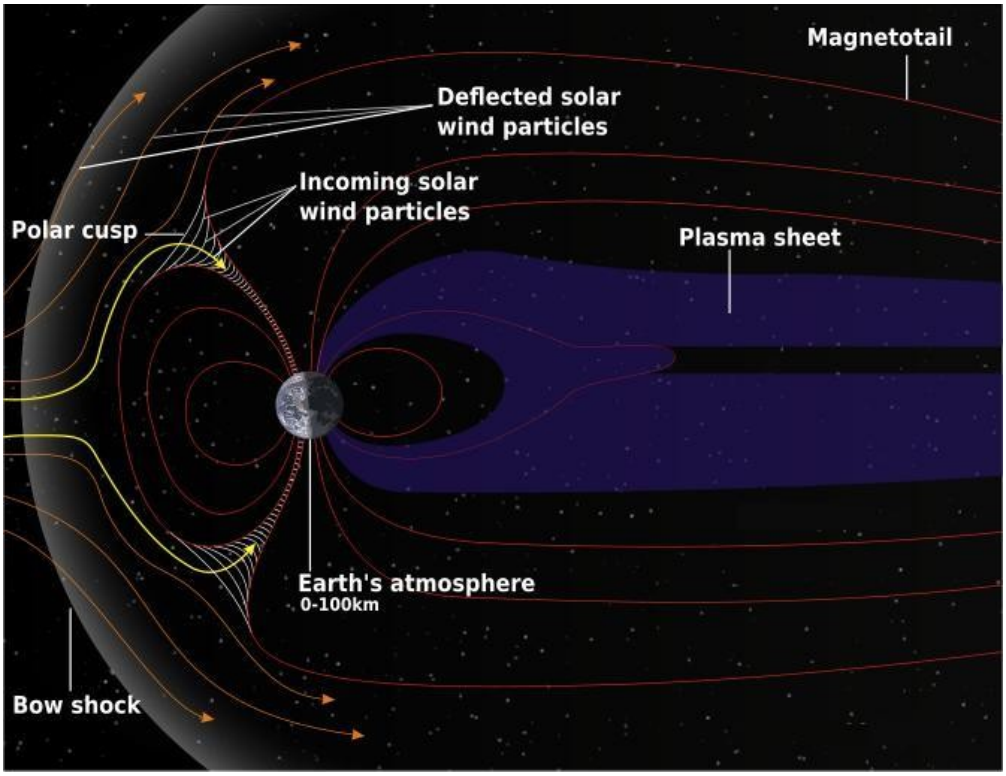

Figure 1.8 - Earth's magnetic field interacting with the solar wind – NASA www.nasa.gov

The solar wind is so deflected along the field lines and, depending on the particles energies, it can be led away following the lines of the magnetic tail or, for the

most energetic particles, it can be funnelled along the closed lines that are reconnected to the Earth's surface, penetrating in the atmosphere. Reaching the ionosphere these charged particles cause the phenomenon called *aurora borealis*. The solar wind interaction with Earth's magnetic field is responsible also for the creation of the *magnetosphere*. In the magnetosphere, a mix of free ions and electrons from both the solar wind and the Earth's ionosphere is confined by electromagnetic forces that are much stronger than gravity, which would drop the particles on the Earth. On the side facing the Sun its boundary is about $70 \cdot 10^3$ km. This value is time-changing because the 11-year solar cycle prompts a variation in the solar wind flux, producing an increasing or decreasing of its pressure on the magnetosphere. Therefore solar wind is responsible for the shape and extension of the Earth's magnetosphere, and its speed, density and direction affect the local space environment of the Earth. When the magnetic field decreases, due for example to a SPE event like a solar flare, it leaves the passage through the field lines of the lesser energetic particles that before were being deviated along the field lines, permitting them to reach lower altitudes with respect to the Earth's surface. When a solar flare occurs the magnetic field decreases abruptly, causing a *geomagnetic storm*. It can be very intense and creates serious problems to the radio communication among spacecraft and satellites orbiting around the Earth, and the strong weakening of the magnetic field could cause even a higher level of radiation contamination aboard spacecraft in LEO.

1.1.4 - Van Allen radiation belt

Protons and ions emitted by the solar wind and from GCRs can be trapped by the Earth's magnetic field in a torus of energetic charged particles around Earth which lies at the latitude of the equator. Charged particles are being trapped because the magnetic field acts just as a magnetic mirror. Particles gyrate around field lines and also move along field lines. When a charged particle encounters the lines of the magnetic field it is funnelled along the line towards the poles where the magnetic lines converge and the strength of the magnetic field increases. Therefore the velocity of the particle along the field line is slowed and a certain point reversed. This causes a continue bounce back and forth of the particle

between the Earth's poles. The radiation belt is split into two distinct belts, with energetic electrons forming the outer belt and a combination of protons and electrons creating the inner belt (but there are also traces of other nuclei, especially alpha particles). Figure 1.9 shows the structure of both inner and outer radiation belt, with the cyclotron trajectory along the field lines and the bounce motion.

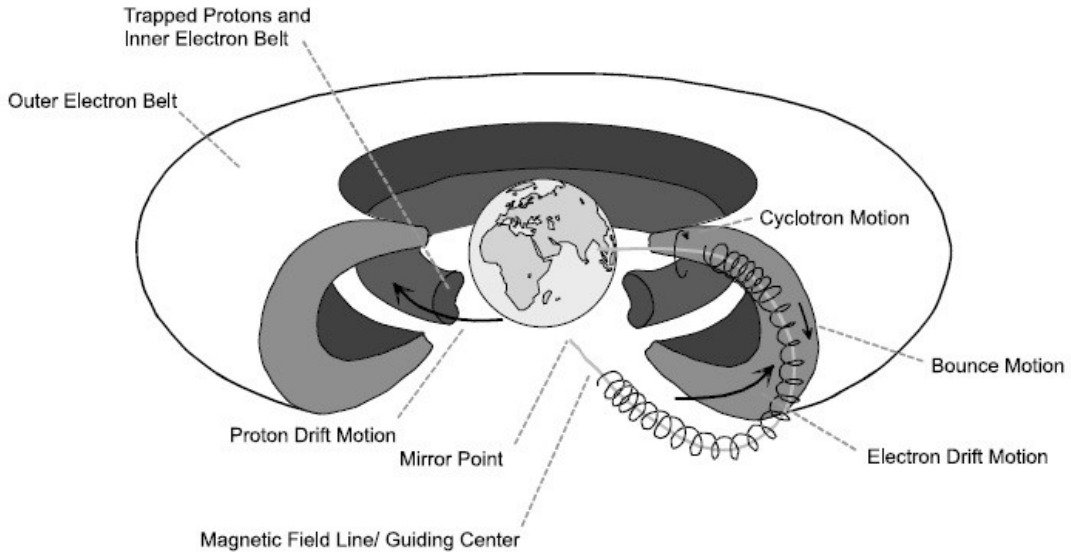

Figure 1.9 - Structure of the inner and outer radiation belt [Benton, 2001]

The large outer radiation belt extends from an altitude of about three to ten Earth Radii (*ER*) above the Earth's surface. Its greatest intensity is usually around 3 *ER*. The outer belt consists mainly of high energy (0.1–10 MeV) electrons and the rest of the population is formed mainly by protons, alpha particles and O^+ oxygen ions. The inner Van Allen Belt extends from an altitude of 100–10,000 km (0.01 to 1.5 ER) above the Earth's surface. It consists of energetic protons with energies exceeding 100 MeV and electrons in the range of hundreds of keV. Figures 1.10a and 1.10b show respectively the outer and inner radiation belt, with the contours of the omnidirectional flux of the protons respectively > 1.0 MeV and > 400 MeV.

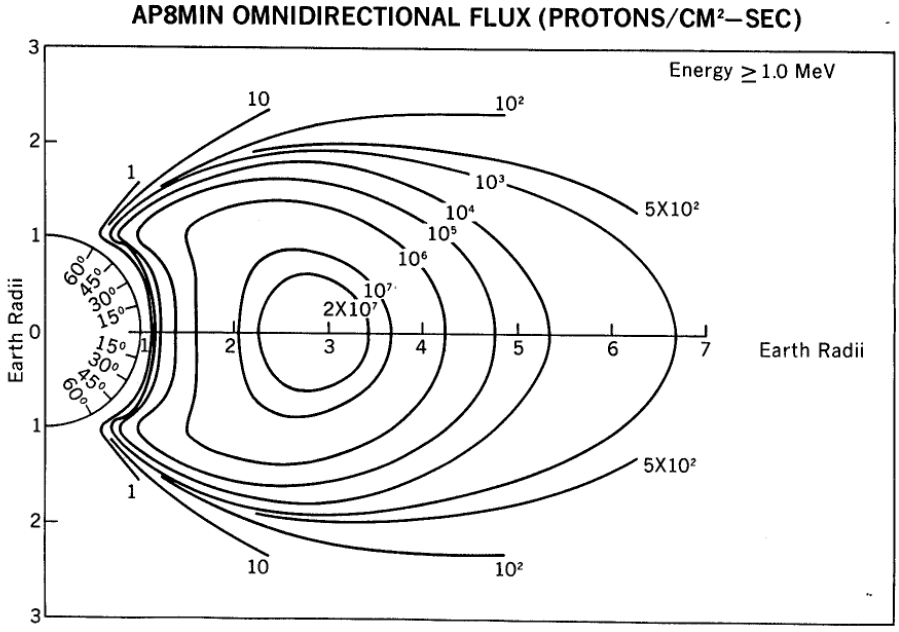

Figure 1.10a - Contours of the omnidirectional flux of protons with energies > 1.0 MeV in the outer belt – US National Space Data Center - AP8MIN model

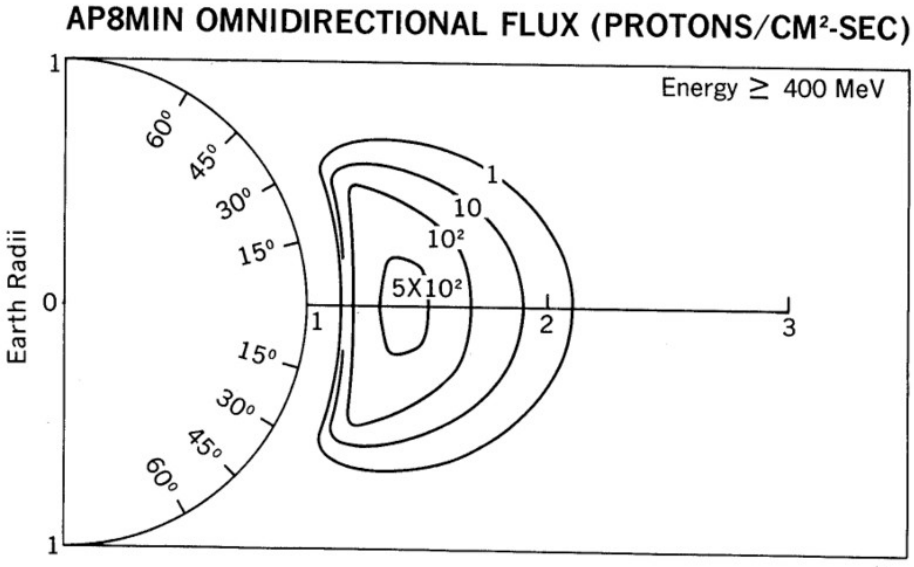

Figure 1.10b - Contours of the omnidirectional flux of protons with energies > 400 MeV in the inner belt– US National Space Data Center - AP8MIN model

The inner belt causes the most of hazardousness to the astronauts in LEO, especially during EVA (Extra-Vehicular Activities).

The most important source of hazard caused by the Van Allen radiation belt is the area where the inner radiation belt comes closest to the Earth's surface, called *South Atlantic Anomaly* (SAA). The presence of the SAA is due to the fact that the Earth's magnetic axis is tilted-up respect to the Earth's rotational axis by an angle of ~11 degrees. The intersection between the two axis is located at about 500 km above the center of the Earth. Because of this tilt and translation of the magnetic axis, the inner Van Allen belt is closer to the Earth's surface over the south Atlantic ocean, and farther from the Earth's surface over the north Pacific ocean. In figure 1.11 the detailed location of the SAA in the south Atlantic is represented.

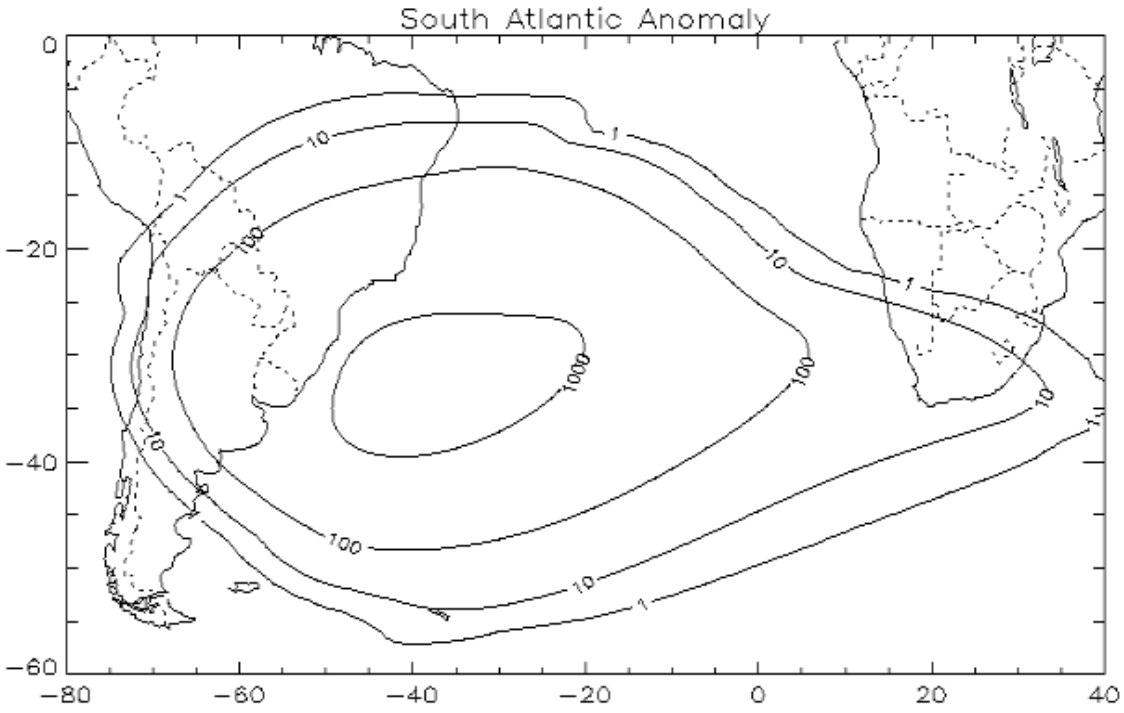

Figure 1.11 - Location of the SAA at 500 km altitude with proton fluxed > 50 MeV [AP8MIN model]

The SAA has a great relevance for the spacecraft in LEO because their orbits pass the anomaly periodically, exposing the astronauts to several minutes of strong radiation caused by trapped protons.

1.2 - Cosmic rays flux modulation

The flux, energy and component distributions of the space radiation field in the spacecraft's orbits in the proximity of the Earth depend on parameters such as the altitude and inclination of the orbit, the orientation of the spacecraft relative to the Earth and Sun, and also a time dependence according to the 11-year solar cycle. We shall discuss the former in the next paragraph and describe in the following the important time-dependence flux modulation of the solar cycle.

The variation of the solar activity along with the ~11-year solar cycle changes the level of solar radiation that arrives on Earth and therefore the radiation received by astronauts, especially in interplanetary missions.

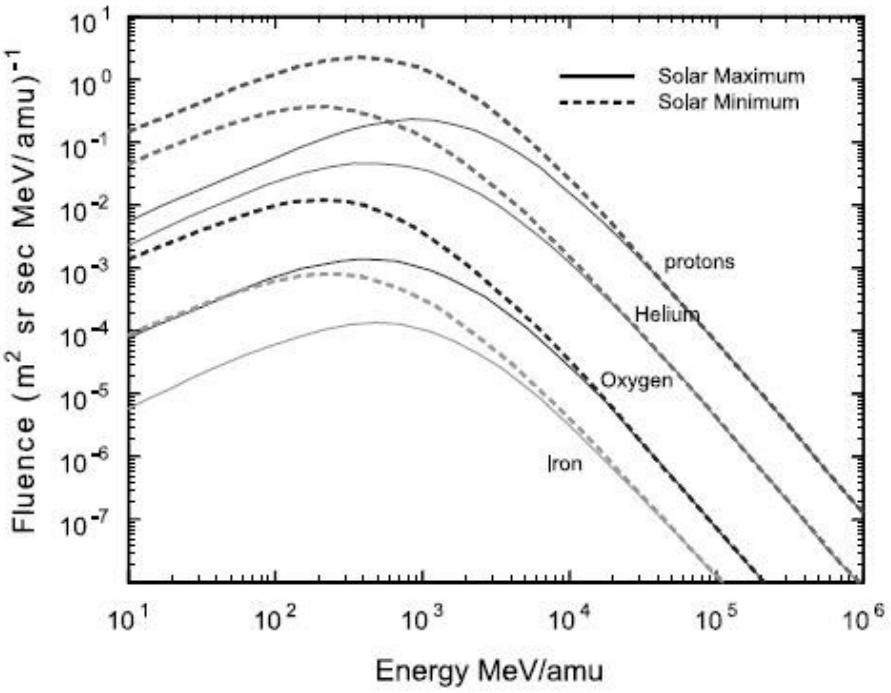

Figure 1.12 - GCRs modulation according to solar cycle. The increasing in fluence is associated with the solar minimum, where the solar wind is weak [Benton, 2001]

There is a maximum variation in the radiation hazard between solar maximum and solar minimum by a factor of three [Badhwar, 1994]. The modulation of GCRs by solar wind is well evident in the figure 1.12. During solar maximum the attenuation is greatest, because the solar wind is most intense and the flux of its particles, together with the magnetic field correlated with it (the *interplanetary magnetic field*), acts as a shield. GCRs flux is highest during solar minimum instead, in which the activity of the solar wind is reduced.

Thus scheduling for missions has to be strictly correlated to the sun activity, especially when spacecraft are involved in interplanetary missions, as weak solar activity during a solar minimum is responsible for major GCRs fluxes, whereas strong solar activity is strictly correlated to SPEs of high energy that have high fluences and could cause very high level of absorbed dose in few hours. The solar wind modules also the strength of the Earth's magnetic field, since the charged particles of the solar wind interact with the magnetic field causing a decreasing of its strength, and therefore during solar maximum the net flux of cosmic rays that penetrate through the atmosphere is higher. Therefore the type of mission planned, if remaining in LEO or rather being placed outside the protective shell of the magnetic field, should take into account the phase of the solar cycle which could act both as a protection against GCRs and as source of strong and hazardous radiation for astronauts.

1.3 - External radiation field in L.E.O.

Particles from SPEs, GCRs and Van Allen inner belt form the radiation environment in which astronauts in LEO have to live each day. These sources make nearly the total of the contribution to the primary radiation flux encountered in LEO missions. The ISS orbit lies in LEO at an average altitude between 390-400 km and with an inclination of 51.6°. It travels at an average speed of 27,743 km/h, completing 15.7 orbits per day (an orbital revolution in LEO takes about 90 minutes). ISS has been built through a partnership between ESA, NASA, JAXA (Japan), CSA (Canada) and Rocosmos (Russia). The station construction started with the launch of the Zarya control module and subsequently the station was expanded with research modules (Zvezda, Destiny,

Columbus, Poisk, Rassvet), connection nodes and solar arrays. The first permanent crew started at the 2nd of November 2000 and for nine years was manned with crew of three astronauts staying up there for 6 months. Currently the station has a permanent crew of six astronauts.

The radiation field encountered outside by the ISS or other spacecraft is called *primary radiation*, whereas the *secondary radiation* is produced in the interaction between primary radiation and the spacecraft structure. Secondary radiation will be discussed in the next paragraph.

SPEs are largely shielded by the Earth's magnetic field, and therefore only the more energetic events have relevance in LEO orbits. This vertical magnetic cut-off blocks all the SPEs with energy below 500 MeV/nucleon, and only very few solar protons arrive as far as the ISS orbit. Similarly the less energetic GCRs particles are deviated along the field lines, but the more energetic particles pass through the magnetic field lines as far as the outer layer of the atmosphere and also deeper, depending on their energy. Inside the solar system the GCRs spectra is peaked around 800-900 MeV. In ISS mean orbit altitude the magnetic field provides a reduction on average by a factor of 10 in the total GCRs exposure relative to the interplanetary environment. Trapped protons in the inner radiation belt extend in energy from few MeV to several hundred MeV and form a broad peak between 150 and 250 MeV.

This broad spectra of radiation is continuously both time and spatial changing, and total radiation flux that arrives in a LEO orbit is strictly dependent on the phase of the orbit, the orbital parameters (inclination, altitude and velocity vector) and the time-phase respect the solar cycle. Therefore there are strong variations in the LEO external radiation flux, so that planning and scheduling of spacecraft missions are strictly correlated with this time and space-dependent parameter.

1.3.1 - Dependence on orbital parameter

Radiation field in LEO has a strong dependence on spacecraft orbital parameters, that is orbital inclination (measured with respect to the equator), altitude (with respect to the Earth's surface) and even the direction of velocity vector of the

spacecraft add an important component to the radiation field measured aboard, the so called east-west trapped proton anisotropy.

The single contribution from GCRs and from trapped protons of the radiation belt is very dependent on the inclination of the spacecraft orbit. In high inclined orbits (orbits that pass near the magnetic poles) the GCRs component is dominant, because GCRs are channelled along magnetic field lines towards the poles and for such high inclined orbits the time that spacecraft spend in the SAA is very low, and so it has low total effect. Instead for orbits of low inclination, which remain close to the equator, the time that spacecraft spend crossing SAA is longer, and therefore trapped protons become the major radiation hazard. The contribution from SAA is also extremely dependent on the spacecraft altitude: the flux increases exponentially with altitude from the Earth surface (but there is a peak around 0.5 ER). Also flux of GCRs increases with altitude, due to the decreasing atmospheric density, but this phenomena is far less strong at LEO altitude. Combining altitude and inclination parameters, it has been on high altitude and low inclination orbits, such as the Space Shuttle missions, that one has measured the highest mean dose rates absorbed by astronauts.

Finally, the east-west trapped proton anisotropy is of important relevance for spacecraft that traverses SAA, especially for that ones such as ISS that have fixed orientation relative to the magnetic field. Protons travelling along field lines in cyclotron motion encounter denser layer of atmosphere while travel in west direction, since this portion of the particle cyclotron orbit lies at lower altitude, below the spacecraft, and therefore undergo more interactions and are attenuated. Consequently the west-side of the spacecraft receives less flux of radiation compared to the east-side. Trapped proton anisotropy can lead to differences up to a factor of 3 in dose rate between east and west part of spacecraft, and therefore it is an important variable to consider in setting the living environment of astronauts inside the spacecraft.

1.4 - Interaction with structure in spacecraft

When radiation passes through the mass of a spacecraft the primary particles not only lose energy in the form of ionization but, depending on its energy and charge, can undergo nuclear interactions with the nuclei that compose the structure, producing secondary particles. Thus the radiation environment that astronauts encounter in the interior of a spacecraft is largely modified by all these interactions, and aboard they experiment different kind of radiation hazard. There are mainly two types of nuclear interaction between primary particles and the nuclei composing the mass of the spacecraft: *target fragmentation* and *projectile fragmentation*. Target fragmentation takes place when the primary flux of high-energy and high-charged ions collides with heavy nucleus and, depending on the kinetic energy of the primary particles, the nuclear interaction can open different channels of secondary particles production (such as neutrons, alpha particles, protons and heavy recoil nuclei). These kinds of processes occur mostly when trapped protons of the radiation belt and GCRs protons collide with the aluminum nuclei of the spacecraft shielding. Projectile fragmentation occurs when high-energy heavy ion, typically called HZE particles, collide with the nucleus of the target. Again a large number of reaction channels are being opened, producing high-energy neutrons, protons and larger fragments that retain most of the kinetic energy of the primary HZE particles.

Subsequently after these two types of nuclear reactions, the secondary particles can undergo further reactions, interacting with the spacecraft internal structure. A lot of other particles are produced, so that the radiation field inside spacecraft is very complex. Besides neutrons, protons and heavy nuclei the contents of the secondary particles include pions, mesons, electrons and γ-rays.

The interaction of the primary radiation with the structure and the following production of secondary particles has been modelled by different radiation transport codes. In literature one can find different codes, both using analytic approaches [Wilson, 1995] and using Monte-Carlo code. Monte-Carlo simulations of secondary neutron flux inside ISS were made using SHIELD code to understand how thickness and material of the spacecraft shielding affect the generation of secondary radiation aboard [Getslev, 2004].

Thin and moderate shielding is effective in the reduction of absorbed dose by the less energetic GCRs inside the spacecraft, but permits the more energetic particles to penetrate. As shield thickness increases, although now primary energetic particles are being stopped, the shield effectiveness drops. This happens because GCRs interacting with larger portion of structure increase the number of secondary products, especially neutrons. Secondary neutrons are the major component of the secondary radiation. Neutron spectra inside spacecraft spans on a wide energy range that can be divided in moderates neutron with energy <1 MeV, evaporation neutrons of energy between 1 and 20 MeV, intranuclear cascade neutrons with energy between 20 and 200 MeV and neutrons with energy from 500 to about 5 GeV that are produced from the fragmentation of high energy GCRs.

The predicted integral particle spectra inside ISS has been obtained by Armstrong and Colborn [Armstrong, 2001] through Monte Carlo simulations (figure 1.13).

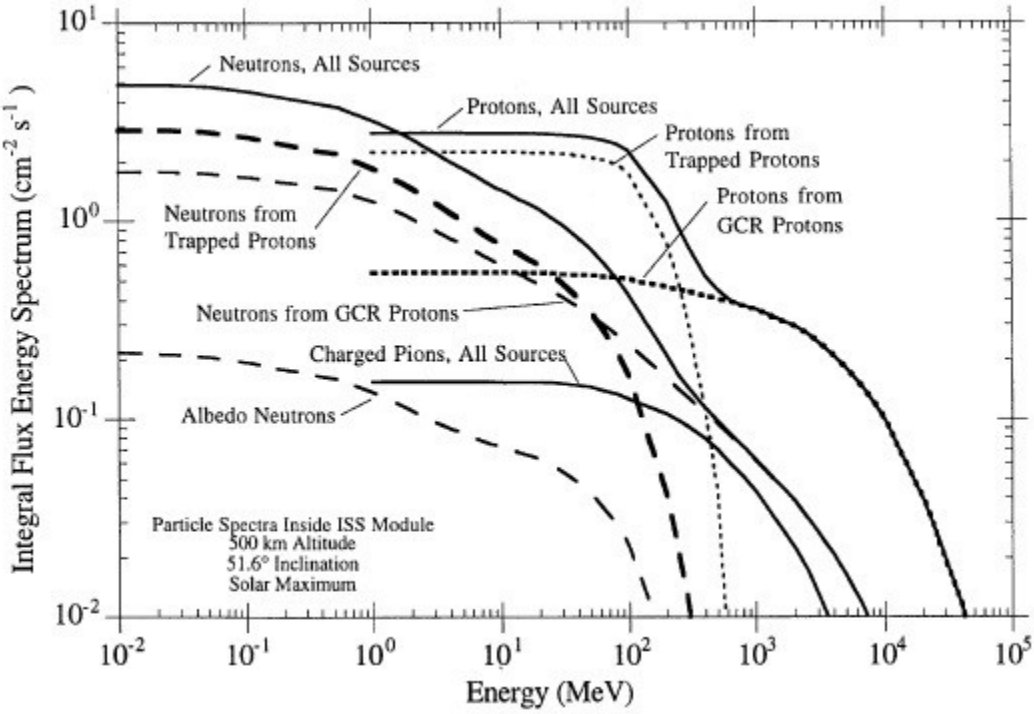

Figure 1.13 – Results of the simulations inside ISS (500 km altitude at 51.6° inclination) during solar maximum. The simulation is based on the contribution of GCR, trapped protons and Earth albedo neutrons [Armstrong, 2001]

It shows the result of the simulations inside ISS (500 km altitude at 51.6° inclination) during solar maximum due to the contribution of the external radiation field composed of GCRs, trapped protons and Earth albedo neutrons. It's evident as inside ISS the bulk of the secondary radiation consists of protons and neutrons ranging in energy from few keV to several hundreds MeV.

Modification of the primary radiation field is highly dependent on the specific composition of the shielding material. Different kind of materials rather than aluminium (such as polyethylene, or materials that have high hydrogen content) might provide a better protection because a lower level of secondary particles would be produced inside the spacecraft. The choice of an optimal configuration for the spacecraft shielding thickness and material is therefore essential in order to decrease at the same time the flux of primary radiation inside spacecraft and the production of secondary neutrons and charged particles.

CHAPTER II

Dosimetry in the space

2.1 - Introduction

This chapter is devoted to describe the current status of dosimetry in the space and what is its role in the task of understanding the biological effects and risks for the astronauts in their stay aboard spacecraft and space station caused by the space radiation field. First it is explained what is and how is defined the biological effect of radiation and which quantities are used in space dosimetry. Then the current instruments used aboard the International Space Station and which types of measurements they perform are presented. An overview of the data and results in the literature is presented, emphasizing the contribution of the different radiation components. Finally the results drawn from the data and the guidelines of radiation protection currently in use are outlined.

2.2 - The biological effect of radiation

Radiations from GCRs, SEPs and from Van Allen radiation belts form a complex mixture of radiation of protons, heavy ions with high charge, neutrons, x-rays and γ-rays. The purpose of space radiation dosimetry is to asses what is the biological effect on the human body caused by this radiation field. Radiation traversing a material causes excitations and ionizations, which are the two main ways in which radiation deposits energy in the material itself. If this material is living tissue, the ionizations can provoke biological effects, since the DNA and the molecular content of the cells can undergo damages and critical disruptions. For instance the biological effects that radiation can cause are cancer, cataracts, neurological disorders, genetic mutations and increasing non-cancer mortality risks.

The amount of dose absorbed by matter or living tissue from ionizing radiation is defined as the quantity of energy deposited per unit of mass. The Gray is the SI

unit of absorbed dose, corresponding to the deposit of 1 J of energy in 1 kg of matter. The dose alone nevertheless it is not sufficient to quantify the biological effect of radiation. It has indeed been observed through radiobiological experiment that at the same dose deposited the biological effects of different radiations are not the same: this happens because the biological effect is highly dependent by the distribution of the energy released on the tissue rather than by its mean value. The damage and the effect on the living tissue is dependent by the type of radiation, by the range of energy considered and by the type of living tissue irradiated as well. Therefore a new quantity, the *equivalent dose,* has been defined, the *Sievert* (Sv), which takes into account the biological effects of the radiation. In this way at the same dose absorbed, different kinds of radiations can have different equivalent dose. Equivalent dose H_T is obtained by multiplying the absorbed dose D in a tissue with a radiation *weighting factor* W_R different for each type of radiation R:

$$H = W_R \cdot D \qquad 2.1$$

The weighting factors W_R have been experimentally evaluated only for few particles (neutrons, γ-ray, electrons, alpha particles and protons) and for limited range of energies in radiobiological experiments. Table 2.1 summarize the recommended value for W_R by the International Commission on Radiological Protection (ICRP) [ICRP, 1978], [ICRP, 1991]. For the neutrons ICRP has defined a continuous curve as showed in figure 2.1.

Type of radiation	W_R
Photons	1
Electrons	1
Protons	2
Alpha particles	20

Table 2.1 – Radiation weighting factors for different type of radiations given in ICRP 1991

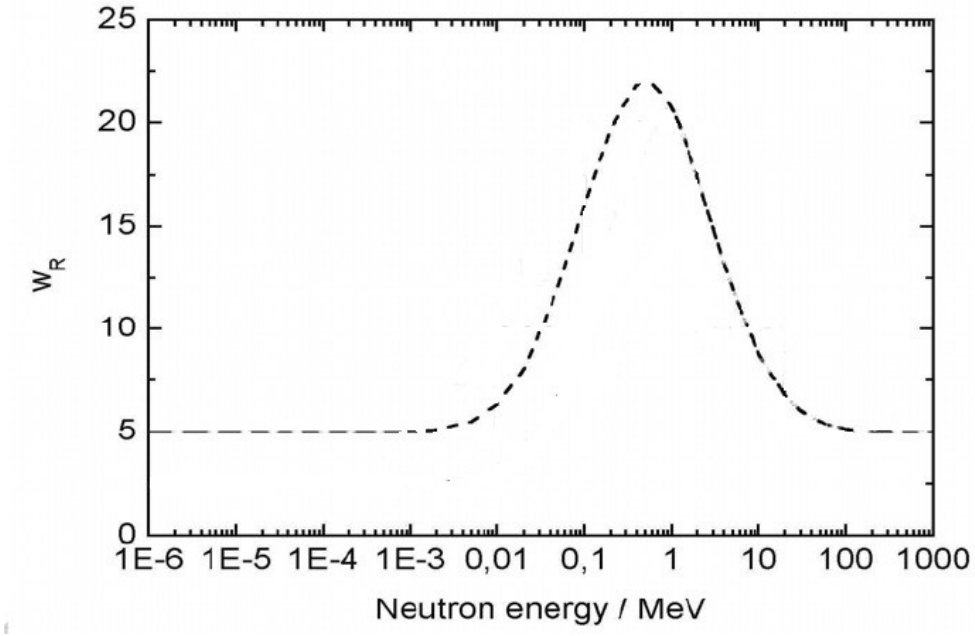

Figure 2.1 – Radiation weighting factor for neutrons given in ICRP 1991.

The system of radiation protection is based on the guidelines provided by ICRP in its Report 60 [ICRP, 1991]. ICRP defines also the concept of the mean absorbed dose in tissue or organ *T* and for a given type of radiation *R*, $D_{T,R}$, and the *tissue weighting factor* W_T, specific for each type of tissue or organ. Multiplying $D_{T,R}$ by the weighting factor W_R and by W_T and summing all the contributions for the whole body, the *effective dose* *E* is obtained:

$$E = \sum_{T,R} W_T \cdot W_R \cdot D_{T,R} \qquad 2.2$$

The effective dose is used in the space dosimetry as the baseline for the radiation risk estimation and for radiation protection limits. In mixed radiation field such as in the space, in which all the types of radiation with very wide ranges of energies are present, one should multiply each component for the specific W_R in order to obtain the equivalent dose of the radiation field. To do this one should need a complete knowledge of the composition, energy spectra and spatial distribution of the radiation field in the space. Besides, knowledge of the

specific biological quality for the different radiation components is not available. This has brought out the necessity to adopt new concepts of radiation protection. To tackle this drawback ICRU has set a new quantity called *dose equivalent*, still denoted by *H*, which is calculated by multiplying the absorbed dose contribution at a given LET[2] (Linear Energy Transfer) for a LET dependent quality factor *Q* and summing over the LET spectra, as shown in equation 2.3 [ICRU, 1983]:

$$H = \sum_{L} Q(L) \cdot D(L) \qquad 2.3$$

The dependence of *Q* in relation to the LET is given in ICRP-60 [ICRP, 1991]. Briefly it states that *Q*=1 up to a LET value of 10 keV/μm, then Q increases up to 29.8 at 100 keV/μm and finally slowly decreases with increasing LET. Dosimetry instruments give a direct measure of the absorbed dose, measured in Gray. Some instruments can measure also the LET, and then it is possible, by equation 2.3, to obtain the dose equivalent. This kind of measurements is of first importance for understanding the biological effectiveness of the complex radiation field that is present aboard spacecraft.

2.3 - Dosimetry aboard spacecraft

Astronauts aboard spacecraft in LEO such as Space Shuttle and ISS or aboard spacecraft in missions towards Moon or Mars are exposed to level of ionizing radiation much higher than those that typically humans absorb during a year on the ground. To asses the radiation effectiveness and risk inside the spacecraft is therefore of primary importance. Given that the space radiation field that hits the spacecraft is both space and time dependent, the detection and characterization of this field is a difficult task. Moreover the space radiation environment consists of a large range of charged particles and radiation with very different fluxes and energies. The external radiation field interacting with the spacecraft shielding produce secondary radiation that consists of many different types of particles

2 The definition of the LET is given in Appendix I

with a broad range of energies. Particles fluxes also are very variable, often are quite low, sometimes also less than one particles per minute, but in some cases, like during SPE, fluxes can increase dramatically by several orders of magnitude. Spacecraft dosimetry thus is implemented by a suite of different detectors, each one optimized to measure a particular radiation component or a particular range of energies. We can distinguish anyway between two kinds of instruments: *passive detectors* and *active detectors*.

Passive radiation detectors have been used since the early days of the space program to quantify the space radiation environment. Active radiation detectors which record and display measurements continuously whereas passive radiation detectors accumulate signals over the entire course of their exposure. Therefore the main drawback of passive detectors is that they cannot provide real-time data, and thus they are incapable to survey sudden variations in the dose absorbed, for instance during a strong and energetic SEP which could be very dangerous for the crew safety.

Active dosimetry implements a new generation of radiation instruments, to improve the crew radiation exposure risk estimation. They permit to have a real-time detection of the radiation field, displaying the data immediately to the crew and continuously monitor and telemeter radiation data to the Earth. Active dosimeters permit both time and spatial resolution: in this way they can gather radiation data throughout the mission in order to obtain the variation of the particle spectra with orbital parameters as well as with temporal fluctuations. Thanks to this features, active dosimetry permitted to discriminate the contribution of the different components to the radiation hazard. It has been of fundamental importance to separate the contribution from trapped protons of the radiation belt and GCRs component to the total dose and likewise the contribution of the SAA with respect to that of GCRs and even to understand the steep variation of dose during solar proton events and the latitude dependence of the total dose due to the Earth's magnetic field.

2.3.1 - Current radiation dosimeters aboard ISS

The constraints imposed by the space environment and the cost of bringing the instruments aboard spacecraft have deployed a large array of complications and

difficulties in the development of instruments adapt for this kind of task. Instruments and electronics have to be small and of low mass, due to the high cost of launching equipment into orbit and also they must have a robust design and be reliable and able to withstand a large amount of use without malfunction, because availability of spare parts aboard is minimal. Passive dosimeter are of small size, safe and easy to use and have zero power consumption and therefore they have been used for much of the history of human space flight and are still now used.

Passive detectors used for crew and area dosimetry can be divided in two types: *thermoluminescent detectors* (TLDs) and *solid-state nuclear track detectors* (SSNTDs). TLDs are inorganic crystalline materials that record the total absorbed dose from ionizing radiation (figure 2.2). As charged particles pass through the TLD they lose energy by ionizing (displacing electrons to a higher energy state) atoms of the crystal. The electrons displaced are being trapped and accumulated. The absorbed dose is determined using a TLD reader. The TLD reader heats the TLD, pushing the electrons out of their trap, to a lower state of energy. This process releases energy and gives off visible light, measured by the TLD reader, which is proportional to the total absorbed radiation dose accumulated during the exposition.

Figure 2.2 - TLD used aboard ISS - NASA www.nasa.gov

The solid-state detectors have been built using different kinds of material. Plastic nuclear track detectors (PNTD) were widely used, and currently aboard ISS a CR-39 PNTD is employed. CR-39 PNTD is made of polymers that are sensitive to charged particles of LET greater than or equal to 5 keV/μm. It is usually made up of thin (approximately 0.6 mm) sheets which are assembled in multi-layer stacks.

Charged particles that pass through the CR-39 PNTD with enough LET to break the molecular bonds of the polymer form a pathway. The size of a nuclear track, when normalized to the quantity of detector sensitive material removed for the process of analysis, is proportional to the LET of the charged particle that has produced the original trail.

Other types of passive dosimeters have been used some of them not more in use. The most common are photographic nuclear emulsions, bubble detectors, activation foils and fission foils.

Currently aboard ISS there are two main instruments for the active monitoring of the radiation environment: the *Tissue Equivalent Proportional Counter* (TEPC) and the *Charged Particle Directional Spectrometer* (CPDS).

The TEPC is a gas proportional counter able to collect data as a function of time, giving a real-time measure of dose exposure. The gas counter cavity is able to simulate a tissue microscopic volume and to measure the spectra of energy imparted by ionizing charged and neutral particles. The TEPC currently used aboard ISS (figure 2.3) is a cylindrical detector made of A150 tissue-equivalent plastic (for the detector wall), of 5.08 cm diameter by 5.08 cm length. It is filled with propane gas at 2 kPa to simulate 2 μm diameter volume of human tissue.

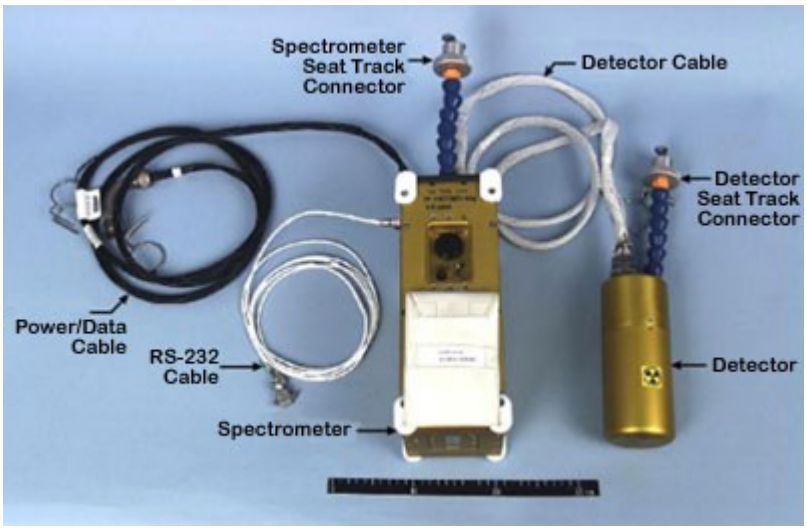

Figure 2.3 - ISS cylindrical Tissue-Equivalent Proportional Counter – NASA www.nasa.gov

This TEPC measures lineal energy in the range from 0.4 to 1000 keV/μm. There is an alarm threshold of 0.05 mGy/min, considered a risky dose originated for possible SPE. The cylindrical TEPC has to be replaced in different directions and positions aboard ISS since it has not a isotropic sensitivity.

The CPDS instrument is designed to measure the charge, energy, and direction of a particle that passes through the instrument. It consists of a series of silicon solid-state detectors of various thickness, forming a telescope, because only particles passing through the cone of acceptance formed by two of these detectors are recorded, and therefore this coincidence triggered by the passage of the charged particle defines the geometrical field of view of the instrument. Then there are other four 5 mm thick Si detectors for the measurement of the energy deposition. Other detectors integrated inside the CPDS provide the coordinates and the charge of the particles gathered. In this configuration, including a Cerenkov detector, the differential energy spectrum of protons in the energy range from 15 to 450 MeV can be measured.

Currently, there are four CPDS instruments in use on-board the ISS. The first is the Intra-Vehicular Charged Particle Directional Spectrometer (IV-CPDS). The IV-CPDS is designed to be used inside the ISS, performing real-time calculations and it displays the average dose rate and other parameters registered aboard the station. The other three CPDS instruments are mounted outside the ISS, forming the Extra-Vehicular Charged Particle Directional Spectrometer (EV-CPDS). The EV-CPDS instruments are arranged such that one points forward along the velocity vector of the station (EV1), one points along the anti-velocity vector (EV3), and the third points up along the zenith direction (EV2). EV1 and EV3, pointing in opposite velocity directions, can determine the east-west asymmetry of trapped particles of the radiation belt. The EV2 provides instead information on SPEs and GCRs. In the figure 2.4a and 2.4b the IV-CPDS and the EV-CPDS are showed.

Figure 2.4a - ISS IV-CPDS - NASA www.nasa.gov

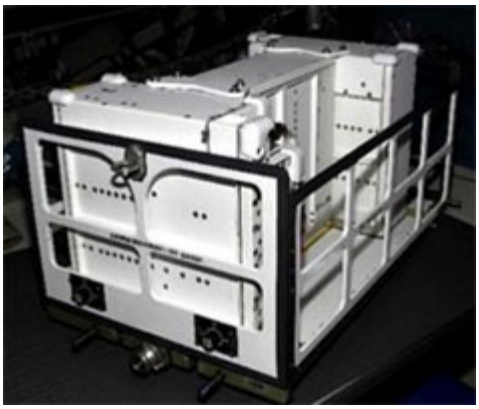

Figure 2.4b - ISS EV-CPDS - NASA www.nasa.gov

There are other complex detectors and experiments aboard ISS which perform further measurements. DOSTEL is a silicon telescope-based detector sensitive to particles of LET between 0.1 and 120 keV/μm. Inside the ISS is placed also an Organ Dose Measurement using the Phantom Torso which simulates a model human head and torso [Badhwar, 2002]. It integrates over 350 thermo-luminescent detectors and five silicon diode detectors to measure absorbed dose to specific organs. Moreover, a TEPC and a CPDS are placed near the torso during the measurements. This experiment aims to simulate doses at discrete locations within the body and it is able to distinguish the dose absorbed by different organs. The MATROSHKA experiment uses an analogue human upper torso phantom simulating the astronauts' space suit during EVA [Dettmann, 2007]. Therefore it is placed outside the ISS and its purpose is to collect data about the radiation exposure of astronauts in EVA, without the shielding protection of the spacecraft. Other detectors used in the past aboard MIR space station and that have been operative aboard ISS are the R-16 operational dosimeter, which consists of two cylindrical ionization chambers and the Liulin mobile dosimeter which is a portable silicon detector developed for use aboard spacecraft [Badhwar, 2002]

Table 2.2 summarizes the instruments before described, the type of measure that they perform and the type of radiation that they can detect.

Instrument	Type of measure	Type of radiation	Energy response
TEPC	LET spectra, absorbed dose, dose equivalent	All types of radiations – charged particles, neutrons and photons	0.4-1000 keV/μm
CPDS	LET spectra, nuclear abundances up to Oxygen, particle energy spectra	Any kind of charged particles, both primary or secondary	~5-400 MeV/nucleon
TLD	Absorbed dose	Any kind of charged particles, both primary or secondary	≤ 10 keV/μm
CR-39 PNTD	LET spectra, absorbed dose	Any kind of charged particles, both primary or secondary	≥ 5 keV/μm

Table 2.2 - List of the detectors used inside ISS, what they measure, the type of radiation that they can detect and the energy range of the measurement

2.3.2 - Dosimetry measurements Intra-Vehicular and Extra-Vehicular

Let's see now which are the dosimetric data gathered in spacecraft and space stations and give a general overview of the present knowledge of the radiation exposure of astronauts in LEO. Dose measurements can provide informations about crew exposure as functions of orbital parameters (altitude and inclination), solar cycle phase and also data regarding the effect of spacecraft shielding and spacecraft orientation in the space. Since most of time the crew is busy in Intra-Vehicular (IV) works, the dosimetry aboard spacecraft has the dominant role and therefore most of the data present in literature concern with the IV radiation environment. Anyway during Extra-Vehicular Activities, that is work done by astronauts outside spacecraft, the protection of the shielding is lost and the radiation environment has thus a higher degree of hazard. Especially during high energetic SPEs the dose absorbed by astronauts in EVA can jump in few hours at intolerable level.

In LEO missions the dominant part of the radiation hazard come from GCRs and trapped protons from South Atlantic Anomaly. As seen in the paragraph 1.1 the relative contributions to the radiation flux of GCRs and protons from SAA is very sensible to the orbit inclination. Figure 2.5a and 2.5b shows the integral LET flux spectra measured by TEPC and CR-39 PNTD on the STS-57 and STS-60 missions, respectively at inclination of 28.5° and 57° (NASA's Space Shuttle is officially called *Space Transportation System*).

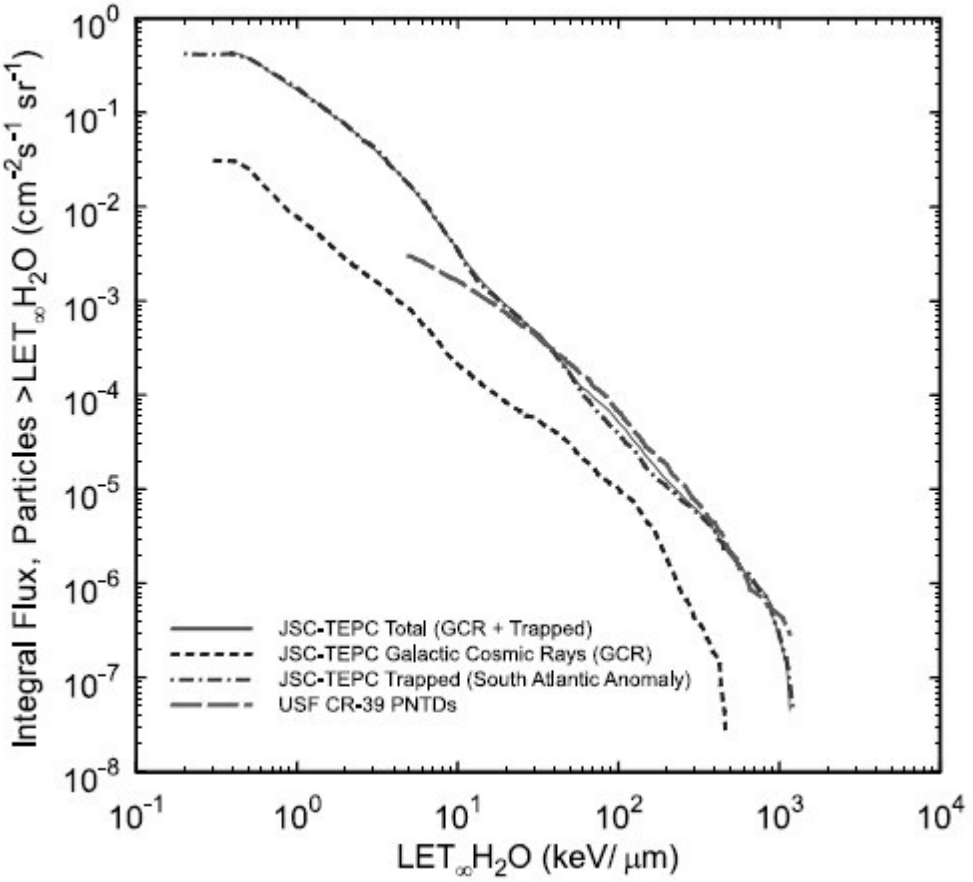

Figure 2.5a - Integral LET flux spectra measured on the STS-57 at inclination of 28.5° for GCRs and trapped particles [Benton, 2001]

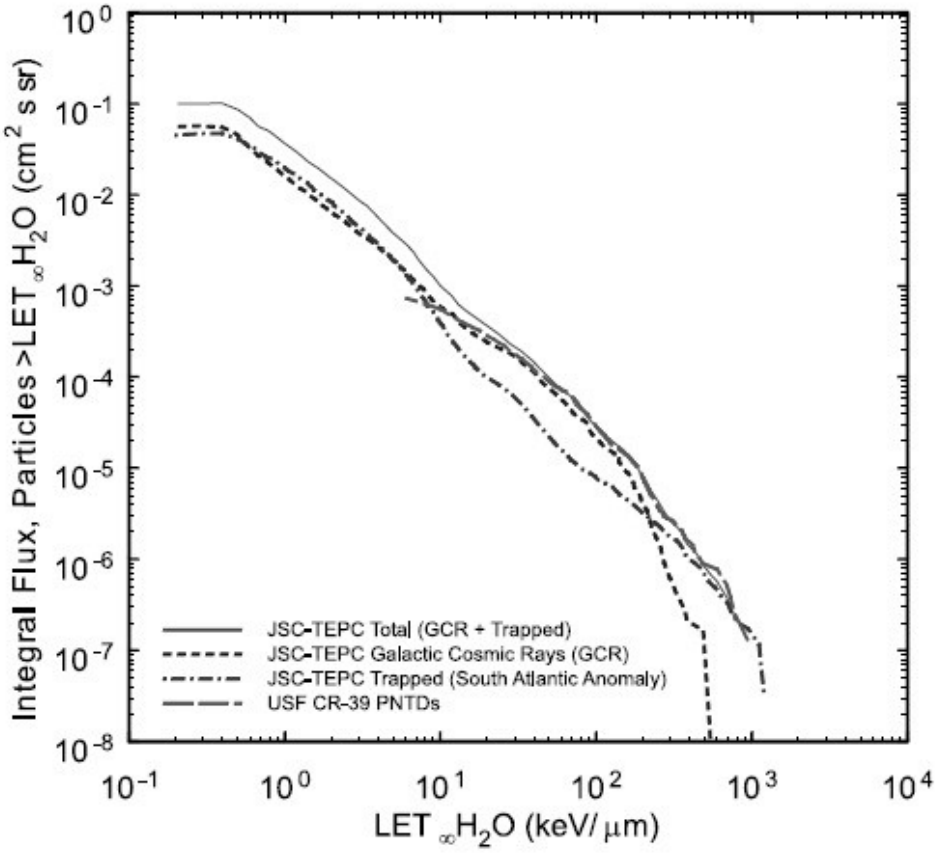

Figure 2.5b - Integral LET flux spectra measured on the STS-57 at inclination of 57° for GCRs and trapped particles [Benton, 2001]

Taking into consideration the TEPC result only, it is immediately clear that the contribution of GCRs at low inclination is negligible compared with the contribution from radiation originated from SAA. On the other hand, for high inclination, GCRs tend to become the bigger contribute.

TEPC is able to resolve the single contribution of GCRs from that of trapped protons from SAA, since it monitors in real-time the spectra of radiation. Therefore when the spacecraft enter in the SAA it is recorded an increment of the total absorbed dose in its spectra and thus it is possible to separate the two contributions. Figure 2.6 shows a spectra for the GCRs and trapped protons

radiation from a TEPC situated in front of the Phantom Torso experiment on STS-91 at inclination of 51.6° [Badhwar, 2002].

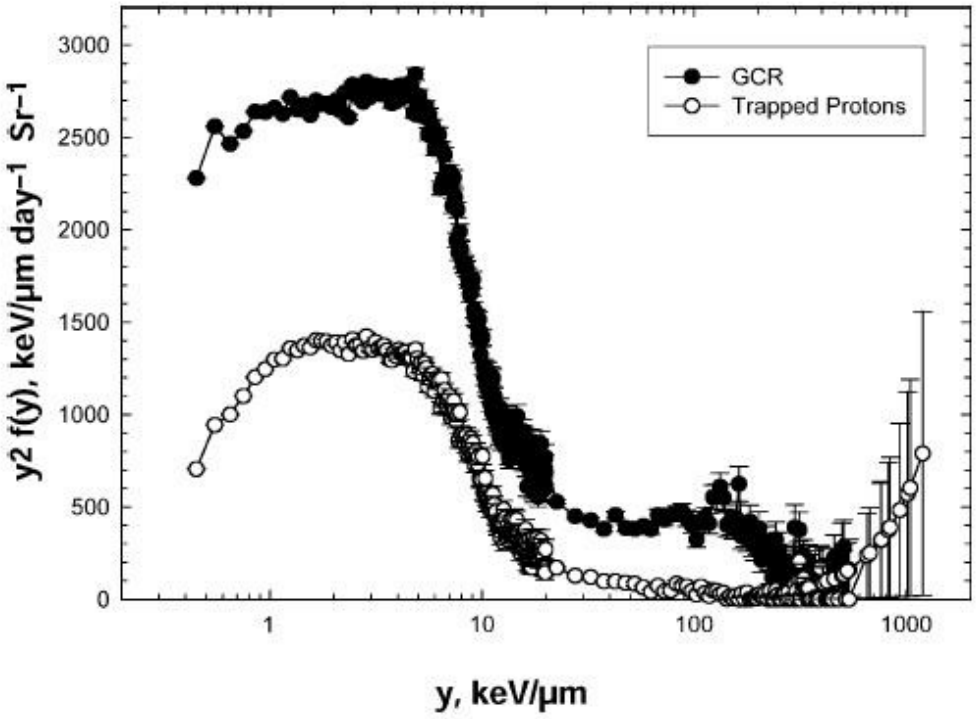

Figure 2.6 - TEPC spectra for GCRs and trapped protons. The instruments was situated in front of the Phantom Torso experiment on STS-91 at inclination of 51.6° [Badhwar, 2002]

Increasing the altitude, dose rate from the proton belts increases nearly exponentially whereas the contribution from the GCRs stays almost constant. Therefore also in an orbit with high inclination, at a given altitude the dose rate of trapped protons can become higher than that of GCRs. At solar minimum for an orbit at 51.6° inclination and 400 km in altitude, the two dose rates are almost equal [Badhwar, 1997].

Data about SEP events are not so abundant as that regarding GCRs or Van Allen radiation belt, since SEPs are shielded by magnetic field and spacecraft orbiting in LEO receive only a fraction of the radiation flux from SEPs. But in interplanetary space the hazard from SEPs could be the most important contribution, especially

in small span of time. Actually for spacecraft outside the Earth's magnetic field the onset of an energetic SEP can increment the dose exposure aboard exponentially in few days or even hours. With the current thickness of available shielding and considering the typical SEP energy spectra, the most important energy range to be considered in the study of SEPs is from 30 to 100-200 MeV for protons (which are the most abundant component). Figure 2.7 shows the simulations of dose equivalent delivered by the strong SEP of the August 1972 (one of the strongest) as a function of the shielding thickness (lines are associated with higher thickness from the top to the bottom).

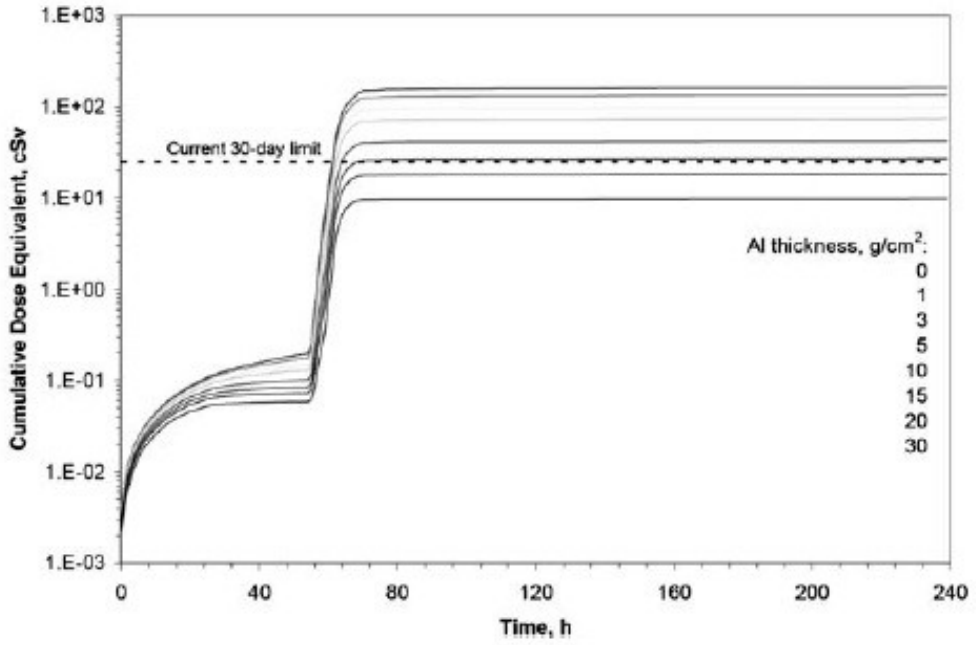

Figure 2.7 - Cumulative dose equivalent of the August 1972 SEP for various shielding thickness of aluminum (increment in thickness is from the top to the bottom). It is worthwhile note the 30-day limit exposure of 0.25 Sv for LEO missions exceeded in few tens of hours [Mewaldt, 2006]

After about 80 h from the onset the SPE ends and there is no more increment of the dose equivalent. It is clear that shielding is effective in reducing the radiation dose from SEP events and that is of fundamental importance to have adequate

systems of monitoring, as real-time detectors, which warn the astronauts of the onset of a SEP, since in few hours the radiation exposure could increase at dramatic levels, especially when astronauts are on EVA.

The measurements of the neutron fluences and the contribution to the total dose remains one of the most difficult task in space radiation dosimetry. Data available about secondary neutron aboard LEO spacecraft reveals that neutrons generated by interactions of GCRs and trapped protons with the spacecraft structure are one of the main components causing radiation hazard for the crew. The neutron total contribution to an astronaut's total dose equivalent for an ISS typical orbit, 51° inclination at ~450 km altitude, ranges from 30% to 60% [Armstrong, 1998] (The quality factor for the neutron is greater than that of protons). Measurements performed on Mir space station by the Granat neutron spectrometer have showed that the majority of the neutron flux aboard spacecraft between about 1 and few tens of MeV, which contributes to the bulk of the total dose from secondary neutrons, is from trapped protons in the SAA interacting with the spacecraft structure [Lyagushin, 1998]. Neutrons below 1 MeV don't contribute sensitively to the neutrons' dose equivalent [Badhwar, 2001]. The production of secondary neutrons inside the spacecraft is strictly correlated with the structure shielding, since it modifies the primary charged particle flux (see paragraph 1.4) according to its thickness and material.

Finally it is showed in figure 2.8 an example of the integral dose equivalent LET spectra measured by TEPC and CR-39 PNTD detectors for the STS-112, STS-114 and STS 121 space missions, in IV exposure. The data gathered by the two detector are well consistent and show about the same dose equivalent all along the three orders of magnitude of the LET.

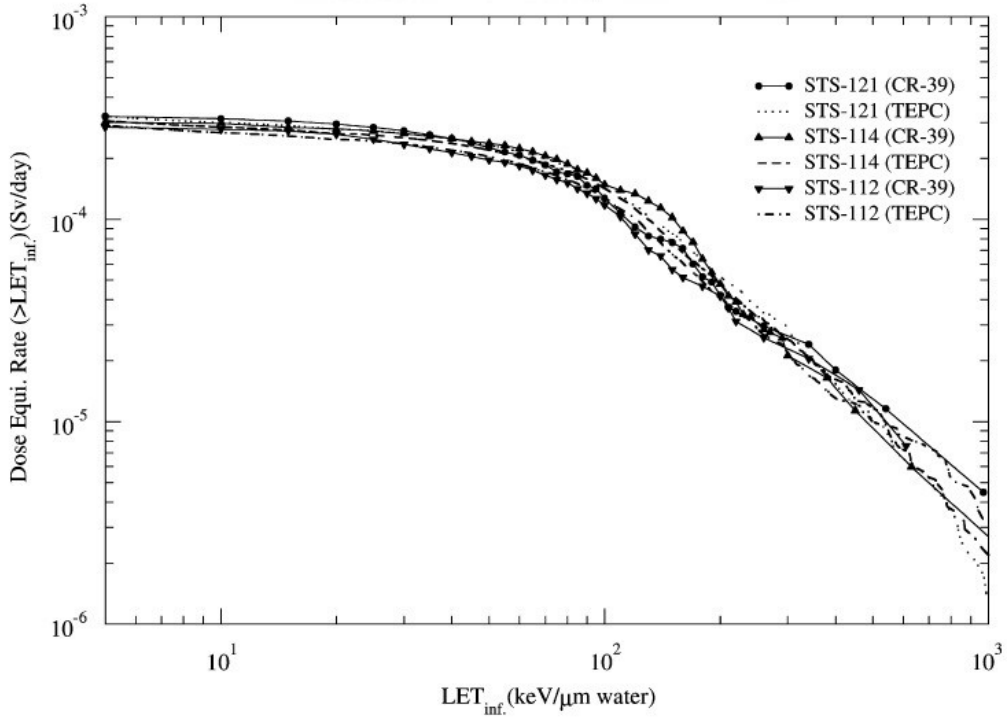

Figure 2.8 - Integral LET spectra of dose equivalent measured by TEPC and CR-39 PNTD for high LET [Zhou, 2007]

Of course variations in the integral spectra tend to occur according to Sun's solar cycle phase, inclination and altitude of the orbit as well as number and power of possible SPEs.

The DOSTEL silicon telescope mounted on top of the head on the Phantom Torso has collected data about the average daily dose both IV and EV. Table 2.3a and table 2.3b show respectively the data obtained from the torso inside and outside the spacecraft for the contribution of GCRs, SAA and the total one [Berger, 2008].

Total average			**GCRs average**			**SAA average**		
μG/d	Q	μSv/d	μG/d	Q	μSv/d	μG/d	Q	μSv/d
194	2.8	535	92	4.4	409	102	1.2	126

Table 2.3a - Dose and dose equivalent for GCRs, SAA and total IV contribution collected by DOSTEL on DosMap (measurements period march-august 2001)

Total average			GCRs average			SAA average		
μG/d	Q	μSv/d	μG/d	Q	μSv/d	μG/d	Q	μSv/d
510	2.5	1265	267	3.1	828	243	1.8	437

Table 2.3b - Dose and dose equivalent for GCRs, SAA and total EV contribution by DOSTEL placed on top of the head of MATROSHKA (measurements period april 2004)

The total average dose equivalent EV is about 2.4 times the IV's, since the lower shielding of the external torso compared wit that inside the ISS. Therefore it is evident that during EVA the hazardousness of the radiation field could be well above the normal dose exposure received by astronauts inside the spacecraft. Besides, energetic SPE can adds more hazard to the contribution of GCRs and SAA, increasing dramatically the dose absorbed by astronauts during EVA even in few hours.

2.3.3 - General results and dose limits

The net flux of cosmic ray radiation that arrives on Earth is well shielded by the atmosphere, equivalent to a 10 m high water column (1000 g/cm^2). A spacecraft provides instead only an average shielding of the order of 20 cm water column (20 g/cm^2) and when astronauts are occupied in EVA the protection of the space suit is equivalent to only to 1.5 cm water column (1.5 g/cm^2).

During the period of low solar activity (solar minimum) astronauts inside spacecraft can undergo a total exposure from radiation up to 1 mSv/d. This value is just quite high if is compared with an average total exposure from natural sources on Earth of about 2.4 mSv/y, due especially to radiation originated from Earth (only 0.3 mSv/y are caused by cosmic ray radiation) [Berger 2008]. During an energetic SPE the exposure can increase up to more than several 100 mSv within a few days. A crew mission aboard ISS is planned to end after about 6 months. Astronauts receive during a mission an average of 80 mSv at solar maximum and of about the double during solar minimum.

Radiation protection for astronauts in LEO deals with biological stochastic effects that are following the exposure in the space, such as genetic effects and risk of cancer induction. The system of radiation protection is based on the guidelines provided by the ICRP [ICRP, 1991]. In table 2.4 it is showed the career effective dose *E* limits for astronauts currently recommended by the National Council on Radiation Protection and Measurements (NCRP) in its Report 132 [NCRP, 2000].

Age of exposure	E (Sv) - Female	E (Sv) - Male
25	0.4	0.7
35	0.6	1.0
45	0.9	1.5
55	1.7	3.0

Table 2.4 - Ten year career effective dose limits for astronauts [NCRP, 2000]

In comparison the career dose limit for occupational workers on Earth is of 20 mSv in one year.

The radiation environment outside and inside spacecraft has been measured for nearly 30 years with a large variety of radiation detectors, but a complete knowledge of the radiation risk in a complex radiation field is still an uncompleted task. New generations of detectors and aimed organ-exposure experiments should permit to collect more useful data of the biological radiation effect and of the risk limits.

CHAPTER III

Microdosimetry and TEPC

3.1 - Theoretical aspects of microdosimetry

In the 1960s Rossi and his colleagues developed microdosimetry by mean of experimental instruments which permit the study of the energy deposition at microscopic level [Rossi, 1959]. Microdosimetry, differently from classical dosimetry, implements stochastic quantities. The stochastic behaviour of energy deposition appears at microscopic level. The energy depositions occur in specific distribution and the biological effects of radiation depends on the microscopic pattern of energy deposition. Microdosimetry provides an energy distribution of this process of energy deposition and not simply a mean value. The International Commission on Radiation Units and Measurements (ICRU) in its report 36 [ICRU, 1983] has defined the microdosimetric quantities used to measure energy deposition (see Appendix I). By means of proportional counters able to simulate microscopic site size (just as TEPC does), it is possible to measure directly the ionization events generated by deposition of energy by radiation passing through the detectors. These detectors are made of special tissue-equivalent plastic and of tissue-equivalent gas which are able to simulate microscopic site size of living tissue. Therefore deposition of energy in these counters is equivalent to the same deposition of energy in a micrometric tissue site. In such a way microdosimetry permits to investigate directly the *quality* of radiation, that is the biological effectiveness of the radiation on living tissue.

3.1.1 - The role of microdosimetry in the space

TEPCs have been used quite recently in comparison with the span of time wherein dosimetry instruments have been implemented for space purposes. Since 1990s TEPC has been adopted by NASA aboard spacecraft, giving a fundamental contribution in the understanding of the space radiation quality. Its main advantage has been the characteristic of being an active detector. This means

that it is able to provide real-time information about the radiation environment and alert when rapid change in the dose spectra occurs due for instance to an upcoming SPE. TEPC measures the lineal energy spectra (see Appendix I) which subsequently can be converted into a LET spectra. Therefore by equation 2.3 it is then possible to obtain the dose equivalent due to a wide range of energy particles and for all kinds of radiation, since the detector is sensitive not only at charged radiation but also at neutrons and photons.

The first TEPC flew on ISS has been the cylindrical detector described in paragraph 2.3.1. NASA will replace the present TEPC with two new TEPCs with a spherical design: a 3.7 cm and a 1.25 cm diameter detectors [Braby, 2010]. Each TEPC will house in a chamber filled with Propane at such a pressure to simulate 2 μm site size. In order to obtain a homogeneous electric field with a spherical geometry the cathode will be segmented and each ring will be set at a specific voltage. The choice of keeping two spherical chamber coupled together come out from the necessity of have good detector response both for low energy and high energy neutrons (see paragraph 5.3.3).

3.1.2 - TEPC used in the space

TEPCs have been used quite recently in comparison with the span of time wherein dosimetry instruments have been implemented for space purposes. Since 1990s TEPC has been adopted by NASA aboard spacecraft, giving a fundamental contribution in the understanding of the space radiation quality. Its main advantage has been the characteristic of being an active detector. This means that it is able to provide real-time information about the radiation environment and alert when rapid change in the dose spectra occurs due for instance to an upcoming SPE. TEPC measures the lineal energy spectra (see Appendix I) which subsequently can be converted into a LET spectra. Therefore by equation 2.3 is then possible to obtain the dose equivalent due to a wide range of energy particles and for all kinds of radiation, since the detector is sensible not only at charged radiation but also at neutrons and photons.

The first TEPC flew on ISS has been the cylindrical detector described in paragraph 2.3.1. NASA will replace the actual TEPC with two new TEPCs with a

spherical design: a 3.7 cm and a 1.25 cm diameter detector [Braby, 2010]. Each TEPC is housed in an individual chamber filled with Propane at such a pressure to simulate 2 μm site size. In order to obtain a homogeneous electric field with a spherical geometry the cathode has been segmented and each ring has been set at a specific voltage. The choice of keeping two spherical chamber coupled together come out from the necessity of have good detector response both for low energy and high energy neutrons (see paragraph 5.3.3).

3.2 - Basics of TEPC functioning

3.2.1 - Introduction

In microdosimetry TEPCs are by far the most common detectors to perform measurements. The TEPC combines both the features of a proportional counter and the properties of a tissue-equivalent detector.

In gas proportional counter the medium of interaction with radiation is a gas-filled chamber. A proportional counter can count the individual ionizing particles that across the gas chamber and measure the total ionization energy produced per particle. Its main characteristic is the ability to amplify a single event (a particle track inside the gas) into a signal proportional to the initial number of ionizations and large enough to be detected, a process called *gas multiplication*, which multiply the single electron for a factor of about $10^3 – 10^4$.

The cathode and the filling gas of a Tissue-Equivalent Proportional Counter are made with materials that have the same elemental composition of the simulated tissue. The energy deposition both from charged and neutral particles depends on the nuclear composition of the material instead of its chemical combination. Therefore it is possible to simulate the tissue by means of special materials for the cathode and gas mixtures for the filling gas that have the same proportion of the elements composing the human tissue, which are H, C, O and N. The most common filling gases used are the methane and propane tissue-equivalent, gas mixtures made by mixing carbon dioxide and nitrogen with methane and propane respectively. In table 3.1 the composition of the two tissue-equivalent mixtures is showed.

	CH_4(%)	C_3H_8(%)	CO_2(%)	N_2(%)
Methane-TE	64.4	0	32.5	3.1
Propane-TE	0	55	39.6	5.4

Table 3.1 - Composition of the two typical tissue-equivalent gas mixtures.

With a TEPC it is possible to simulate a microscopic volume of tissue with a macroscopic cavity. This can be carried out by adjusting the pressure of the filling gas so that the energy deposited by a charged particle crossing the volume of the counter is equal to the energy that the same particle with the same energy deposits crossing a volume of real tissue of microscopic dimension. Let us consider two volumes, one of real tissue and one of tissue-equivalent gas. The energy deposited by a charged particle crossing the volume is given by the product of the material mass stopping power, the material density and the chord length across the volume. Therefore the energy deposited in the tissue volume ΔE_T and in the gas volume ΔE_G can be written respectively as:

$$\Delta E_T = \left(\frac{1}{\rho}\frac{dE}{dx}\right)_T \rho_T \Delta x_T \qquad 3.1$$

$$\Delta E_G = \left(\frac{1}{\rho}\frac{dE}{dx}\right)_G \rho_G \Delta x_G \qquad 3.2$$

where ρ is the density, Δx the chord length of the volume and $dE/\rho dx$ the mass stopping power, respectively for the gas G and the tissue T. Given that the energy deposited in the two volumes has to be the same, the following relation is obtained:

$$\Delta E_T = \Delta E_G \;\rightarrow\; \left(\frac{1}{\rho}\frac{dE}{dx}\right)_T \rho_T \Delta x_T = \left(\frac{1}{\rho}\frac{dE}{dx}\right)_G \rho_G \Delta x_G \qquad 3.3$$

As the mass stopping power of tissue and gas is the same (since the gas is tissue-equivalent), the previous relation become:

$$\rho_T \Delta x_T = \rho_G \Delta x_G \qquad 3.4$$

Writing the previous relation in function of the pressure, one obtains a relation between the gas pressure and the tissue site size:

$$P_G V = R T n \qquad 3.5$$

$$P_G = \frac{\rho_G R T}{M} \qquad 3.6$$

$$P_G = \frac{R T}{M} \rho_T \frac{\Delta x_T}{\Delta x_G} \qquad 3.7$$

where *R=8.314 J/K·mol* is the gas universal constant, *T* the temperature in *K* and *M* is the molar mass in kg/mol. This is an important relation, because enables the detector to simulate different site sizes simply varying the pressure of the gas in the cavity.

Evaluation of dose from TEPC is generally based on application of the Fano theorem, which states that the dose in the cavity is the same as the dose in the material that it has replaced, independently of any difference in density, if the atomic compositions of the cavity and wall are the same, and if the presence of the cavity does not disturb the primary radiation fluence [Attix, 1986].

In order to investigate different interactions between radiation and biological matter the cathode of TEPCs could be made of different conductive plastics. In this work we use A-150 tissue-equivalent conductive plastic, developed at the Physical Science Laboratory Illinois Benedectine College Lisle-Illinois, which correspond to the composition of muscular tissue. Its atomic composition is showed in table 3.2, according to ICRU-36 recommendations [ICRU, 1983].

	H	C	N	O	F	Na	Mg	P	S	K	Ca
Muscular Tissue	10.2	12.3	3.5	72.9	0	0.08	0.08	0.2	0.5	0.3	0.007
A-150 Plastic	10.1	77.6	3,5	5.2	1.7	0	0	0	0	0	1.8

Table 3.2 - Composition in percentage of the A-150 plastic and muscular tissue

The tissue-equivalent cathode performs a very important role in the detector, because it forms the outer shell of the gas cavity. The design and width of the cathode influences the incoming radiation, and these parameters should be specified according to the kind of measurements that have to be made and the kind of radiation environment in which the measure occurs. The wall attenuates the incident radiation, modifying the radiation spectrum that is measured inside the gas cavity. The choice of the wall thickness is essential in order to obtain a good and consistent measurement. In general the wall thickness must be increased with increasing incident radiation energy, but this entails also a reduction of the less energetic radiation, that would be blocked and attenuated by the wall itself. Therefore in a complex radiation field, where a mixture of radiation types and energies is present, it's not simple to reach a good compromise because thicker wall risks to attenuate low energy radiation, but otherwise less tick wall could be not suitable for high energy radiation, since high energy particles will pass the counter without deposition of energy and therefore will not be detected. Since the optimization of the thickness of cathode wall is of primary importance, Monte Carlo simulations are performed for simulating energy depositions and interactions as a function of wall thickness.

3.2.2 - Gas gain and electronic avalanche

As seen above, electrons moving towards the anode undergo a process of multiplication in such a way that the electric pulse formed is both proportional to the energy imparted by the ionizing charged particle and large enough to be detected and separated by electric noise. The process of multiplication is a function of the gas elements, gas pressure and the voltage applied between anode and cathode. The ionizations occurred inside the gas chamber are collected by an electric field between the anode and cathode. The charges are gathered toward the anode, which is composed by a linear wire. The area between cathode and anode can be divided into two regions with different properties: the *drift region* and the *multiplication region* (figure 2.9). In the drift region the ion-electron pairs are created after the crossing of a ionizing charged particle. Then they begin to drift with a velocity depending on the electric field strength and the gas pressure. Electrons move in direction of the anode, sometimes undergo

recombination with positive ions and, if the gas is electronegative, attachment with neutral molecules such as oxygen could also occur, forming a negative ion (for this reason it is important avoid contamination of the counter gas with air).

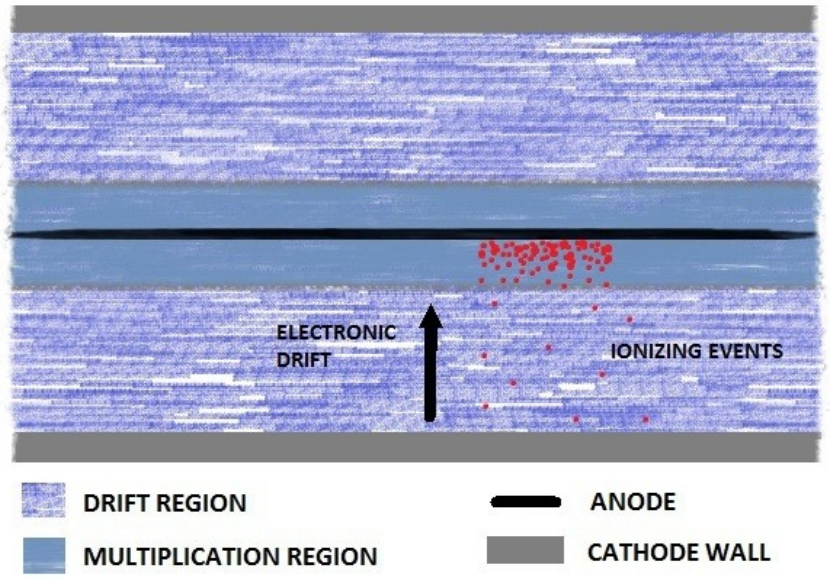

Figure 3.1 - Schematic representation of the ionization process and electrons production in the detector sensitive volume

In the multiplication region electrons gain enough kinetic energy to produce secondary ionization, thank to a high increasing in strength of the electric field. The secondary electrons subsequently produce further ionizations and so on and so forth, creating an avalanche of electrons that amplify the initial signal of various orders of magnitudes. The amount of charge multiplication depends on the ratio *E/p*, the electric field divided by the gas pressure. When *E/p* becomes high enough, ionisation by electrons can occur [Kliauga, 1995]. The electric field *E* for a cylindrical counter can be calculated if the anode radius *a*, the cathode radius *b* and the radial distance *r are* known:

$$E = \frac{V}{r \ln(b/a)} \qquad 3.8$$

where *V* is the anode voltage. The gas gain *G* is the ratio of the number of electrons resulting from the multiplication N and the initial number of electrons N_0 The increment of electron current is proportional to distance travelled and the initial number of electrons. For cylindrical counter with gas gain *G* as previously defined can be showed that:

$$G = \exp\left(\int_{r_a}^{r_c} \alpha(r)\, dr\right) \qquad 3.9$$

where r_a and r_c are respectively the radius of the anode and of the cathode and α is the first Townsend ionization coefficient. It represents the number of ion pairs created by an electron crossing one unit of length in the direction of the electric field. In first approximation the ionization coefficient has to satisfy the Townsend equation:

$$\frac{\alpha}{P_0} = A_0 \exp\left(-\frac{B_0}{E/P_0}\right) \qquad 3.10$$

where B_0 and A_0 are constants that depend on the gas used and P_0 is the pressure of the gas. A more deep gas gain analytical model has been developed by Sègur et al. [Sègur, 1995], in order to describe the ionization mechanism for detector that work at low pressures (few tens of torr or less). In paragraph 5.3.5 we shall use this model to obtain the gas gain calculations for the TEPC

The extent of the multiplication region is one of the main factors determining the energy resolution of a proportional counter. Secondary ionizations produced inside the multiplication volume will generate signals that differ in magnitude depending on the position where the event has occurred. An ideal counter will have a multiplication volume which is very small compared with the total sensitive volume of the detector, in order to minimize the number of events which do not experience a full amplification process. Therefore, minimizing the multiplication region, it is possible to increase the signal resolution. The anode wire radius is another sensible parameter in relation with the gas gain that occur

close to the wire. In cylindrical geometry a very small change in anode radius entails a large change in the electric field close to the anode, especially for small diameter, and therefore a change in gas gain.

3.2.3 – Detector geometry

The spectra and flux of the radiation field that has to be measured influence the choice of the size and geometry of the detector. The size of the cavity is an important parameter in relation with spectra distortion, that is with the capacity of the detector to provide good measurements. Measurements could be affected by the so-called *pile-up* effects that cause an increase of dead time. Pile-up is an effect caused by the overlap of two or more signals, which are detected as one. There are two types of pile-up: the first occurs when two signals are so close that create a single electronic avalanche (the mean time of separation needed in order that two signals produce two different electronic avalanche is of the order of 10-100 ns). One can avoid this pile-up only decreasing the flux of particles entering in the gas cavity. The second is due to the time needed for the elaboration of the signal, a sort of electronic pile-up. The mean time needed to elaborate a signal is about 5-10 μs, with the electronic chain available in our laboratory. In the space the flux of particle is usually low, and therefore sensitive cavity size of some centimeters are used (see paragraph 5.3.2).

The simplest proportional counter design has a cylindrical geometry. This because the most common electrode used to collect electron is a linear wire, which defines an axis of symmetry. For cylindrical geometry the main drawback is the lack of isotropic response with regard to an isotropic external radiation field. The spherical counter has the advantage that, at least at first approximation, it has isotropic response with respect to the external radiation field. This is not completely true because the wire anode along the diameter of the sphere imposes a unique direction in the space, giving a cylindrical geometry to the multiplication region of the counter. If the multiplication region has a small diameter compared to that of the spherical volume of the counter, then it will provide a good spherical symmetry approximation throughout the sensitive volume. Spherical counters have another advantage in comparison with the cylindrical one. The mean random chord length of the distribution is equal for a

spherical or cylindrical geometry whereas in a sphere the variance of the chord lengths distribution is smaller than that of the cylinder. Therefore the deposition of energy in the sphere occurs with a distribution less scattered. The main problem with spherical symmetry is that near the end of the anode the electric field is stronger, because the wall of the sphere, i.e. the cathode, is much closer to the anode and therefore the gas gain is higher than at the center. In order to avoid this problem different solutions have been adopted. The most common is placing a helix wire around the anode wire, so that a kind of grid is interposed between the cathode and the anode. In this way, if the helix is small compared to the sphere diameter but large compared to the anode diameter, one obtains uniform electric field around the anode wire. But in the space it is not possible to use the helix, since vibrations inherent in space station environment would create noise effects and distortions due to the instability of the helix. Another solution uses field-shaping electrodes added to the pole regions of the anode wire [Braby, 1995]. A more complex solution consists in dividing the cathode into rings and then adjusting the potential difference between each ring and the anode, in order to keep constant the electric field near the anode [Braby, 2008].

CHAPTER IV

Experimental set-up for microdosimetry measurements

4.1 - Introduction

This chapter presents both the experimental set-up used in laboratory for performing microdosimetric measurements and the procedure used to generate microdosimetric spectra. The experimental setup can be divided in two parties: the vacuum and gas flow system and the electronic chain. The former consists of a vacuum pump system, used for create vacuum inside the detector chamber, and a gas flow system for the inlet of the gas. The second is composed by the specific electronic chain with preamplifier, amplifiers, ADC and PC. Finally is outlined the method used for create a microdosimetric spectra, once the data has been gathered and stored, using specific software and procedures.

4.2 - Vacuum and gas flow system

A special vacuum system has been opportunely mounted and attached to the detector to produce a vacuum to eliminate all the polluting gases and substances inside the gas chamber. Vacuum is produced with a rotary pump and a turbo molecular pump. The first pump creates a fore-vacuum down to 10^{-3} mbar whereas the latter can reach a lower pressure of about 10^{-6} mbar. The pressure of the system is checked by a Penning (Balzers) manometer placed at the entrance of the pumps. At the same system is connected also the Propane-TE bottle used to introduce the tissue-equivalent gas inside the detector. The gas flow is measured by a device called Mass Flow Controller (MFC), and usually the flow is set to be 1 cm^3/min. The gas pressure has to be as much as possible precise. The whole system is sketched in figure 4.1 and showed in figure 4.2.

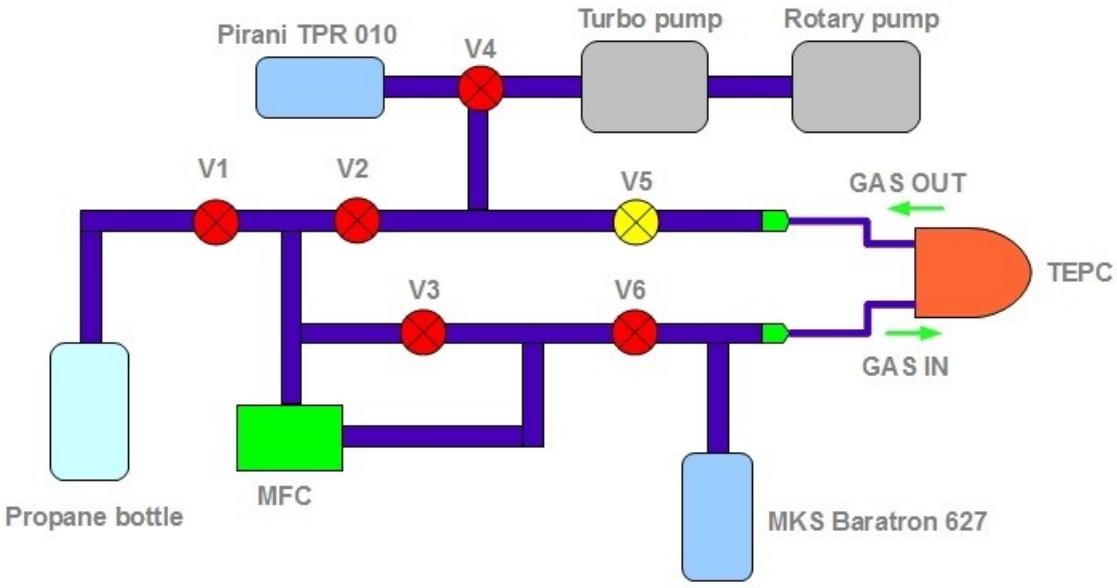

Figure 4.1 – Sketch of the vacuum and gas flow system

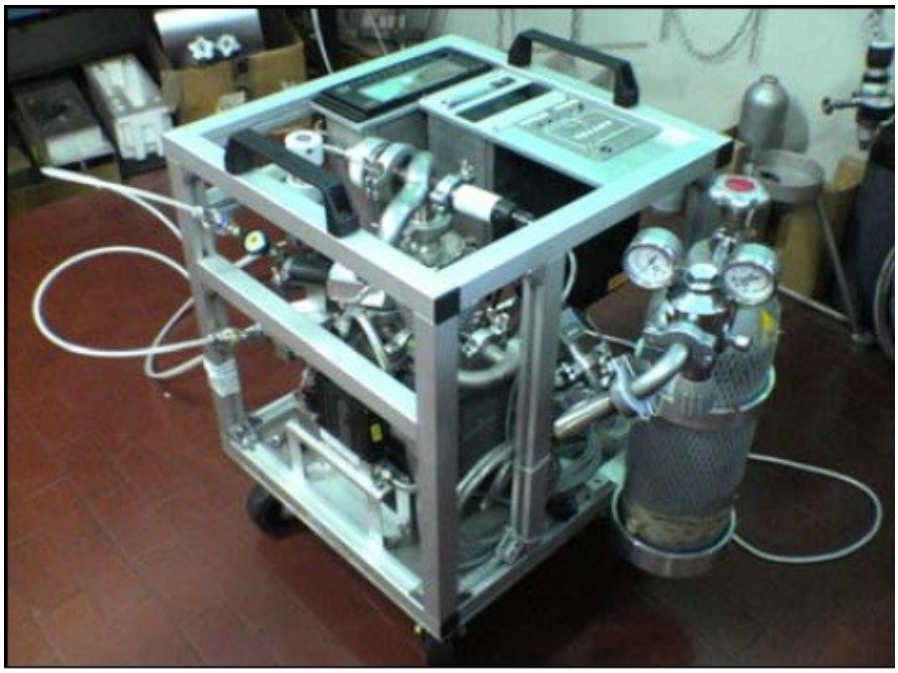

Figure 4.2 – Vacuum and gas flow system used to perform microdosimetric measurements

In order to obtain good microdosimetric measurements it is important to reach a good purity of the gas inside the gas chamber , preventing other polluting gas, as electronegative gases, like oxygen , that reduce the gas gain of the detector. Electronegative gases, like oxygen, are not suitable for TEPCs, given that these gases capture the electrons produced in ionization events, causing a decrease in the number of electrons towards the anode. The gas gain therefore diminishes and the the amplification is significantly compromised. It is essential thus avoid that the filling gas is contaminated by air and water vapour.

4.3 - Electronic chain

The experimental set-up consists in the electronic chain used to link the detector to the acquisition system and the vacuum gas system, needed for create the appropriate gaseous environment.

The task of the electronic chain is to collect the signal coming from the detector and then digitalize and finally store the data in a computer in order to make an offline analysis. In figure 4.3 is represented a scheme of the electronic chain used for the measurement.

The electric field between anode and cathode is supplied by two high voltage generators: HV1 supply voltage to the anode, whereas HV2 to the cathode. The electronic avalanche that occur in the multiplication region and that is gathered by the anode, is converted in a negative pulse. This pulse passes then to a preamplifier PA that is positioned near the detector chamber in order to minimize the noise. The PA is a low noise amplifier and permits the collection of a wide range of signal.

The preamplifier gives in output a positive signal ranging from 0,6 mv to 10 V. It enters three different amplifiers A1, A2 and A3. The signal is divided in three different signals because is needed to achieve a good energy resolution both for small and big ionization events. Therefore three amplifiers are necessary since each one is related to a specific part of the microdosimetric spectra, i.e. respectively *low*, *medium* and *high LET*. The amplifiers filter the signal and shape the signal giving them a Gaussian form.

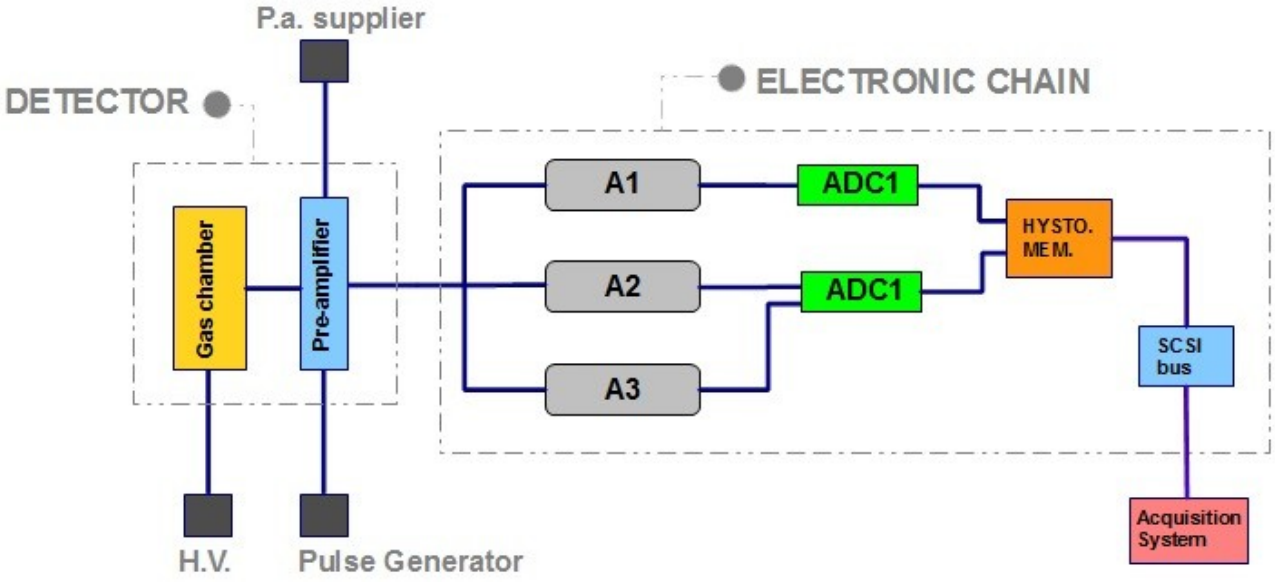

Figure 4.3 – Sketch of the detector configuration and the electronic chain used to perform microdosimetric measurement. The acquisition system consists of the PC and the software used to gather and manage the data.

Once that the signals have been amplified and shaped, they arrive to three different analog-to-digital converters (ADCs). The ADC-1 has 16384 channels and collects low-LET signals, whereas the ADC-2 and ADC-3 have 8192 channels and collects signals respectively of medium and high-LET. Each ADC provides for each channel the number of counts.

Finally the ADC outputs are collected and stored in a CAMAC memory card subsequently transferred to the acquisition system via SCSI-bus. The maximum acquisition rate of the system is 100 kHz, due to CAMAC constraints. The acquisition software is provided by Sparrow Corporation and is called *Kmax*. The outcome of the spectra obtained is a graph that shows counts versus channels. The data so collected undergo offline elaboration for creating microdosimetric spectra.

4.4 - Data acquisition and processing

4.4.1 - Generation of a microdosimetric spectra

The first step in the generation of a microdosimetric spectra consists in obtain a graphical representation in which the distributions of the counts are in logarithmic scale (the recommendations for a correct graphic representation of the microdosimetric spectra are reported in the Report 36 of ICRU [ICRU,1983]). The representation of the spectra in logarithmic scale permits to have a better visual representation of the data, since the most of the counts are due to small events and on the other hand a microdosimetric spectra spans over about 5-6 order of magnitude. After the conversion the normalization of the frequency *f(y)* and dose *d(y)* distribution[3] of the lineal energy *y* must be conserved. The linear and logarithmic differential of *y* are linked by the following equation, respectively for the frequency and dose distribution:

$$f(y)dy = (ln10)\,y\;f(y)\,d(logy) \qquad 4.1a$$

$$d(y)dy = (ln10)\,y\;d(y)\,d(logy) \qquad 4.1b$$

The conservation of the normalization therefore leads to:

$$\int_0^\infty f(y)dy = \int_0^\infty (ln10)\,y\;f(y)\,d(logy) = 1 \qquad 4.2a$$

$$\int_0^\infty d(y)dy = \int_0^\infty (ln10)\,y\;d(y)\,d(logy) = 1 \qquad 4.2b$$

If the logarithmic scale of *y* is subdivided in *B* increments per decade, then the *n*-value of *y* in the new logarithmic scale is:

$$y_n = y_0 \cdot 10^{\frac{n}{B}} \qquad 4.3$$

3 See Appendix I.

Where y_0 is the minimum value of y which has been considered. The logarithmic increment of y then is:

$$\Delta(logy) = \frac{1}{B} \qquad 4.4$$

If the number of increment per decade B is high enough then the difference between $d(logy)$ and $\Delta(logy)$ is negligible, and thus is possible approximate 4.2a and 4.2b:

$$\int_0^\infty (ln10)\, y\ f(y)\, d(logy) = \frac{ln10}{B} \sum_{i=0}^{\infty} y_i \cdot f(y_i) = 1 \qquad 4.5a$$

$$\int_0^\infty (ln10)\, y\ d(y)\, d(logy) = \frac{ln10}{B} \sum_{i=0}^{\infty} y_i \cdot d(y_i) = 1 \qquad 4.5b$$

Finally the i-value of each of the two distributions represented in logarithmic scale and normalized can be calculated as:

$$f(y_i) = \frac{n(y_i)}{\sum_{y_{min}}^{y_{max}} n(y_i)\, \Delta y_i} \qquad 4.6a$$

$$d(y_i) = \frac{n(y_i) f(y_i)}{\sum_{y_{min}}^{y_{max}} y_i n(y_i)\, \Delta y_i} \qquad 4.6b$$

In order to obtain a good number of events for each increment and have a homogeneous representation, an empirical value of B is 60, i.e. each decade has 60 points. The standard representation of a logarithmic spectra is a semi-logarithmic graph, with the lineal energy $y(keV/\mu m)$ in logarithmic scale in the x-axis and in the y-axis $yd(y)$ or $yf(y)$. The first is the usual representation of microdosimetric spectra where equal visual areas correspond to equal doses.

4.4.2 - Spectra calibration

The calibration of the spectra is performed through two different passages: first the calibration in volt and second the calibration in energy. The first step consists in convert the channels in voltage (mV). This task is carried out by a pulse generator, which tests the linearity of the electronic chain and permit the calibration of each spectra in Volt. The pulse generator has four accurate attenuation switches by which it is possible decrease the signal linearly, and therefore obtain a calibration straight line for each of the previously spectra, that is a correspondence volt-channel.

The process of logarithmic representation and volt calibration of each one of the three spectra is performed with KaleidaGraph software through apposite macros.

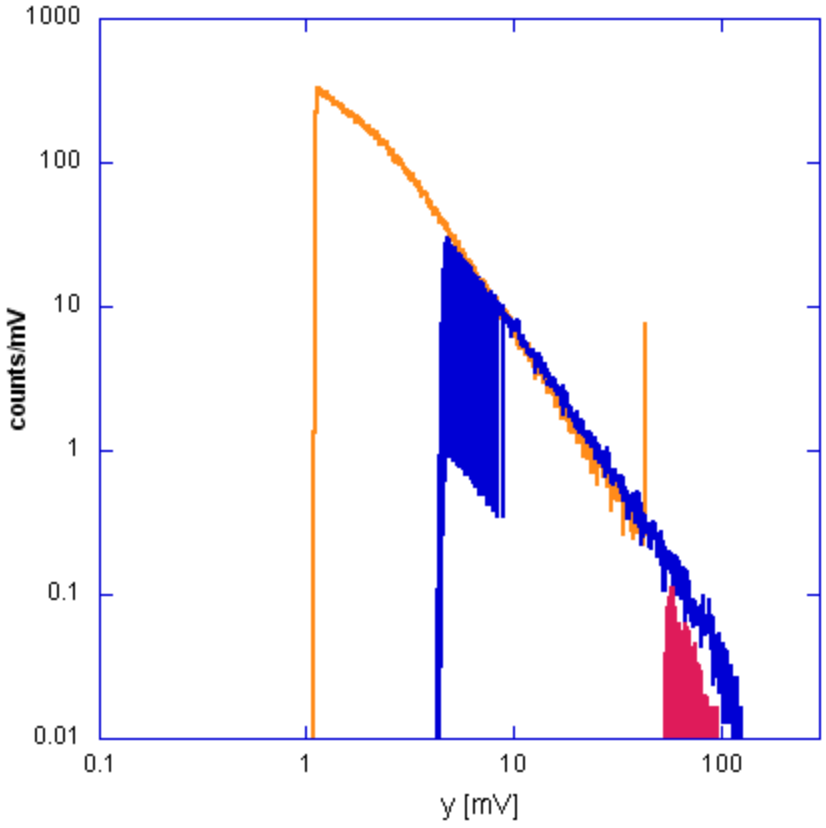

Figure 4.4 – The three spectra calibrated in volt

Figure 4.4 shows the three spectra counts per mV obtained using gamma rays from Cesium-137[4] with the mini-TEPC AMiCo-3[5] developed at LNL-INFN simulating 1 μm tissue site size.

In figure 4.4 we can see that there are two intervals of overlap, since some signals are commons to two sub-spectra (the red spectra (high-LET) in this example is overlapped entirely by the blue one (medium-LET)). In order to create a unique chart the overlapping regions are joined (figure 4.5).

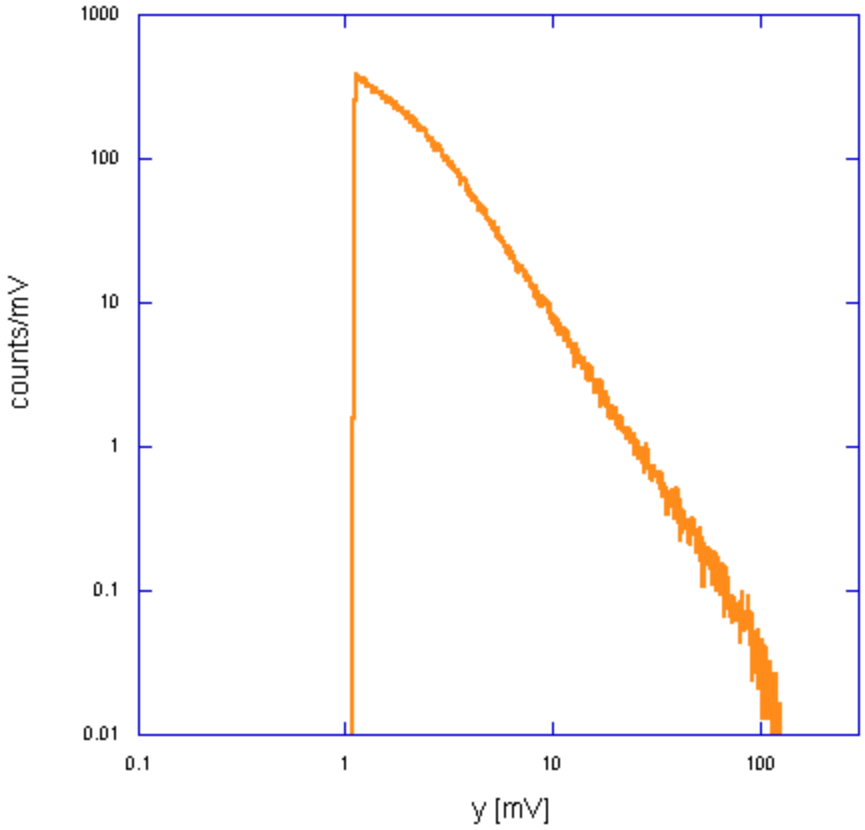

Figure 4.5 – The three spectra joined in a unique chart

Following mathematical calculations reported before and in Appendix I, we obtain a chart *yd(y)* per *y(keV/μm),* represented in figure 4.6.

4 Cesium-137 decays by beta emission to Barium-137 which is responsible for the emission of gamma rays. The photon energy of Ba-137 is 662 keV.

5 Acronym of *Adrotherapy Mini COunter*

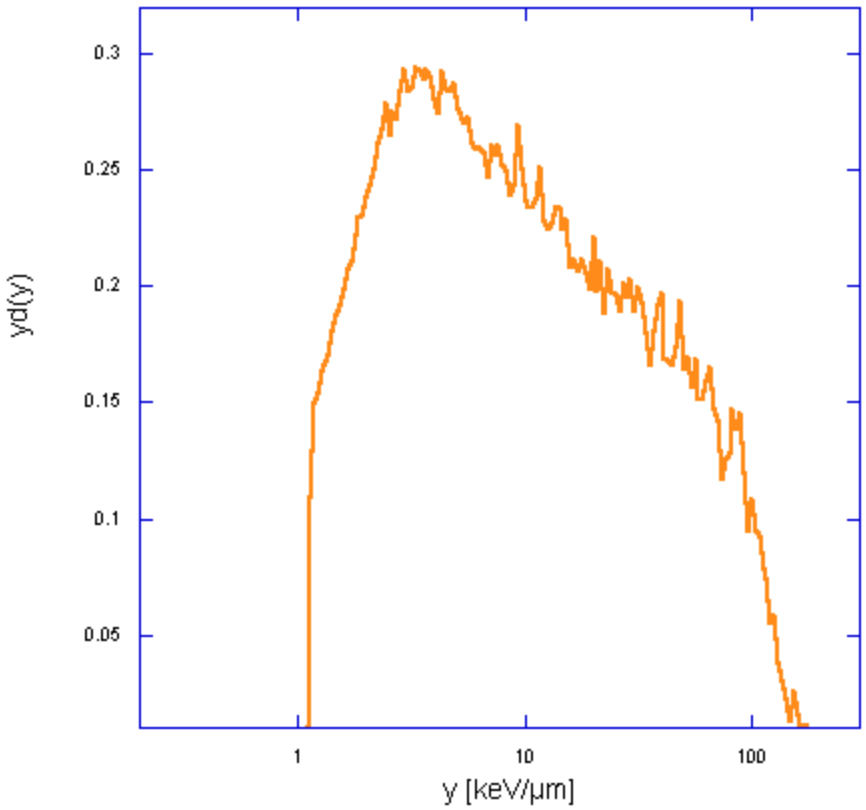

Figure 4.6 – The spectra in yd(y) per y(keV/μm) representation (the spectra is not yet calibrated in energy)

Figure 4.6 has not been calibrated yet in energy. In order to obtain a graph of the dose delivered per lineal energy it is necessary perform the energy calibration, that is associate to a given channel of the spectra a known energy. There are several ways through which it is possible perform a energy calibration. Calibration through detector's internal source can be performed if the detector is irradiated by an internal radiation source whose deposit of energy is well known. Usually are used X-ray sources or alpha particle sources. A second possibility is based on the physical reason that the energy released from charged particles crossing the matter present a maximum at a given point, that is called *particle edge*. The edge will correspond to a specific point in keV/µm in the microdosimetric spectra. Once that this point is known it is possible calibrate the entire lineal energy spectra. Electron and proton edges are commonly used in spectra calibration. Proton edge and electron edge can be calculated for different gas pressure and simulated site size, once that the stopping power for the

particles in that gas is known. Electron edge is used with gamma ray sources (electron edge is independent from the gamma ray source energy and type, depending only by the simulated site size and gas used). In order to determine the point of the edge the second derivative of the microdosimetric spectra of figure 4.6 has been calculated. The second derivative (figure 4.7) presents a peak where the edge occurs, in the right part of the spectra. High statistics of the microdosimetric spectra permits a good definition of this peak (better than 5% [Moro, 2007]). However, once that the value in mV of the second derivative maximum has been determined, the correspondence in energy is obtained. For gamma ray source the electron edge is at 12.6 keV/µm for 1 um simulated site size, which corresponds in the figure 4.7 at 182 mV.

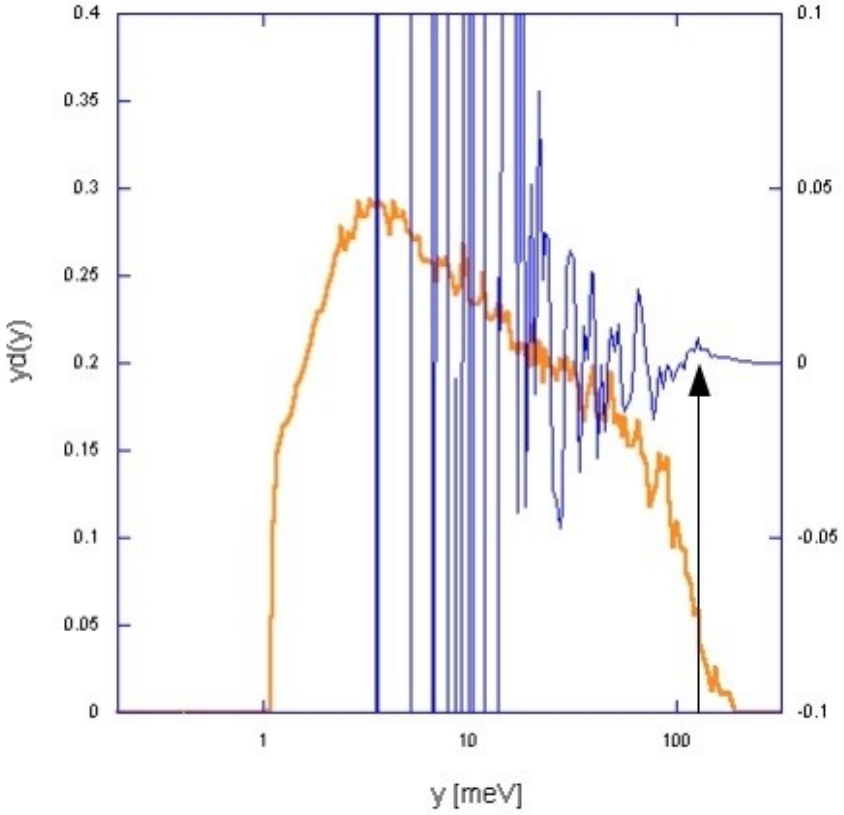

Figure 4.7 – The spectra in yd(y) per y(keV/µm) with its second derivative. The arrow point out the the peak of the electron edge

Finally figure 4.8 shows the final spectra calibrated in energy, in which the electron edge of the spectra has been energy calibrated.

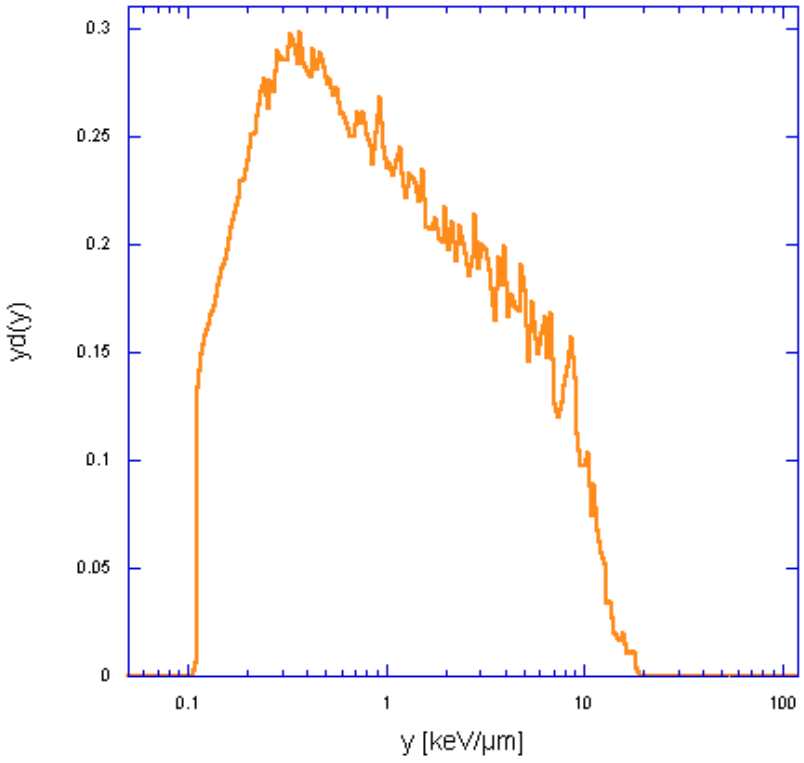

Figure 4.8 – The final spectra calibrated in energy

CHAPTER V

Design of a spherical TEPC for the space

5.1 - The EuCPAD project

In February 2008 the European Columbus laboratory has been launched and has become an integral part of the International Space Station, creating the first European space laboratory dedicated to long-term experimentation. This space research laboratory provides accommodation for experiments which are hosted in ten International Standard Payload Racks (ISPRs). Each rack has the size of a telephone booth and is equipped with its own autonomous and independent laboratory. The European experiment program utilizes both internal and external facilities of the module, and its experimentation regard material science, fluid physics, life science, space science and Earth observation. ESA's concern about space radiation exposure has been realized in an array of facilities and experiments that are already operative aboard Columbus or are scheduled in the incoming years. The study of the radiation effect aboard space stations and spacecraft is a long collection of data gathered on space shuttle's missions, MIR space station and aboard ISS itself. With Columbus module ESA is now able to afford its own long-term program in this field, with experiments in radiation dosimetry that have the purpose to survey and to gather data about space radiation inside and outside the module. The main ESA's external facility is *DOSTEL* (DOSimetric radiation TELescope), that is a small radiation telescope that measure the radiation environment outside the ISS. Internal experiments are *ALTCRISS* (Alteino Long Term monitoring of Cosmic Rays on International Space Station), that study the effect of the shielding on cosmic rays; *Matroshka*, an ESA experiment that was already installed aboard ISS and consists of a human shape equipped with several active and passive dosimeters; *EuCPD* (European Crew Passive Dosimeter) is a set of personal dosimeters worn by the crew to measure the radiation exposure during their flight; and finally there is the *EuCPAD project*, (European Crew Personal Active Dosimeter) an ongoing project for the active monitoring of the space radiation aboard space station and in EVA. EuCPAD

project consists of portable active personal dosimeters based on silicon detectors and of a rack unit in which a Tissue-Equivalent Proportional Counter with a processing unit and a read-out module will be mounted. This module is called PSD (Personal Storage Device) and it is the unit through which the data gathered and stored are displayed to astronauts as numerical values, graphs and audible signals. When a portable detector carried by astronauts is inserted inside the PSD, it stores the new data. In this way, together with the uninterrupted monitoring of the TEPC, astronauts can continuously check the status of the radiation dose personally absorbed and that one present inside the space station.

5.2 – A new TEPC for the space: EuTEPC

This thesis concerns just with the study, design and construction of a prototype of a spherical TEPC for ESA's EuCPAD project. The active TEPC should be able to monitor continuously and in real-time the radiation environment aboard spacecraft and therefore it will be used as a dose-risk alarm during the crew permanency aboard ISS. In paragraph 2.3.1 we have mentioned that aboard ISS a cylindrical TEPC is already present. A new generation of spherical TEPCs is scheduled to be flown, both by NASA [Braby, 2010] and of course by ESA with the EuCPAD project.

Although cylindrical detectors have always worked fairly and they have given proof of strong reliability, their cylindrical symmetry is not the optimal solution in an isotropic environment as the space. Spherical detectors besides are preferred for their isotropic response and for the smaller variance, compared to a cylindrical one, in the energy deposition (see paragraph 3.2.3). Therefore the ideal geometry in space environment is the spherical one, in order to obtain an isotropic response and a better energy resolution.

TEPCs are used in many fields such as in radiation protection, radiobiology and hadron therapy in determining the radiation quality of a broad array of radiation field. For each different application the counter design must be characterized with different specifications. The counter must be optimized with relation to its shape, wall thickness and atomic composition, size, gas multiplication process and type of electronic.

5.3 - Design of the spherical TEPC chamber

5.3.1 - Introduction

In this paragraph the work of study and design of the detector's spherical chamber is presented. Several aspects have to be studied in order to build the appropriate spherical chamber. First of all the physical dimension of the gas chamber and its wall thickness must be chosen taking into account the intensity and the composition of the radiation field inside the space station. The design of the gas chamber is central in the creation of the spherical TEPC. The spherical symmetry is the ideal one for obtain an isotropic response in a non-homogeneous radiation field and in a sphere the variance of the chord lengths distribution is smaller than that of the cylinder: consequently the deposition of energy in the sphere has a distribution less scattered. Another constraint imposed by the space environment regards the impossibility to use any sort of helix or grid to create a uniform electric field along the length of the anode inside the gas chamber, because they will cause huge microphone effects due to the remarkable vibrations present inside the space station. For this reason a special technical solution, consisting in divide the cathode into several rings and setting for each ring a specific voltage, has been adopted. This approach has been used by Braby et al. [Braby, 2009] in the design of the NASA's TEPC and it has been chosen also for this project although with some modification in the design constructions and assembly techniques. To choose the correct voltage for each cathode ring, in order to obtain the needed electrical field configuration, is a task related both with the detector gas gain required and with the gas pressure needed for simulating micrometric tissue site. The gas gain has to be set accurately in relation with the lowest signal that is expected to detect, with the noise due to the electronic and with the dynamic range of the electronic chain. Besides, the separation thickness between the cathode rings and between anode and cathode should not be too small because at small gas pressure the sparking voltage reach its minimum value.

5.3.2 – TEPC dimension and gas pressure

The physical dimension of the gas chamber is related with the flux of the radiation field inside space station and with the gas pressure. The dimension of the detector has to adapt to the flux of the incoming radiation. The physical cross-sectional area of the TEPC should be enough big in order that the particles collected are sufficient to have a good counting statistics. The expected counting rate for protons, both due to primary and secondary radiation, is of about 7.3 protons cm^2/s [EuCPAD private communication]. This value increases of almost 100 times when the ISS passes inside the South Atlantic Anomaly, giving a maximum number of events of 730 protons per second. For such a low flux is possible set a radius of the detector gas chamber of some centimeters. In this project it has been chosen to work with a radius of 2.5 cm, which in turn means have a detector cross-sectional area of about 20 cm^2. Once fixed the radius of the detector it is possible to calculate the gas pressure needed to simulate a micrometric tissue site size. Recalling the equation 3.7 for the simulation of a microscopic tissue site size we are able to manage the calculation for the correct pressure for a TEPC of 5 cm diameter and the temperature fixed to about T = 20°C. At 1μm and 2 μm the gas pressure inside the counter cavity should be respectively 8.09 torr and 16.18 torr for C_3H_8 gas, and 8.33 torr or 16.66 torr for C_3H_8-TE gas mixture.

5.3.3 - Wall thickness

The wall thickness of the cathode is an important parameter, since it is involved in the number of interactions of indirectly ionizing particle such as neutrons. Neutrons produced by the interaction between galactic cosmic rays and spacecraft structure are responsible for a very important portion of the dose received by astronauts. The neutron energy spectrum depends of the incident charged particle spectrum and the scattering environment, but generally extends to beyond 100 MeV. To achieve ideal neutron dosimetry the cathode wall thickness should be at least as thick as the range of a proton having the maximum energy of the neutrons to be monitored. This proton range is 0.1 cm in tissue-equivalent material generated by 10 MeV primary neutrons and 7.6 cm for 100 MeV

neutrons [Braby, 2010]. A wall thickness of 7.6 cm is not reasonable in a TEPC for space applications, because of weight and size constraints imposed by the space environment. Besides, thick walls would attenuate the lower energetic neutrons, resulting in an underestimation of their contribution to the total dose. In practice it is not possible to use a wall thickness that provides an ideal response for all the energies considered, and a compromise is unavoidable. Simulations of the deposition of energy in the detector wall and gas cavity has been performed with Monte Carlo codes for neutrons and protons, which contributes practically to the inside total absorbed dose. The simulations take into account different thickness for the A-150 plastic that forms the cathode wall, ranging from 4 to 7 mm. Two layers of aluminium are also present externally, of 2 mm and 5 mm, which represent the external envelope of the TEPC. In the simulations has been used gas simulating tissue site size of 2 μm.

Figure 5.1 and 5.2 shows the data for neutrons and protons (for all the range of energy) for various thickness of A-150 plastic. The graphs are normalized to one. The contribution of each component to the total dose is showed in figure 5.3, where this time the graph is normalized to dose rate/day. The proton contribution in comparison with the total contribution is the same below 10 keV/μm, whereas above 20 keV/μm neutron contribution is comparable to which of protons. As it can be seen in figure 5.2, proton contribution is independent by A-150 thickness whereas neutron contribution (figure 5.1) varies slightly with y between 1 and 100. This is due to the contribution of neutron of different energy. In figure 5.4 dependence of neutron lineal energy deposition by A-150 thickness is showed for monoenergetic neutrons of 1 MeV and of 100 MeV. As final result is possible to state that energy deposition by neutrons and protons is independent by A-150 thickness in the range of 4-7 mm.

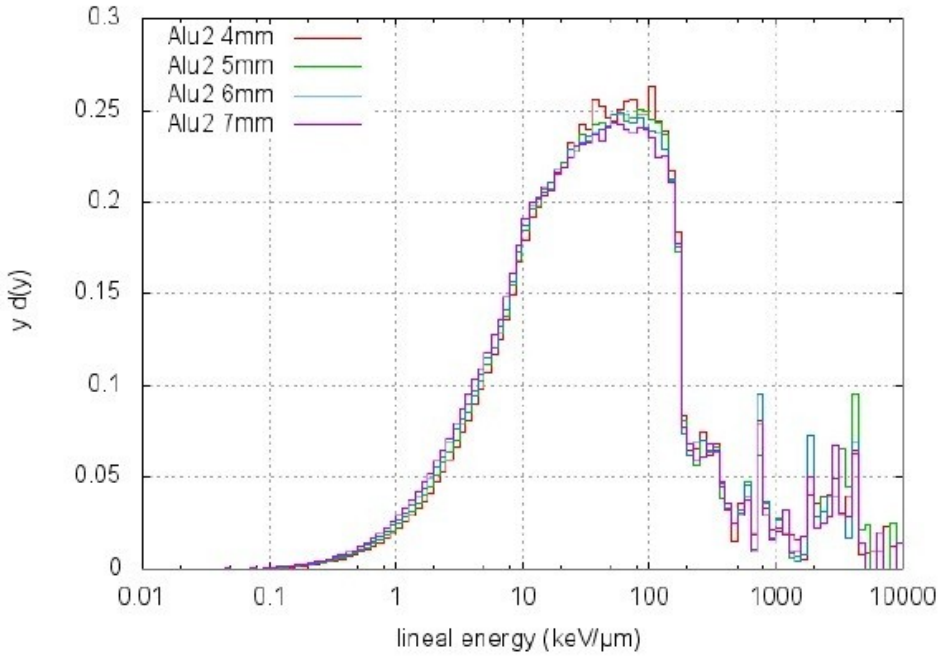

Figure 5.1 – Simulations of the TEPC spectra for neutrons for different A-150 plastic thickness [EuCPAD private communication]

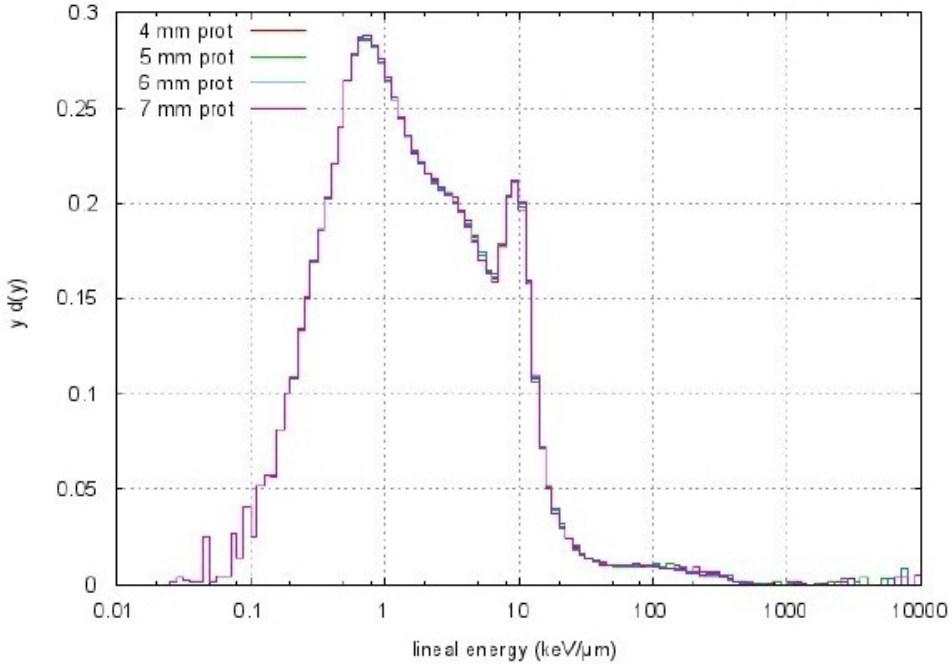

Figure 5.2 – Simulations of the TEPC spectra for protons for different A-150 plastic thickness [EuCPAD private communication]

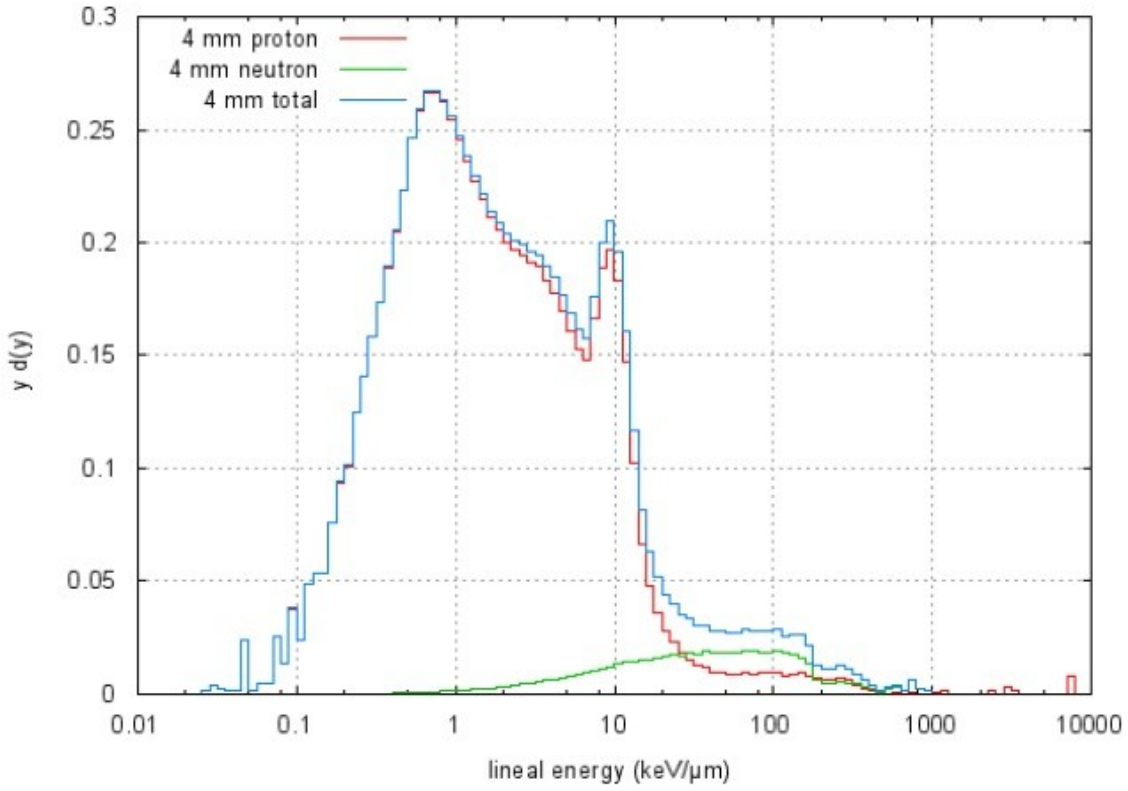

Figure 5.3 – Contribution of each component to the total dose for 4 mm A-150 plastic (the graph is normalized to dose rate/day) [EuCPAD private communication]

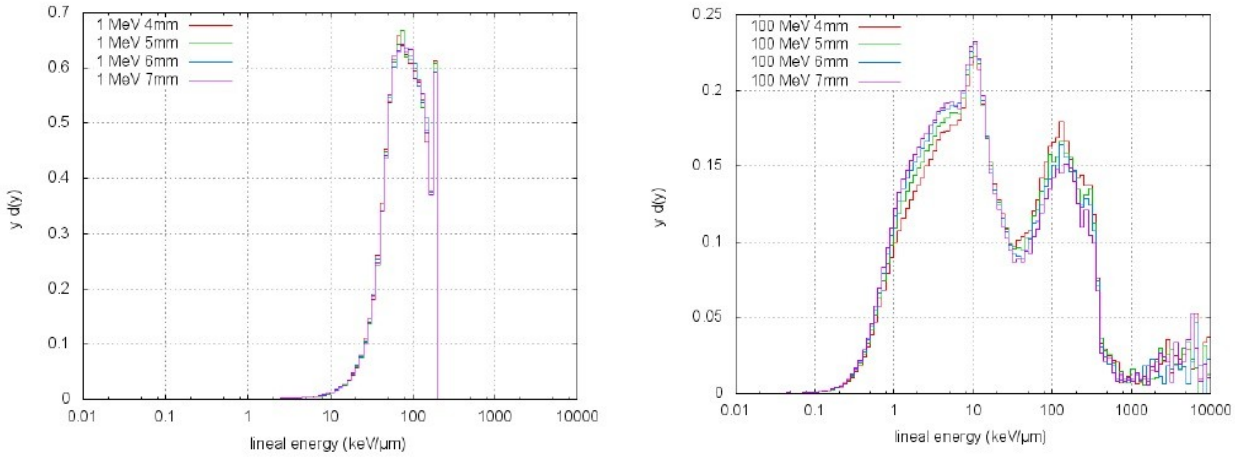

Figure 5.4 – Dependence of lineal energy deposition by monoenergetic neutrons of 1 MeV (left) and of 100 MeV (right) for A-150 plastic 4 mm thickness [EuCPAD private communication]

5.3.4 - Segmented wall configuration

In the paragraph 3.2.4 it has already been mentioned that in a simple spherical detector the electric field is not uniform along the anode wire, because the distance between the cathode and anode wire is not constant. In order to create a constant electric field a segmentation of the cathode has been foresee. The determination of the number of sectors, their shape and their dimension, spacing and potential difference between each sector and the anode necessary to achieve the uniformity of the electric field has been investigated. The modelling of the TEPC and the calculation of the electric potential inside it have been performed by means of the software FlexPDE 6 [www.pdesolutions.com], a partial differential equations solver by the finite element method. As the spherical TEPC has a cylindrical symmetry around the anode wire, the modelling of the detector has been performed in axisymmetric cylindrical coordinates (R, Z): in the following plots the rotation axis, corresponding to the location of the anode wire, is the Z coordinate. The anode wire is placed along the ordinate of the plot and the radial position R is along the abscissa. The software has been employed to calculate the electrostatic potential V inside the counter by solving the electrostatic field equation:

$$\nabla \cdot (\varepsilon \nabla V) = 0 \qquad 5.1$$

It has been found that, for a 50 mm diameter TEPC, the subdivision of the cathode wall into 9 sectors is sufficient to assure a good uniformity of the electric field. In figure 5.5 the layout of the lower half hemisphere of the TEPC is represented. The 3 mm thick cathode wall made of A150 tissue-equivalent plastic is subdivided into 5 sectors (C1, C2, C3, C4, C5), separated by thin insulator layers of 0.4 mm (made of Rexolite® 1422, which is a special insulating plastic with tissue-equivalent properties). Around the cathode, a Rexolite shell of 3 mm thickness is also represented. Its function is both to isolate the cathode from the external shielding of the detector, to assure the desired thickness to the detector wall (as Rexolite composition is very similar to that of A150) and to press together all 9 cathode electrode.

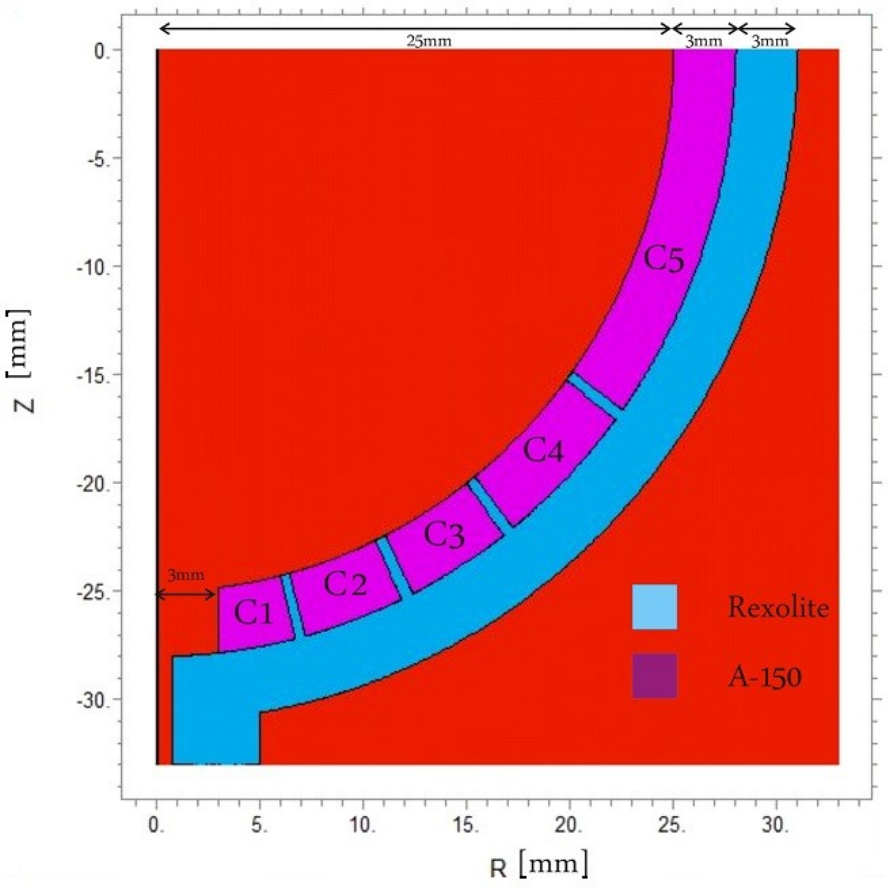

C5 = 1

C4 = 0.96

C3 = 0.91

C2 = 0.84

C1 = 0.67

ANODE = 0

Figure 5.5 - Cathode rings and the voltage bias relative to that given to C5, set for each ring. Are displayed also the distance between anode and cathode and the separation between each ring.

The simulation with FlexPDE 6 is presented in figure 5.6, which shows the half hemisphere of the TEPC. The field lines are parallel to the Z axis, apart small deviations near the detector wall. The configuration of the simulation has been obtained setting at 0 V the anode and biasing the cathodes according to the value of figure 5.5 with the cathode C5 set at -700 V. It is worthwhile to notice that the dependence of the electric potential along the diameter of the counter has the same trend as in a cylindrical counter. In figure 5.6 the radial dependence of the electric potential along the diameter of the counter (Z=0) is plotted, together with its best fit obtained using the equation giving the electric potential dependence in a cylindrical counter:

$$V(R) = -\frac{\Delta V}{\ln\left(\frac{r_c}{r_a}\right)} \cdot \ln\left(\frac{R}{r_a}\right) \qquad 5.2$$

where ΔV is the voltage between anode and cathode, r_a is the anode radius, r_c is the cathode radius. The electric potential of the spherical counter biased at ΔV=700V is equivalent, according to the values of the best fit parameters, to the potential of a cylindrical counter of the same diameter biased at ΔV=703V. The correlation between the two electric potential is as good as R=0.99996.

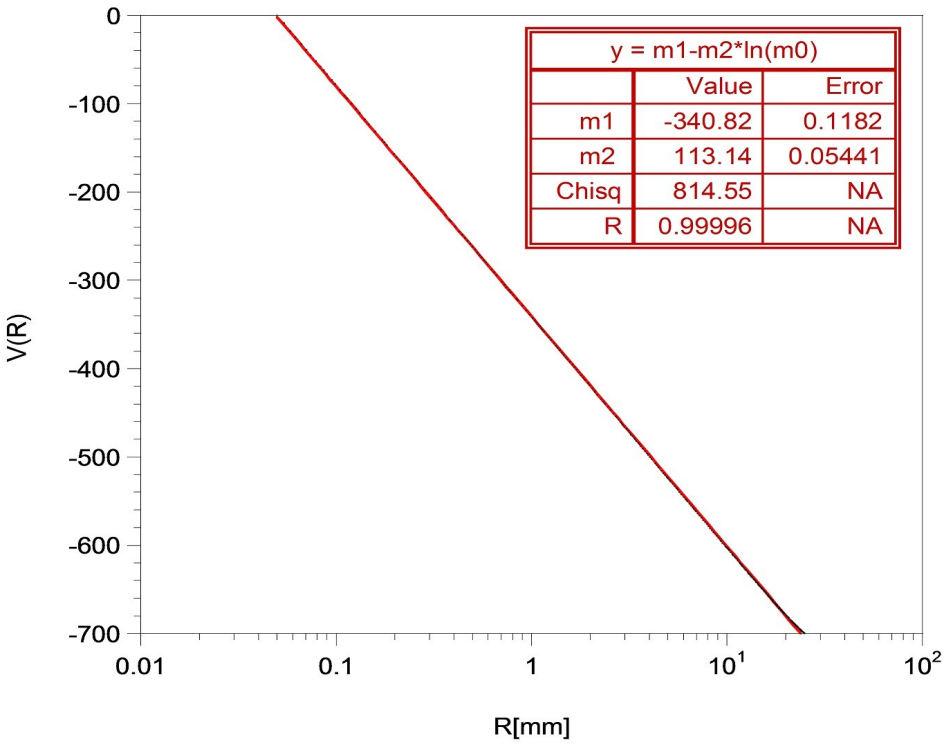

Figure 5.6 - Radial dependence of the electric potential along the diameter (black points) with its best logarithmic fit obtained using the equation 5.1 (red line)

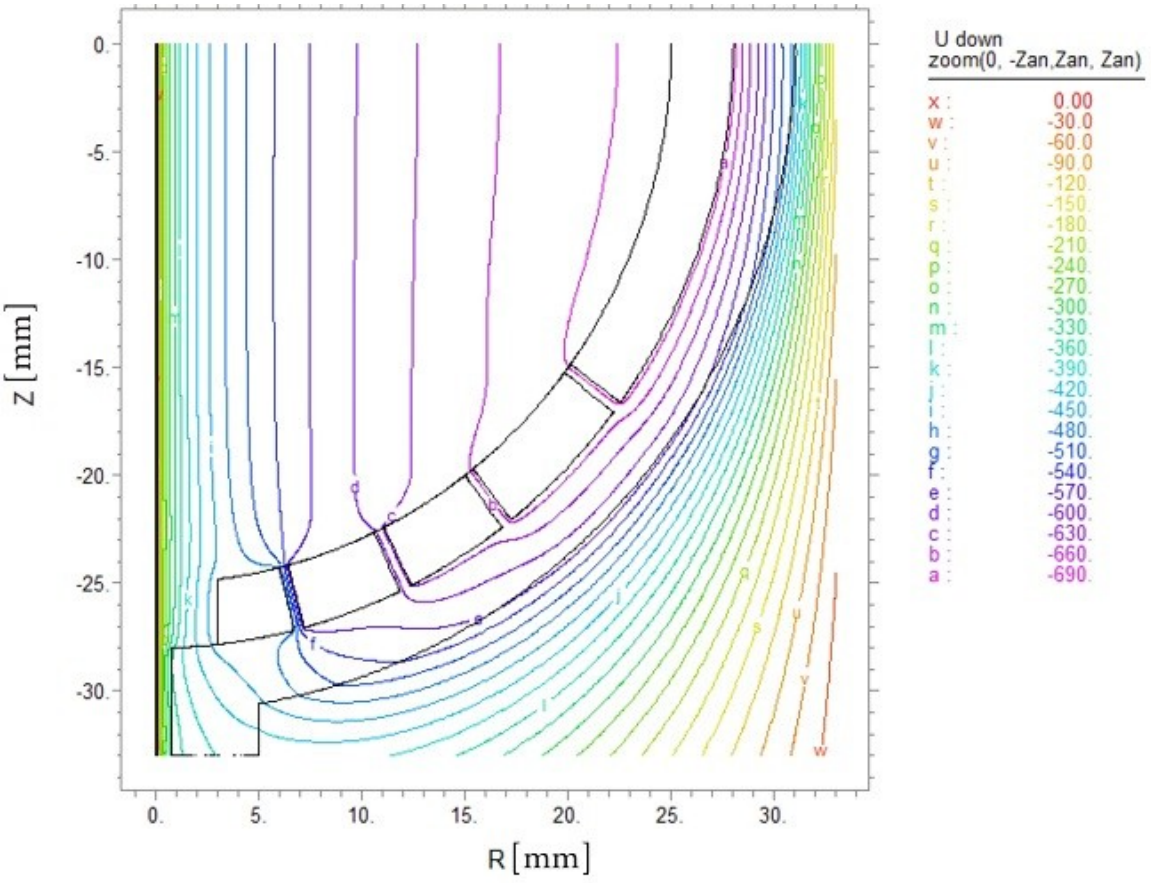

Figure 5.7 - Simulation of the equipotential electric field lines of the segmented cathode wall. The anode is set at 0 V, whereas the cathode C1, C2, C3, C4 and C5 are biased according to the values set in figure 5.5 with the cathode C5 set at -700 V.

Besides the result obtained from the simulation is independent by the value of the voltage applied to the cathode C5. This means that the equipotential lines will present the same structure as the voltage ratios between the different cathodes are only dependent from geometrical parameters and not from the voltage applied to C5.

5.3.5 - Detector gain

The gas gain is a variable determined by various constraints both electronic and physical. Once the voltages of the cathode rings and of the anode have been set, and the gas pressure fixed, the gas gain is determined. The phenomenon of gas ionization has been already introduced in the paragraph 3.2.2, where has been introduced the general formulation theory of gas gain by Segur et al. [Segur, 1995]. In the following we use this gas gain analytical model for the calculations of the detector's gas gain. Gas gain calculations have been performed on a code developed for cylindrical counters, but as seen in the previous paragraph the equipotential field lines for the spherical TEPC have the same pattern of the cylindrical TEPC. Simulations of the gas gain have been made for Propane C_3H_8 and for Propane-based tissue-equivalent C_3H_8-TE both at 1 μm and 2 μm site size. From equation 3.7 at a temperature of 20°C the gas pressure inside the cavity for simulate 1 μm and 2 μm site size is of 8.09 torr and 16.18 torr respectively for C_3H_8 gas and 8.33 torr and 16.66 torr respectively for C_3H_8-TE gas mixture.
Following the gas gain analytical model by Sègur et al. the gas gain *G* for a cylindrical counter is:

$$\frac{\ln G}{K} = \frac{L}{(1-m)\cdot M \cdot V_i}\left[\exp(-M\cdot S_a^{\,m-1} - \exp(M\cdot S_c^{\,m-1})\right] \qquad 5.3$$

Where:

$$K = \frac{\Delta V}{\ln\left(\frac{r_c}{r_a}\right)} \qquad S_a = \frac{K}{r_a\ N} \qquad S_c = \frac{K}{r_c\ N} \qquad M = \frac{L\ K}{V_i}\exp\left(\frac{V_i}{K} - 1\right) \qquad 5,4$$

ΔV is the voltage difference between anode and cathode C5, r_c and r_a are respectively the cathode and anode radius, N is the gas molecular density and L, V_i and m are constants depending on gas characteristics (the values of the constant for normal Propane and Propane-TE used for the calculations have been taken respectively from Alkaa et al. [Alkaa, 2000] and obtained from Monte-Carlo simulations by Mitev et al. [Mitev, 2005]. Gas gain calculations for C_3H_8 gas simulating 1 μm and 2 μm (respectively 8.09 torr and 16.18 torr) for different anode diameter are presented in figure 5.8 and 5.9. The cathode voltage has been set respectively at 700 V and 800 V. In figure 5.10 and 5.11 the same calculations for different anode diameter but with C_3H_8-TE gas at respectively 8.33 torr and 16.66 torr are showed.

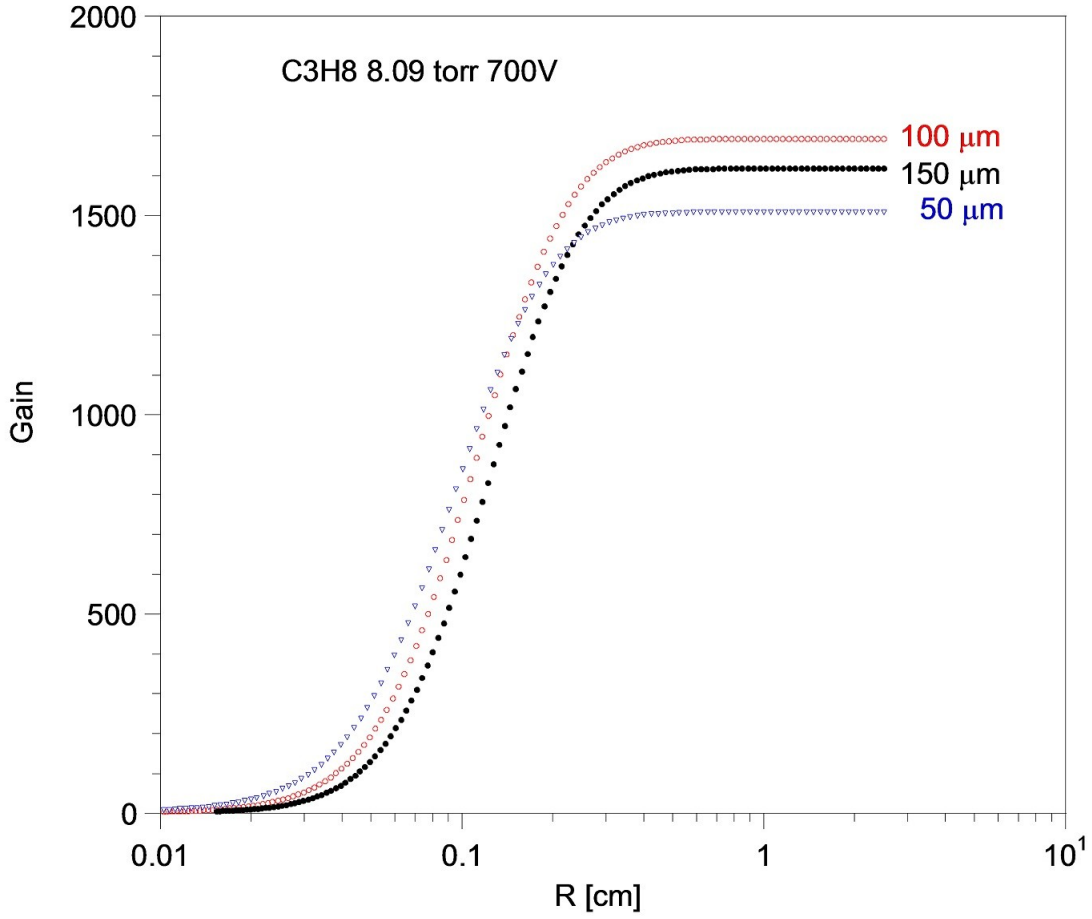

Figure 5.8 - Gas gain for C_3H_8 gas simulating 1 μm at 700 V tissue for different anode diameter.

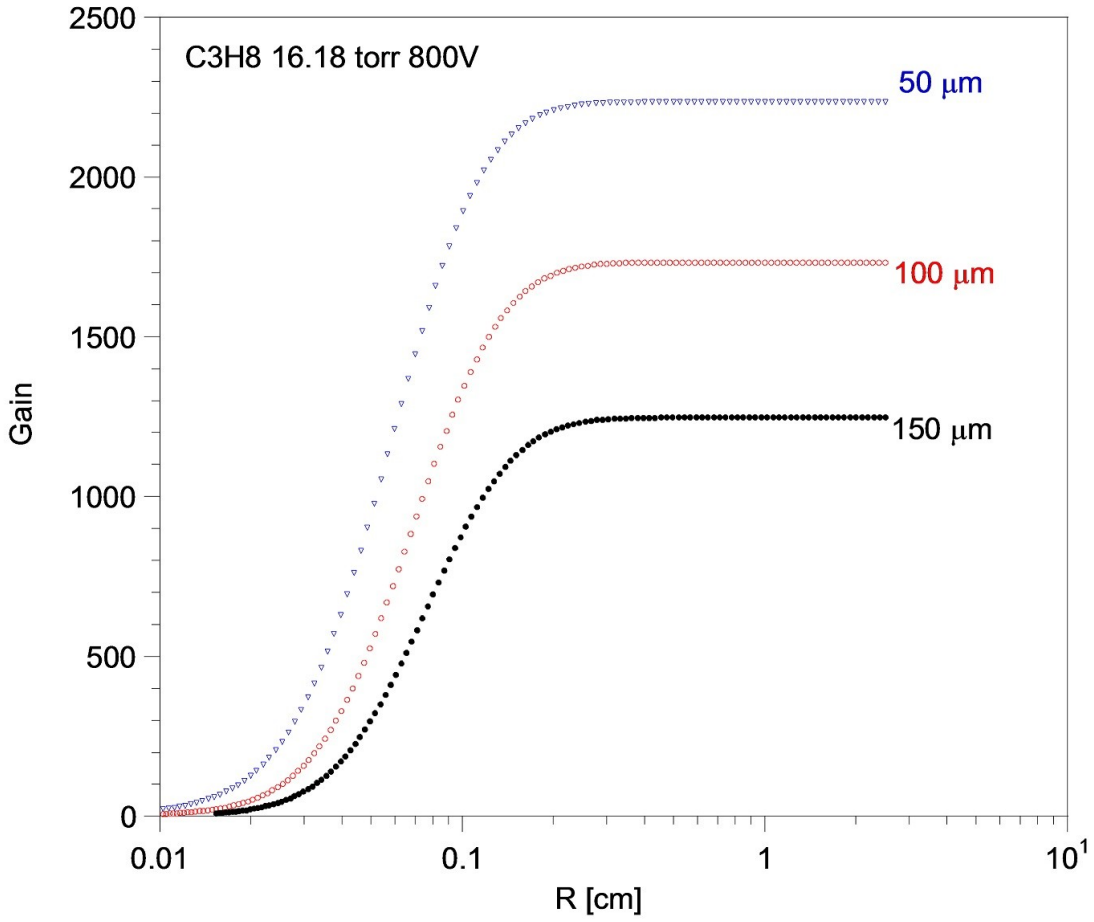

Figure 5.9 - Gas gain for C_3H_8 gas simulating 2 μm at 800 V tissue for different anode diameter.

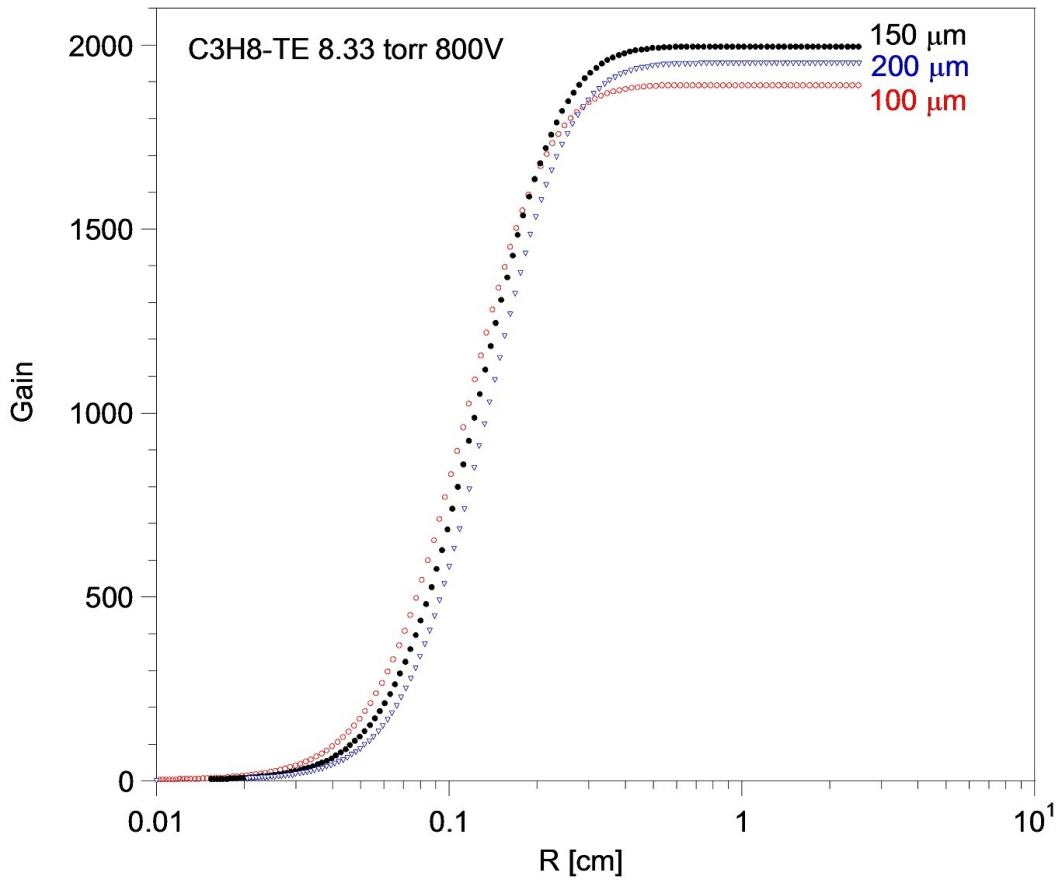

Figure 5.10 - Gas gain for C_3H_8-TE gas simulating 1 μm at 800 V tissue for different anode diameter.

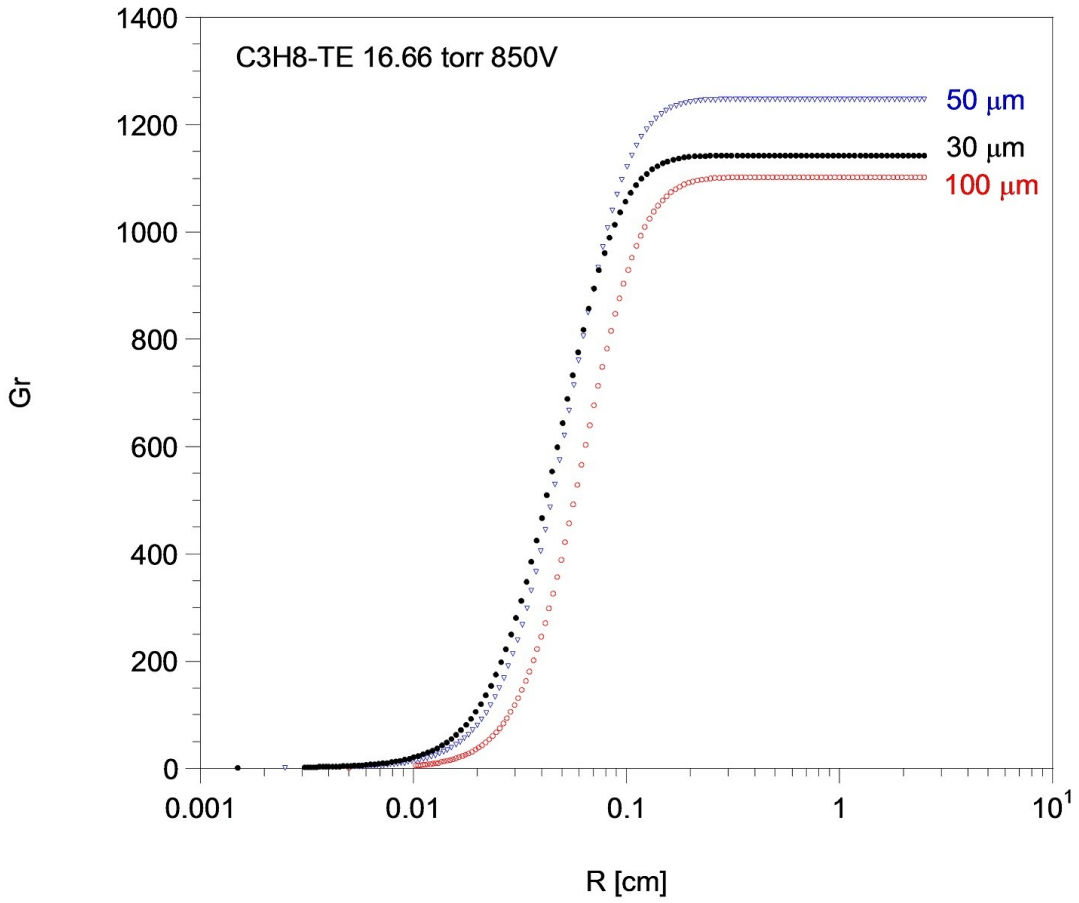

Figure 5.11 - Gas gain for C_3H_8-TE gas simulating 2 µm at 850 V tissue for different anode diameter.

Finally figure 5.12 and 5.13 show the simulations of gas gain for C_3H_8 gas simulating respectively 1 µm and 2 µm for 100 µm anode wire and for different cathode voltages. It has been chosen to use an anode wire of 100 µm diameter because it allows achieving a good gain both at 1 µm and 2 µm simulated site size.

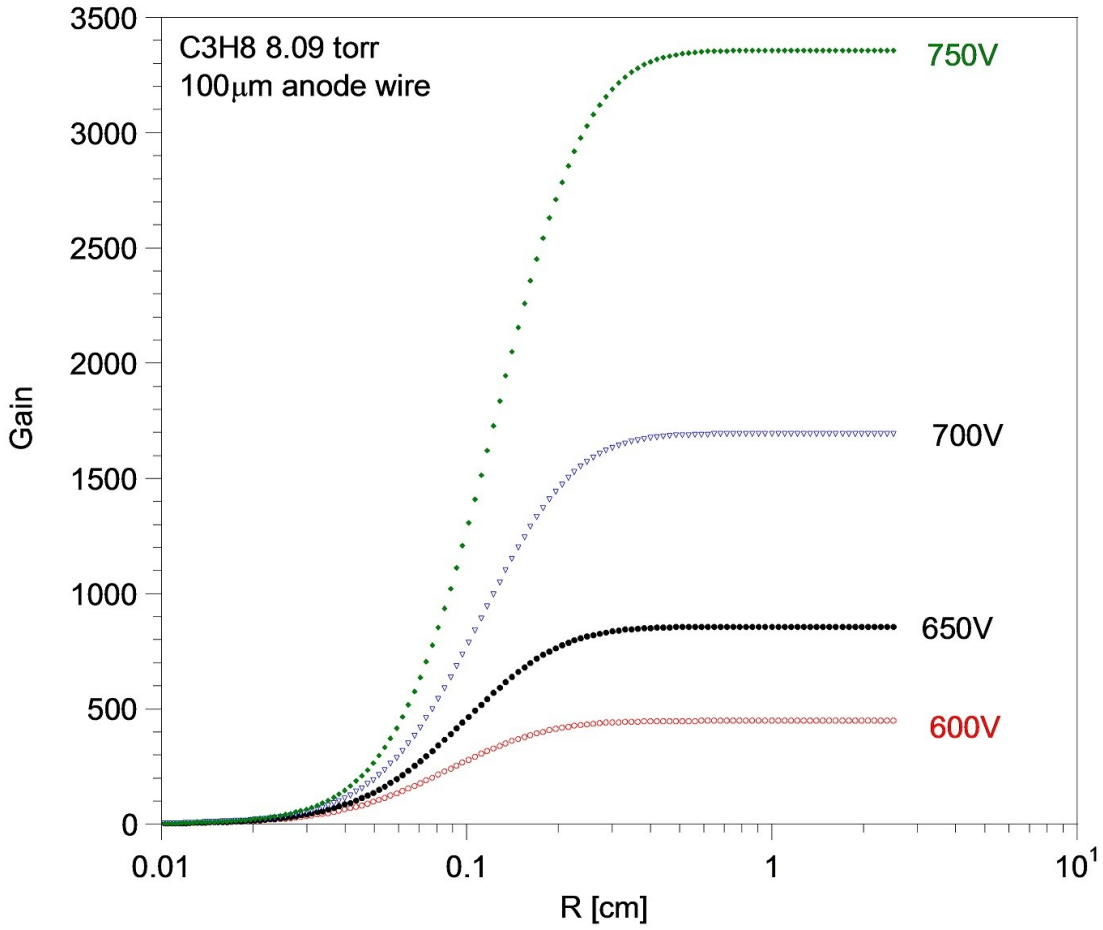

Figure 5.12 - Gas gain for C_3H_8 gas simulating 1 μm tissue for different cathode voltage with 100 μm anode diameter

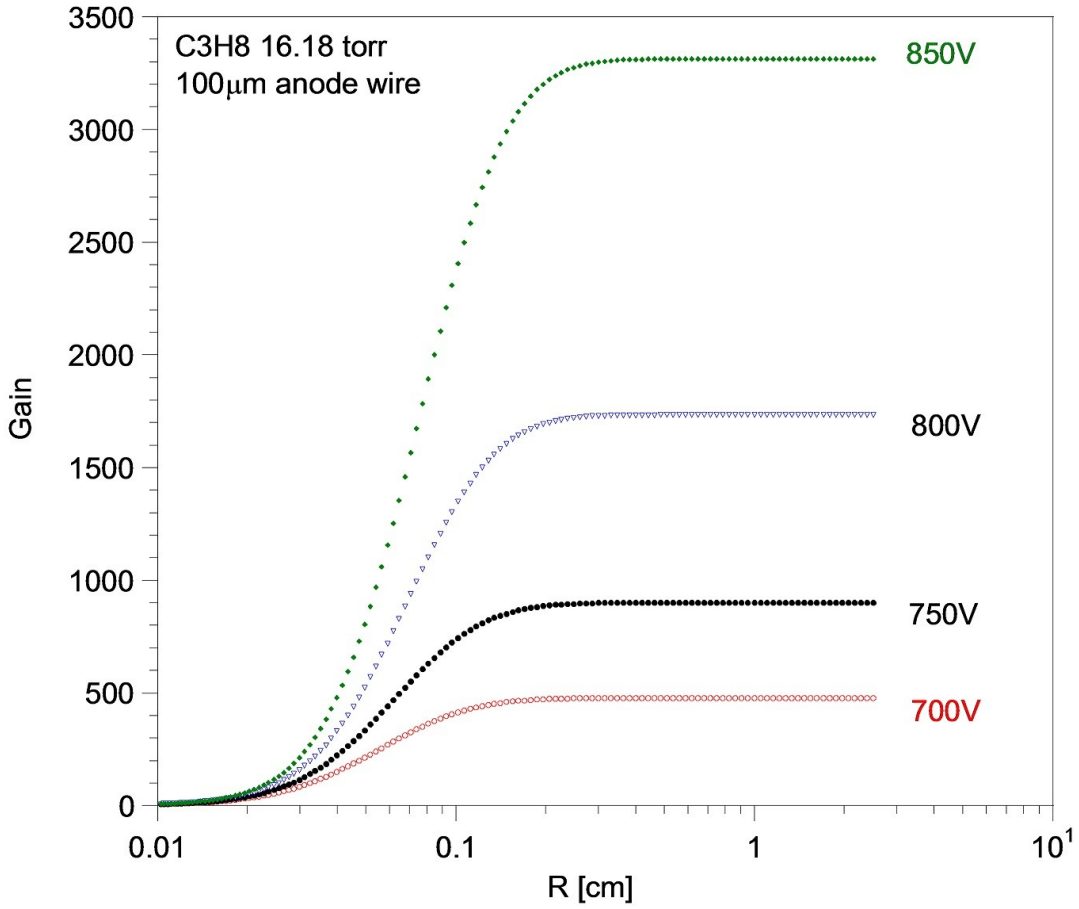

Figure 5.13 - Gas gain for C_3H_8 gas simulating 2 μm tissue for different cathode voltage with 100 μm anode diameter

What results from the simulations is that the Propane reach a higher gain in comparison with the Propane-TE for the same voltage applied, that is for the same simulated site size higher voltages are required with C_3H_8-TE for obtain the same gas gain of C_3H_8. As we shall see in the next paragraph this entails the drawback of have major probabilities of discharge processes. From figure 5.8 and 5.9 what results is that with C_3H_8 gas simulating 1 μm at 700 V the gas gain is maximized with anode wire size set at 100 μm, while at 2 μm simulated size the gas gain is maximized by an anode wire diameter of about 50 μm (these values are also slightly dependent on the applied voltage). The thickness of the anode

wire is very important, since thicker anode assure a better stability of the detector gain, given that the effective diameter of the anode wire may change during the lifespan of the detector. Irradiated gas can suffer *ageing* and thus can change their physical properties. Ageing effect occurs since without gas flow system, long-period of use of the same gas might cause alteration in the composition of the gas due to polymerization and creation of negative ions that would drift toward the anode and would accumulate on its surface, increasing slowly the anode diameter and causing thus alteration in gas gain. In order to avoid this effect is preferable work with thicker anode diameter. But since in the space usually there is low space radiation flux the ageing effect is negligible even for about 2-3 years of use of the same gas.

In figure 5.12 for 700 V cathode it is noticeable that the maximum gas gain is reached as far as 4 mm from the anode, i.e. the avalanche region is as big as the value of R at which the gas gain remain constant. This means that electrons generated from ionization events occurring below this distance will undergo less gas gain, and therefore the anode signal for this events will not be the same for a similar event occurring above 4 mm. This entails that ionization events inside the cylindrical volume with 4 mm of radius around the anode will undergo a distorted gain. However the ratio between this volume and the total volume of the gas chamber is very small, about 0.04. This distortion can therefore be neglected. The choice of use normal Propane depend also by the necessity of have a gas which components are less inclined to change their properties by pollution from outgassing effect and interaction with radiation. Normal Propane is composed by the only molecule of C_3H_8 whereas C_3H_8-TE contains also CO_2 and N_2. This entails different rate of variation for each molecule and therefore C_3H_8-TE is subject to change its composition properties more quickly than normal Propane. Since the stability of the gas in the TEPC is fundamental to allow a correct usage of the detector for about 2-3 years, the choice of employ Propane is required.

What comes out from the simulations of figure 5.12 and 5.13 is that the choice of gas pressure, and consequently of the gas gain obtained, has to be chosen according to maximum voltage applicable imposed by discharge processes, the desired range in lineal energy and the electronic noise of the electronic chain (paragraph 5.4.2).

5.3.6 – Electric field and discharges

The voltage bias between each couple of cathode and between the cathode C1 and the anode has however the drawback of prompt possible electric discharges, due to the high voltage used, the small distances between the segments of the cathode and the low pressure of the tissue-equivalent gas. The difference set for the voltage between each rings is bound by their separation distance. This constraint can be determined by the *Paschen curve,* which describes the effect of discharge of an electrode in a gas medium with a given pressure. Decreasing the pressure of the gas could provoke a discharge between the electrodes of the detector if they are very close. The TEPC suffers of this drawback both close to the border between two cathode rings and between the smallest cathode, C1, ring and the anode. Thus for avoid discharge due to the high voltage used there are two possibilities: or decrease the voltage difference or increase the separation between the electrodes (once the gas pressure has been fixed).

Figures 5.14 and 5.15 show the Paschen curve for the C_3H_8 and the arrows indicate the sparking voltage corresponding to the distance between two consecutive cathode rings (of 0.4 mm) and between the anode and the first cathode ring C1 (of 3 mm). The curves have been obtained from the Paschen law:

$$V = \frac{B_0 P d}{\ln(P d) + \ln\left(\frac{A_0}{\ln(1+\gamma^{-1})}\right)} \qquad 5.5$$

where A_0, B_0 and γ are constants depending by the gas used, d is the distance between two electrodes, P the gas pressure and V the sparking voltage. The Paschen characteristics for Propane gas has been derived from the publication of Heylen [Heylen, 2000]. The 0.4 mm gap distance at 1 μm and 2 μm is respectively of about 400 V and 500 V. This value can be compared with the difference of voltages between the cathodes rings biased accordingly to figure 5.5. Even for high voltage, as 750 V or 850 V, the maximum voltage difference between two cathode rings is well below the sparking voltage both at 8.09 torr and 16.18 torr, the voltage difference between C1 and C2 (the higher between

two consecutive rings) being of 127.5 at 750 V and of 144.5 V at 850 V. The sparking voltage values for the 3 mm distance between C1 and anode are about 700 V and 1000 V respectively at 1 μm and 2 μm site size, enough above the difference at 750 V and 850 V, being respectively of 502.5 V and 569.5 V. This entails that, accordingly to figure 5.9 and 5.13, it would be possible work at high gas gain without run into discharge effects. Anyway, as we shall see in the next paragraph, high gas gain entails also have an electronic able to manage wide range of signals and the optimum solutions is also strongly dependent by the kind of radiation spectra expected to detect.

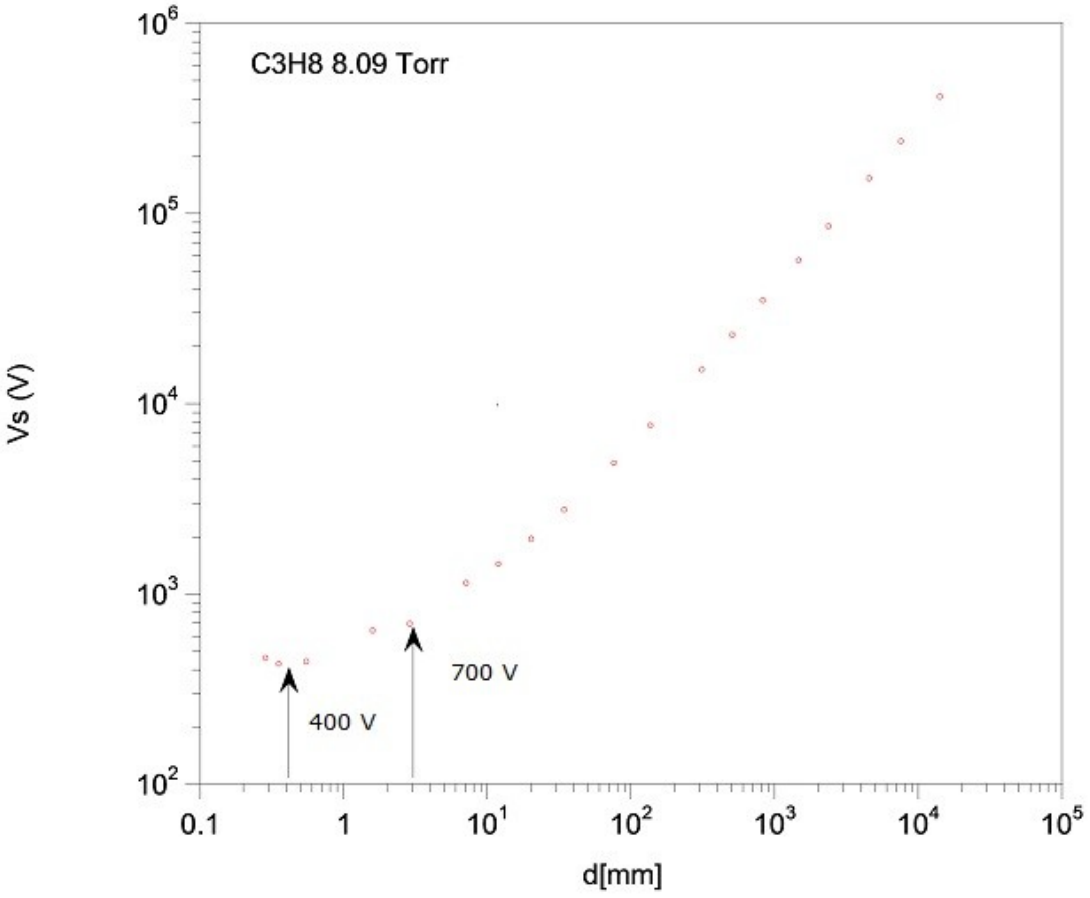

Figure 5.14 - Representation of the Paschen law for the C_3H_8 gas at 8.09 torr (1 μm site size). Are showed the points of maximum potential attainable between two consecutive cathodes and between C1 and the anode.

The choice of simulate 1 μm or 2 μm site size without incur into discharge problems permits thus to evaluate experimentally which is the best solution in relation with space radiation and detector characteristics in order to obtain significant lineal energy spectra.

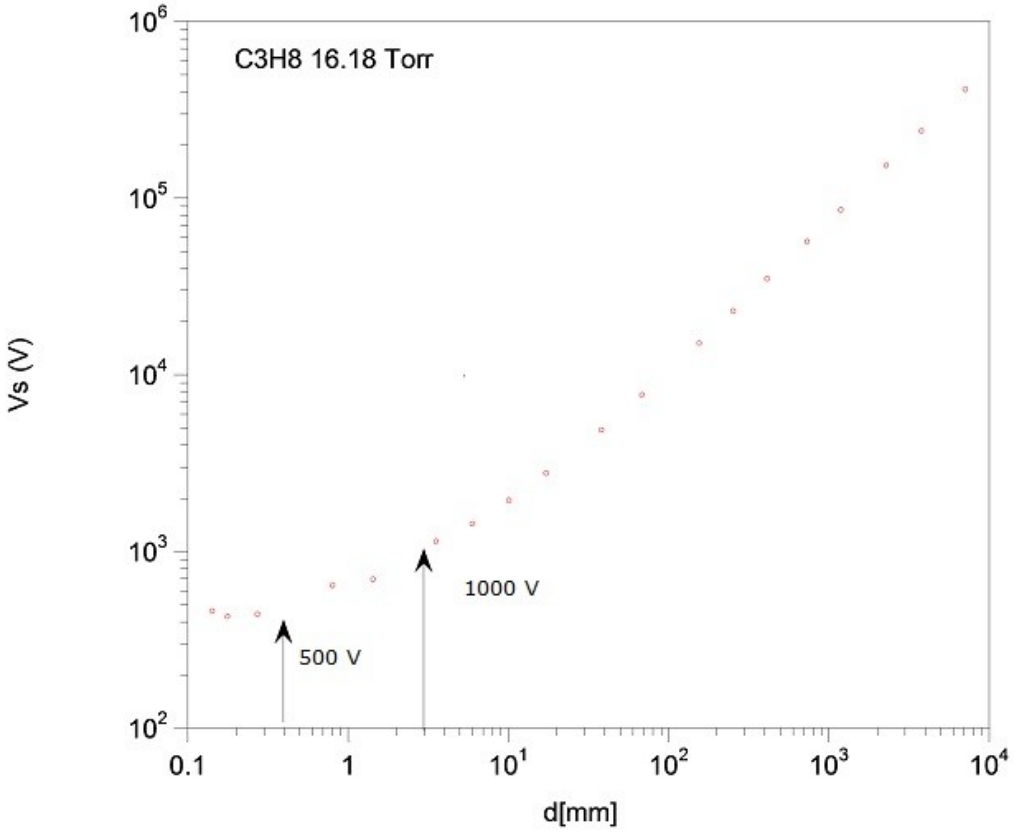

Figure 5.15 - Representation of the Paschen law for the C_3H_8 gas at 16.18 torr (2 μm site size). Are showed the points of maximum potential attainable between two consecutive cathodes and between C1 and anode.

5.4 - Electronic design

5.4.1 - Preamplifier and voltage divider

The detector has two electronic boards: one contains a preamplifier and the other one a voltage divider. The preamplifier receives the output from the anode and it provides a positive signal. The voltage divider is used to set the specific voltage of each cathode ring and anode through apposite coaxial cables and connectors. The electronic boards have been chosen to place outside the low gas pressure chamber. In this way the electronic boards work in higher pressure and it is easier to prevent discharges. Moreover in this way the electronic components do not pollute the gas inside the TEPC. The electronic components indeed are subjected to release impurities and pollutants when placed in vacuum and they could change the composition of the gas, altering the gain of the detector.

5.4.2 - Electronic noise and counting rate

Radiation in the space is a mixed field with energies ranging from few eV up to thousand of MeV. The deposition of energy in the gas chamber therefore has a similar spreading behaviour and the electronic has to be able to manage an energy range as much as possible wide. The requirement in lineal energy range that the detector has to satisfy spans about from 0.2 to 2000 keV/μm. The upper value energy deposition is due to the recoil of secondary Oxygen ions originated by the interaction of the primary protons with the detector cathode walls. Ions with charge bigger than Oxygen which deposit bigger energy per micrometer are also produced, but these events are very rare and therefore is possible neglect energy deposition events bigger than 2000 keV/μm. The lower level of energy deposition detectable by the device is bound by the electronic characteristics, that is by the minimum signal that can be separated from the background noise. The range between the upper and lower level that can be managed by electronic is called *dynamic range*. This range is fixed by the maximum and minimum number of electrons produced and amplified in the detector gas chamber and gathered by the anode. Since for create a single ionization, i.e. a electron-ion couple, are needed about 30 eV of energy deposition, the number of electrons generated by the upper limit of lineal energy deposition, 2000 keV/μm for 1 μm site size, is

around $2 \cdot 10^6$ eV / 30 eV = $6.7 \cdot 10^4$. As it has been showed in paragraph 5.3.5 the possible set of cathode voltage available for 1 μm site size range from 600 V up to 750 V. Taking for the cathode a value of 700 V this means, according to figure 5.11, a gas gain of about 1600. Therefore the maximum number of electrons that the electronic has to manage is the number of electrons generated by the upper limit of lineal energy deposition multiplied by the gas gain, that leads to a maximum signal of about 10^8 electrons. The lower level of detector sensibility is imposed by the electronic noise generated by the preamplifier of the detector. This threshold depends by the total capacity used in the device and by other electric noises that create a certain variance in the signal. In laboratory it has been measured this noise of the electronic with the electronic chain described in the paragraph 4.3. In order to measure the noise of the pre-amplifier it is necessary separate the noise of the electronic chain by that of the pre-amplifier itself. Therefore by means of a pulse generator has been generated a signal for the pre-amplifier and the output acquired with the acquisition software *Kmax*. What has been recorded is the output signal for the electronic chain with the pre-amplifier and without, for a voltage input of about 6.40 mV. Table 5.2 reports the centroid and the FWHM for the two signal.

	Centroid	**FWHM**	**Voltage Input V_i (mV)**
Pre-amplifier ON	283	7	6.6
Pre-amplifier OFF	253	2	6.4

Table 5.2 – Output signals in channels for the electronic chain with pre-amplifier and without it. The centroid channel and the FWHM in channels for the two signals are showed.

To convert the noise from channels to electrons, it is necessary have the electric charge for channel. Therefore it has been obtained the total charge in input, considering that the total capacitance of the pre-amplifier is about C = 1pF (parameter of construction). Therefore the total charge is $Q = C \cdot V_i$. The charge for channel thus is, respectively for the two signals, the total charge over the channel of the centroid:

$$P.a.\ ON\ \rightarrow\ \frac{Q}{Channel\,Centroid} = \frac{6.6\ fC}{283} = 0.02332\ \ C\ /\ ch \qquad 5.6$$

$$P.a.\ OFF\ \rightarrow\ \frac{Q}{Channel\,Centroid} = \frac{6.4\ fC}{253} = 0.02529\ \ C\ /\ ch \qquad 5.7$$

If we divide this for the charge of a single electron what results is the number of electrons per channel:

$$P.a.\ ON\ \rightarrow\ \frac{0.02332\,C/ch}{1.602\cdot 10^{-19}C} = 145\ \ electrons\ /\ ch \qquad 5.8$$

$$P.a.\ OFF\ \rightarrow\ \frac{0.02529\,C/ch}{1.602\cdot 10^{-19}C} = 158\ \ electrons\ /\ ch \qquad 5.9$$

Therefore the noise of the electronic chain with pre-amplifier and that of the only electronic chain is calculated multiplying by the FWHM in channels for the two signals:

$$P.a.\ ON\ \rightarrow\ 145\ \ electrons\ /\ ch\ \cdot\ 7\ ch = 1015\ \ electrons \qquad 5.10$$

$$P.a.\ OFF\ \rightarrow\ 153\ \ electrons\ /\ ch\ \cdot\ 2\ ch = 306\ \ electrons \qquad 5.11$$

Therefore subtracting the two noises, one obtains:

$$1015 - 306\ electorns = 709\ \ electrons \qquad 5.12$$

This means that with a minimum S/N (signal to noise ratio) fixed to three, the minimum signal detectable by the instrument should be around $2\cdot 10^3$ electrons. What comes out is that the electronic can manage a range of electrons that span 6 decades, from about 10^3 up to 10^8 (that is the dynamic range of the electronic). The minimum signal manageable by the electronic is in agreement with the assumed lineal energy lower limit of the detector, that is around 0.2 keV, since the minimum number of electrons for such limit is $1600\cdot(0.2\ keV\ /\ 30\ eV\ ) \cong\cong 10^4$.

With a minimum electronic threshold of 10^3 electrons the lower limit of lineal energy deposition that TEPC would be able to detect is of about (10^3·30 eV) / 1600 = 0.02 keV/µm.

Another parameter that we take into account is the electronic velocity, that is how many events the electronic can manage in a second. It has already been pointed out that aboard ISS the average counting rate of protons that will interact with the detector is of about 73 protons per second [Technical Meeting on TEPC Electronics, 14 January 2011, EuCPAD-3200-Minutes-DLR-001]. As it has seen in the paragraph 5.3.2 this value increases of almost 100 times when the ISS passes inside the South Atlantic Anomaly, giving a maximum number of events of 7300 protons per second, i.e. an expected counting rate as high as about 7kHz [Technical Meeting on TEPC Electronics, 14 January 2011, EuCPAD-3200-Minutes-DLR-001]. Therefore the preamplifier has to be able to manage at least that frequency, in order to be not blinded by two events occurring too close (the *pile-up* effect). In In this work high values of counting rate, for instance during SPEs, have not been taken into account, and in such cases the TEPC could not manage good measurements with such high counting rate.

CHAPTER VI

Detector construction and assembly

6.1 - Introduction

This chapter deals with the first phase of the construction of the EuTEPC. The main characteristics of the detector discussed in the previous chapter have imposed the constraints for the subsequently working out of the technical design. The mechanical design has been the main task to challenge, especially due to construction problems caused by the geometry of the mechanical parts and the material used. The construction of the components has been carried out at CINEL workshop (Padova) while the assembling phase and the preliminary tests on the detector system have been performed at the LNL-INFN (Legnaro). Paragraph 6.2 presents an overview of the mechanical characteristics and designs of the TEPC, in order to understand how the detector is composed and built. Then the central core of the detector which consists in the gas spherical chamber is discussed, explaining more in detail the process of creation and assembly. Finally the detector's Vacuum System which hosts the gas chamber. The research of a vacuum sealing method sufficient to endure for 2-3 years of use in the space has been one of the most challenging task tackled. The test of the sealing and the methods used are presented along with the measurements of the degassing inside the detector and the first discharge tests.

6.2 – TEPC mechanical design overview

The EuTEPC has been designed in order to satisfy space standards, i.e. for instance material used, vibrations constraints and lack of spare parts aboard space station. Vibrations have been the central concern in the mechanical design and assembling procedures since the waves inside space stations don't propagate outside in the void space but remain trapped inside the structure. Especially the

cathode sphere, given its fragile structure, needed special blockages in order to hold out against continuous vibrations and possible shocks.

The spherical TEPC consists of four subsystems which are sketched in figure 6.1:

- **Shield System**
- **Vacuum System**
- **Detector System**
- **Electronic Boards System**

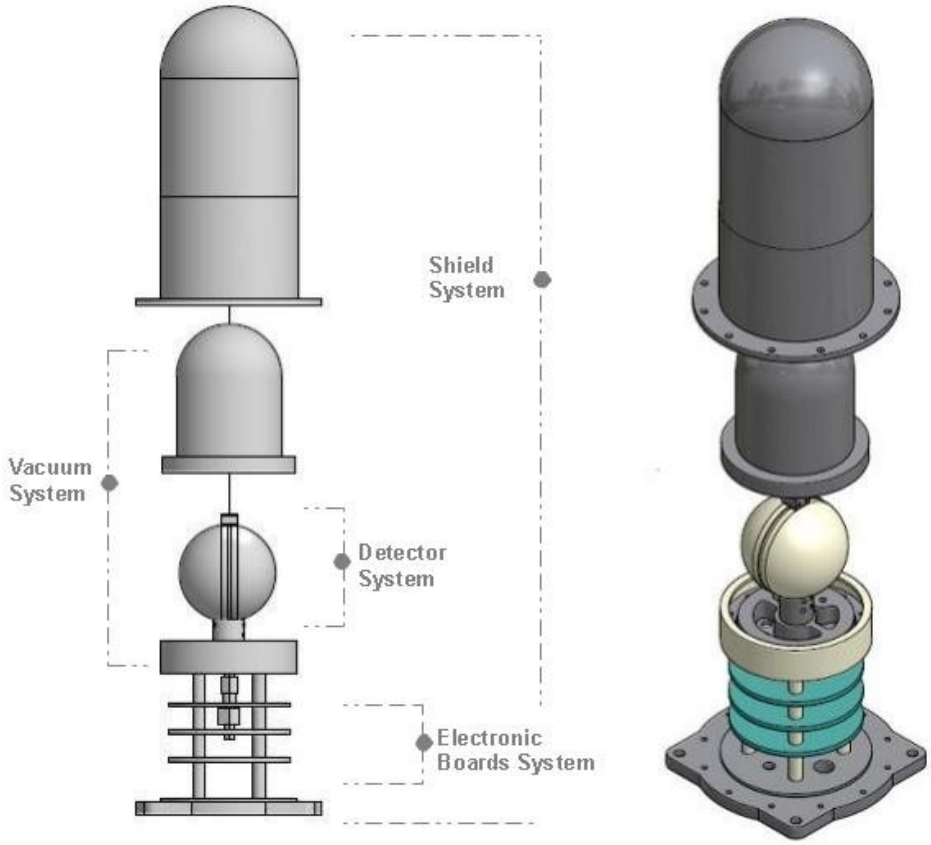

Figure 6.1 – Exploded view of the whole detector and its subsystems: Shield System, Vacuum System, Detector System and Electronic Boards System

The Detector System consists of the A-150 plastic cathode rings divided by the Rexolite insulating rings (see paragraph 5.3.4), and of the Rexolite insulating shells which enclose all the parts (Rexolite is a thermoset, rigid and translucent plastic produced by cross linking polystyrene with divinylbenzene). The cathode rings form the gas chamber which forms the sensitive part of the detector in which ionization events occur. The Vacuum System consists of the vacuum housing (made of stainless steel) which cover the Detector System and the mounting plate. The gas inside the Vacuum System is kept at the correct pressure according to the simulated tissue site size and it is completely sealed from the outside. Figure 6.2 shows the exploded view of the Detector and Vacuum System mounted together, while figure 6.3 shows the prototype of the Vacuum System with the Detector System mounted on the mounting plate. The mounting plate hosts also all the vacuum-tight micromin feed through connectors for the anode signal and the high voltage supply for the cathodes.

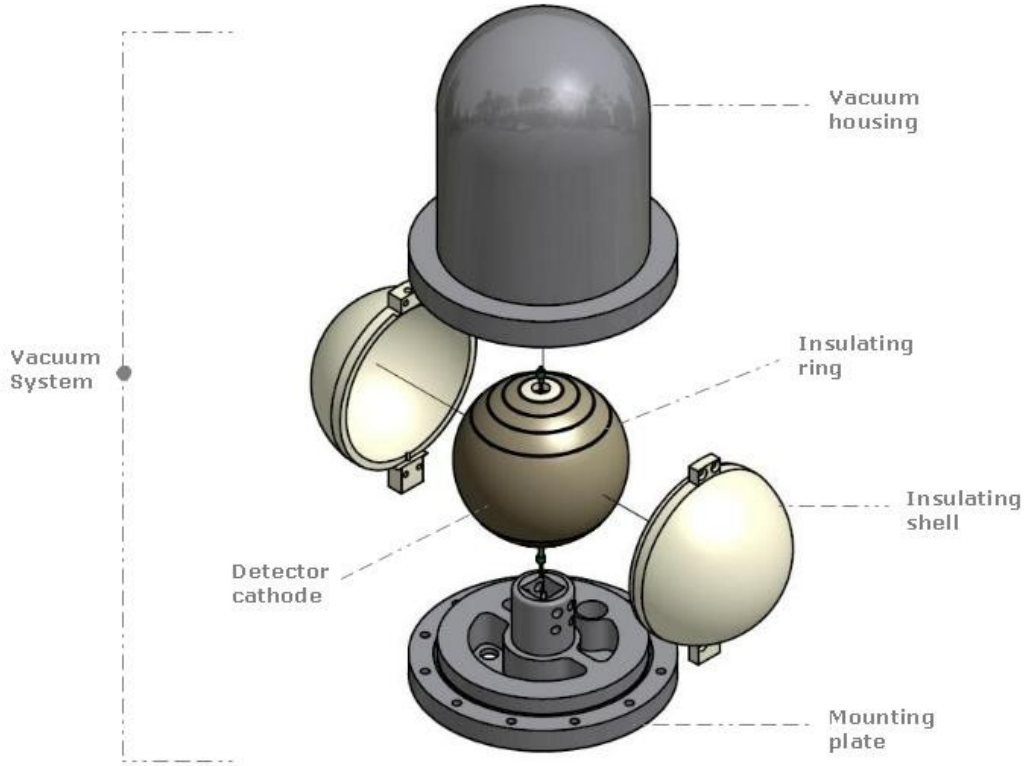

Figure 6.2 - Representation of the Detector System with the inner sphere, the enclosing Rexolite shells, the stainless steel cup and the bottom basement.

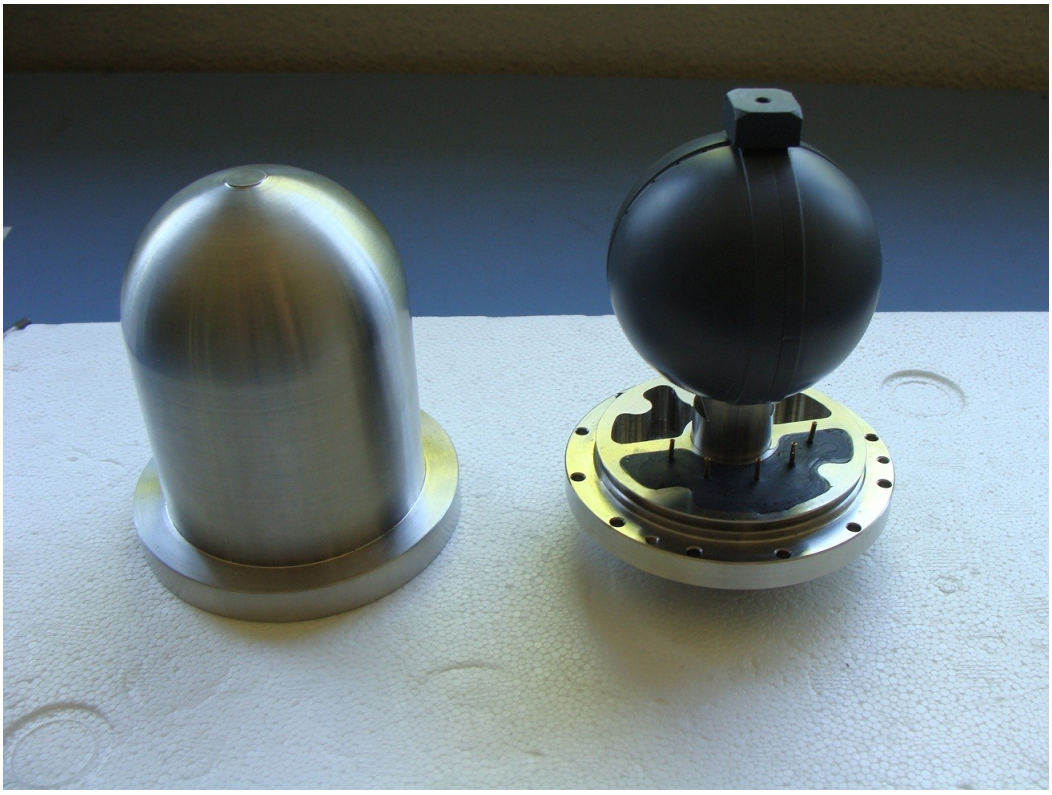

Figure 6.3 - Prototype of the Vacuum System with the Detector System mounted on the mounting plate

The Electronic Boards System consists of a Preamplifier and high-voltage divider boards made of Polychlorinated Biphenyls (PCBs), installed on four stainless steel columns fixed on the flange of the Shield System. The columns fix also the mounting plate of the Vacuum System to the flange by screws so as to block it. The shield housing is made of anticorodal aluminium of 3 mm of thickness, it covers the whole instrument (the item is about 20 cm high) and is screwed on the flange. In figure 6.4 the prototype of the shield housing with the Vacuum System mounted on the four stainless-steel columns is showed.

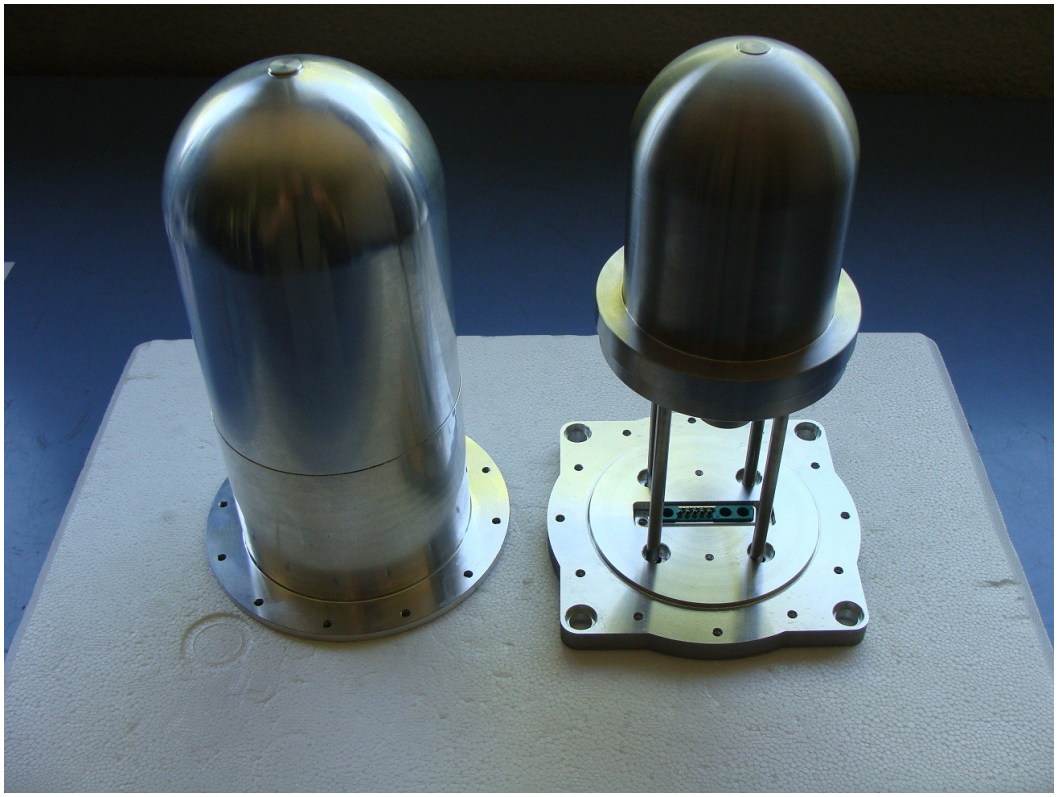

Figure 6.4 - Prototype of the shield housing with the Vacuum System mounted on the four stainless-steel columns.

6.3 - Construction of the spherical chamber

The sphere has been divided in nine rings of 3 mm thickness and with an inner radius of 25 mm. Figure 6.5 shows a section of the Detector System with the cathode rings, the insulating shell and the anode wire. To insulate each ring and give it a specific potential, eight rings of Rexolite of 0.5 mm thickness have been also turned and inserted between the rings of A-150 plastic. The use of Rexolite as insulator is due to its characteristic to have both insulating and tissue-equivalent properties and also to its ability to withstand high voltage. Besides it has high resistance to mechanical deterioration by ionizing radiation. The value of the thickness for the Rexolite rings has been chosen according to the sparking voltage simulations of paragraph 5.3.6. Two external hemisphere shells of Rexolite insulate the cathode from the exterior. The two shells of Rexolite other

than to avoid discharges between the cathode and the external aluminum cup are needed also in order to enclose and block all the rings. Four screws at the extremities of the shells close tightly all the system.

The turning of the A-150 plastic cathode rings is a delicate task, since it is essential to remove all the flaws from the internal surface of the rings. Particular care in the turning has to be taken in the spots where the two rings approach, because it is there that discharges are more likely to occur (little bumps can produce local increase of the electric field and thus generate a discharge with the adjacent ring). Each ring and the insulating shells have been turned by a mechanical lathe with electronic control and assembled after in laboratory (figure 6.6).

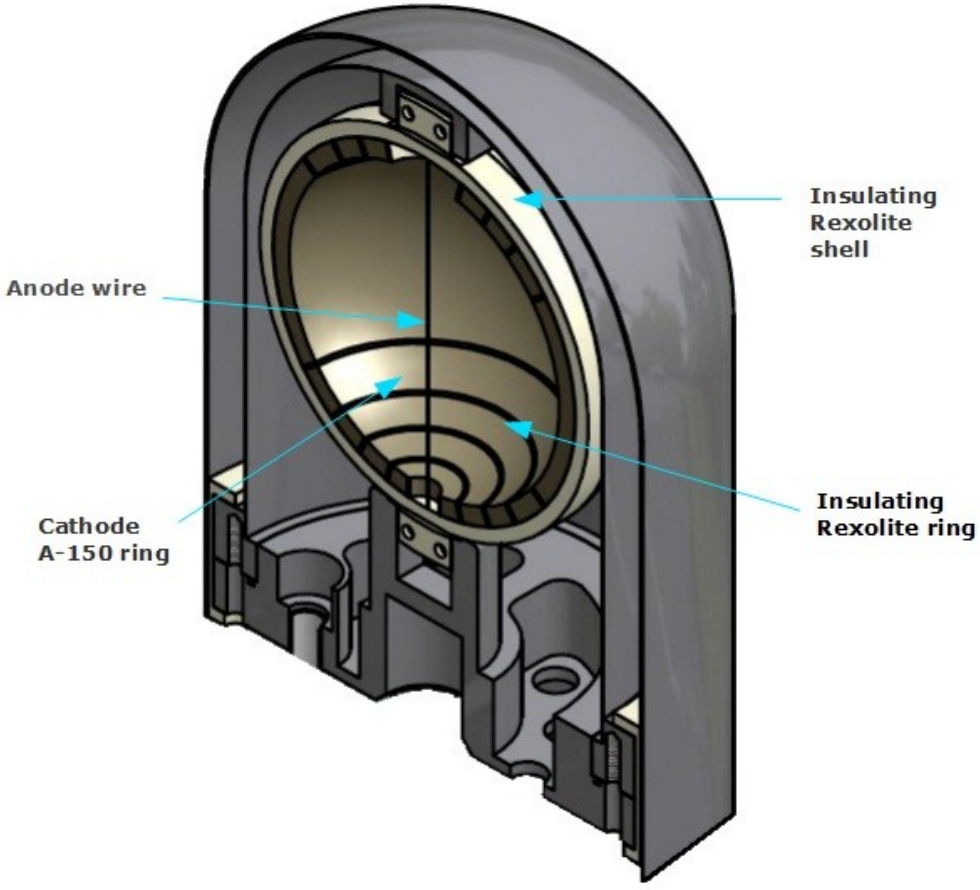

Fgiure 6.5 - Section of the Detector System with the A-150 cathode rings, the anode, the Rexolite rings and the closing shells of Rexolite.

The anode wire consists of a 100 μm gold plated tungsten wire fixed at the extremities of the Rexolite shells through a crimping pins. The rings of A-150 are fed with a specific voltage (paragraph 5.3.4) by a 140 μm copper wire coated with Kapton. Each wire is soldered to a gold plated copper crimp connector which has been inserted inside the A-150 plastic rings. The Cu crimp connectors serve also to block the rings inside the Rexolite shells in such a way that they cannot rotate around their axis. The insertion of the connectors in the A-150 plastic rings occurs by heating the connector with a tin welder and pressing the connector inside the plastic ring. After that, the crimp connectors are soldered with the 140 μm copper wires. The wires are hosted inside cavities carved in the external surface of the Rexolite shells. Subsequently all the connectors and wires are fixed and insulated with a special Rexolite® Adhesive glow (12517, C-LEC Plastics Inc).

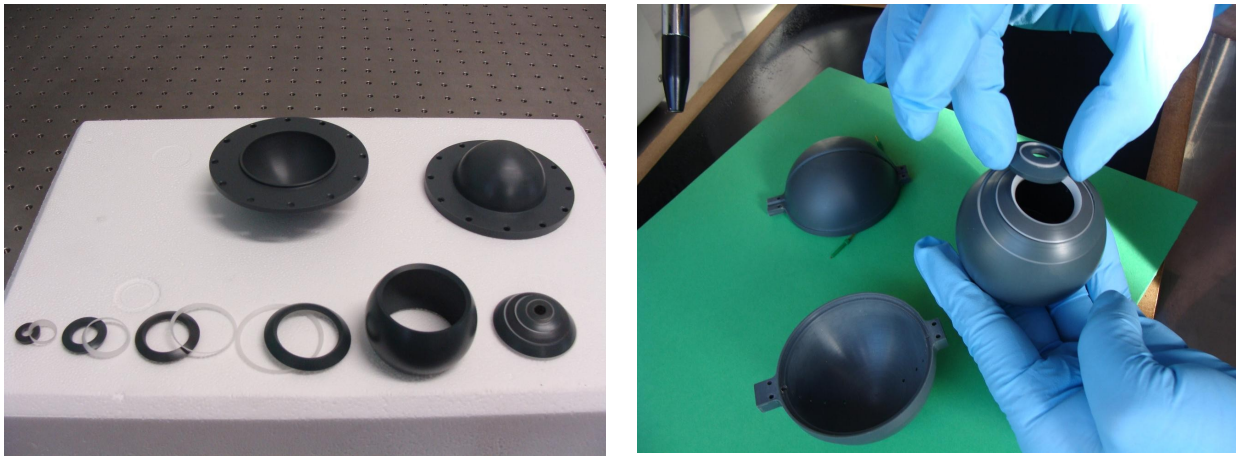

Figure 6.6 – The cathode rings with the insulating rings and shells (left) and their assembling (right)

6.4 - Vacuum System

The bottom plate hosts the holes for six Micromin connectors (ATI-Elctronique Company) that provide the voltage to the cathode and the hole for the inlet of the gas inside the sphere. The Rexolite shells that enclose the A-150 cathode are fixed to the stainless cup and basement at two extremities along the anode axis.

The mechanical blockage (see figure 6.5) is needed to secure the chamber from vibrations and damage of the components. The vacuum housing and the basement are fixed tightly together by twelve screws along the external circumference.

6.4.1 - Vacuum sealing procedures and results

In order to reach a sealing able to maintain the gas pressure constant for a long period (approximately three years) different procedures for creating the vacuum inside the detector, filling it with the gas and finally sealing the instrument have been studied. The first procedure that has been investigated consists in use a copper tube, inserted in a Swagelock connector, which is crimped with an apposite pincer once the gas has been poured inside. The procedure has been to utilize a special screw provided with a tempered stainless-steel sphere that close tight the hole in the detector basement for the inlet of the gas. Different pincers have been investigated. The second procedure consists of a special screw provided with a tempered stainless-steel sphere that close tight the hole in the detector basement for the inlet of the gas.

A Balzers Helium leak detector (HLT 150) has been used to test the leakage in the sealing. It consists of a Rotary pump to create the vacuum and a sensor for the Helium which allows to test the sealing. Once the device that has to be tested is plugged to the detector, is therefore possible to verify if molecules of Helium enter through the device pouring Helium close to the possible leak. The detector measures the variation of pressure of the Helium per unit of time per liter, that is *mbar·l/s*. The leakage test has been carried out both for the copper tube and the sealing screw method. The copper tube has been crimped using three different pincers of various dimensions and crimping techniques. The smaller pincer which crimps on a very small area and cut at the end the tube is showed in figure 6.7.

Figure 6.7 – Small pincer

Figure 6.8 shows the larger pincer which has a broad area of crimp, of about 8 mm, but doesn't cut the tube.

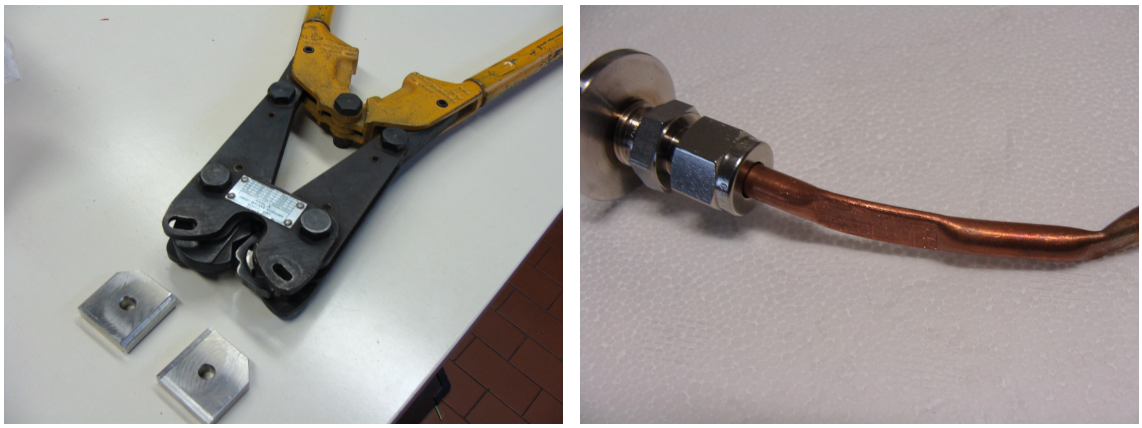

Figure 6.8 – Large pincer

Finally the last pincer is a special American tool used to obtain apposite vacuum sealing, which crimping technique consists in crimping the tube in a rather broad area (about 3-4 mm) and also cutting the tube. Figure 6.9 shows the tool and the result.

Figure 6.9 – American pincer

The other method used for sealing the detector consists in closing the hole for the inlet of the gas with a screw on the tip of which a tempered stainless steel sphere has been soldered. Once the vacuum has been created, the screw is screwed in with a special tool. Figure 6.10 shows the flange used for the test with the screw and a detail of the screw with the sphere.

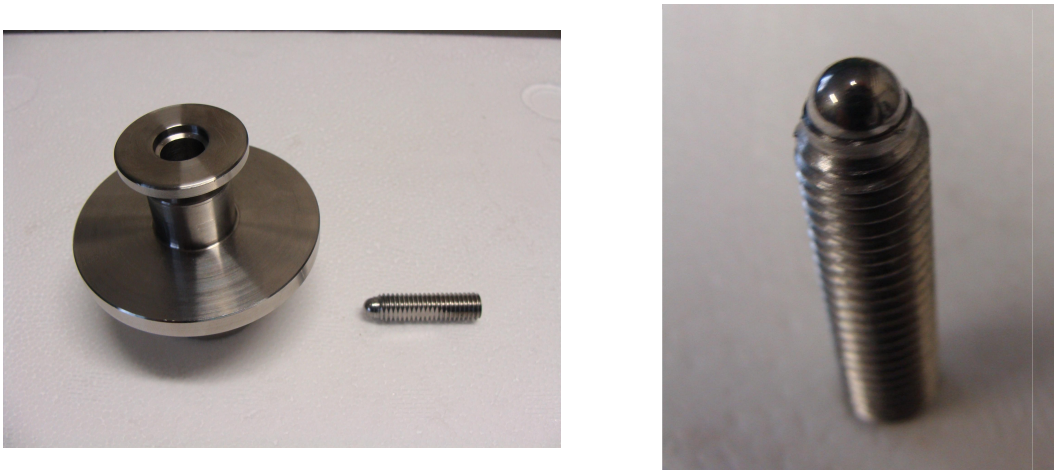

Figure 6.10 – The screw with tempered stainless steel sphere (right) and the mock up of the mounting plate used for the test (left)

The copper tubes crimped and the flange with the screw have been mounted on the Helium leak detector, tightening with an O-ring in order to perform a safe

sealing of all the system. The Balzers HLT 150 Helium leak detector has a sensitivity to $1 \cdot 10^{-10}$ mbar·l/s. Measurement of the Helium background has been performed before each leakage measurement, keeping the environment well ventilated in order to minimize bias in the background level of Helium due to several cycles of measurements. For each method of sealing ten measurements have been performed. Table 6.1 summarizes the obtained results.

American Pincer (mbar·l/s)		**Small Pincer (mbar·l/s)**		**Screw (mbar·l/s)**	
Background	Leakage	Background	Leakage	Background	Leakage
$3.81 \pm 0.37 \cdot 10^{-9}$	$4.07 \pm 0.33 \cdot 10^{-9}$	$4.61 \pm 0.15 \cdot 10^{-8}$	$1.35 \pm 0.07 \cdot 10^{-3}$	$3.40 \pm 0.25 \cdot 10^{-9}$	$3.57 \pm 0.24 \cdot 10^{-9}$
Difference		Difference		Difference	
$0.26 \pm 0.07 \cdot 10^{-9}$		$1.35 \pm 0.07 \cdot 10^{-3}$		$0.17 \pm 0.07 \cdot 10^{-9}$	

Table 6.1

The results for the large pincer are not showed since it has been not possible to reach a vacuum beneath some millibar. Table 6.2 finally presents the leakage of Helium per hour (the volume of the cavity used for the vacuum test was of about 0.015 liter).

American Pincer (mbar/h)	**Small Pincer (mbar/h)**	**Screw (mbar/h)**
$6.24 \cdot 10^{-5}$	324	$4.08 \cdot 10^{-5}$

Table 6.2

The large pincer cannot create a sufficient crimping for a worthwhile sealing. This happens because the elasticity of the copper tube once that the pincer is opened doesn't allow the copper tube internal surface to solder, and the repulsive forces prevail forming a leak. The two other pincers instead, besides pressing the tube at the end of the crimping, cut the metal. This method permit the copper to be well merged together at least close to the extremities where the cut has occurred. The American pincer however, since perform the pressing in a broader area, performs a better work, and the final result is comparable to that of the screw. These two methods have the same effectiveness indeed and both have a

increment of the pressure of about 4-6·10^{-5} mbar/h. The screw method finally has been chosen since it doesn't need any tube (that would cause complications with the insertion of the electronic boards too). The standard limit for a vacuum-tight sealing is of the order of $1 \cdot 10^{-7}$ mbar·l/s, which means about $4 \cdot 10^{-4}$ mbar·l/h. For the 0.015 liter cavity used in the experiment therefore the maximum rise of the pressure has to be of $2.6 \cdot 10^{-2}$ mbar/h, that is well above the increase of pressure obtained experimentally for the screw and the American pincer. With a leakage of about $5 \cdot 10^{-5}$ mbar/h in one year the leakage will be of about 0.43 mbar/y. This result is therefore acceptable for a sealed detector that has to work at the same pressure for 2-3 years.

6.4.2 - Degassing process and gas inlet

Contamination of the gas inside the TEPC can come from leakage inside the structure of the detector or outgassing from detector's components, and therefore is fundamental to eliminate this kind of pollution in order to prepare the counter suitable to perform measurements. The outgassing effect is produced by every surface of the detector components that absorbs gaseous elements, like oxygen. If this contamination occurs, the absorbed particles are then emitted inside the counter chamber. Outgassing effect can introduce electronegative gases inside the cavity, causing electron capture and preventing correct gas amplification. In order to avoid this, it is essential to clean and eject all the impurities from the detector's components. Therefore the whole detector chamber must be kept in vacuum for several days so as to eliminate every polluting gas absorbed by the surfaces of the detector components. In order to test the outgassing of the various Vacuum System's components (see figure 6.2) measurements of the degassing have been performed in two different steps:

a) test of the Vacuum System

b) test of the Vacuum System outgassing with the feed through

Finally a last step of outgassing test is that of the Vacuum System with the detector plastic sphere (not covered in this thesis).

The mounting plate of the Vacuum System hosts the hole for the vacuum and the gas inlet according to the result of paragraph 6.4.1, where a screw is used to close the Vacuum System. Figure 6.11 shows the side view of the mounting plate of figure 6.2 with the screw and the joint for the vacuum system device used for creating the vacuum inside the detector.

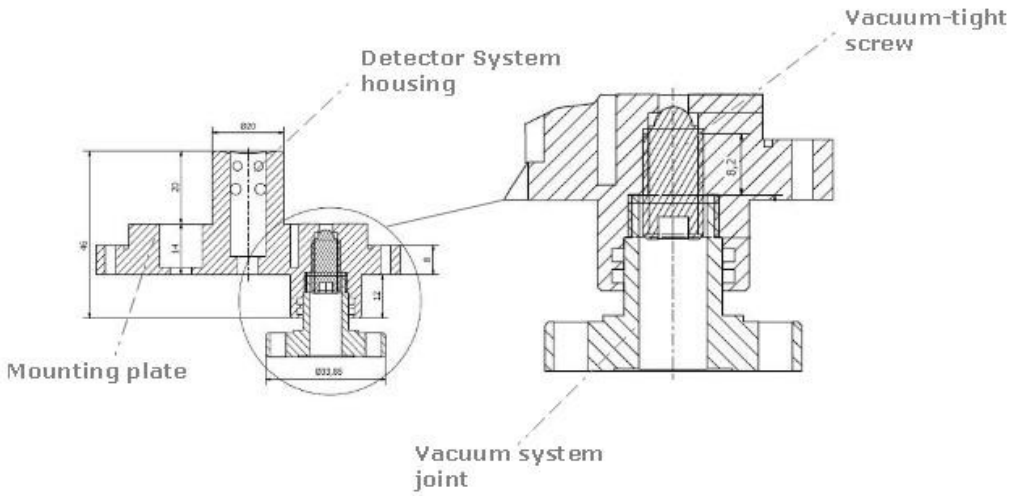

Figure 6.11 – Mounting plate side view with the detail of the screw with tempered stainless steel sphere and the vacuum system joint.

Before to perform the step test previously pointed out the rate of degassing of the joint system used for connect the detector has been tested. The vacuum has been performed with the vacuum pump system sketched in figure 6.12, which shows the pump system, the joint system and the Vacuum System. Figure 6.13 shows the joint system and the manometers used.

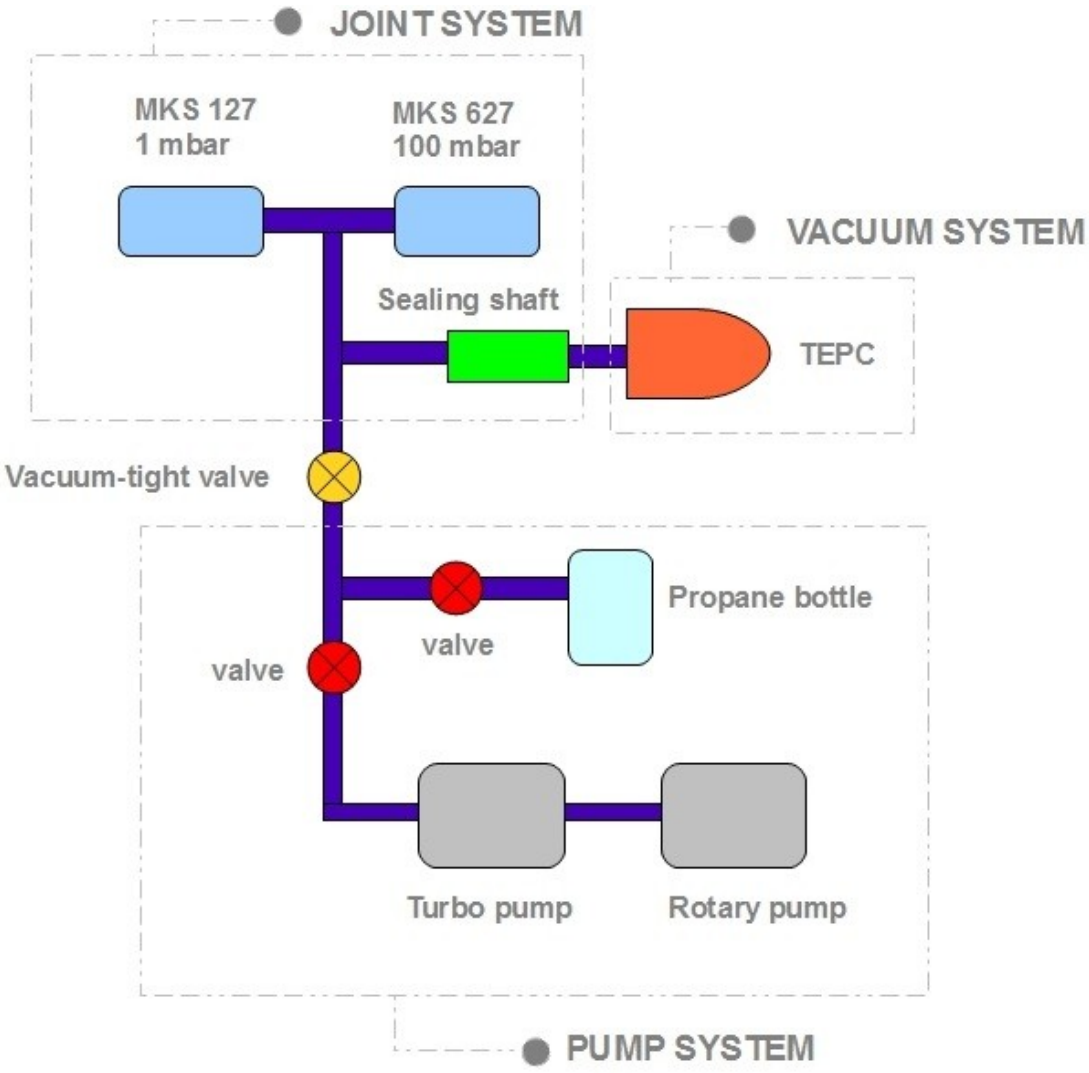

Figure 6.12 – Sketch of the Vacuum System together with the joint and pump system

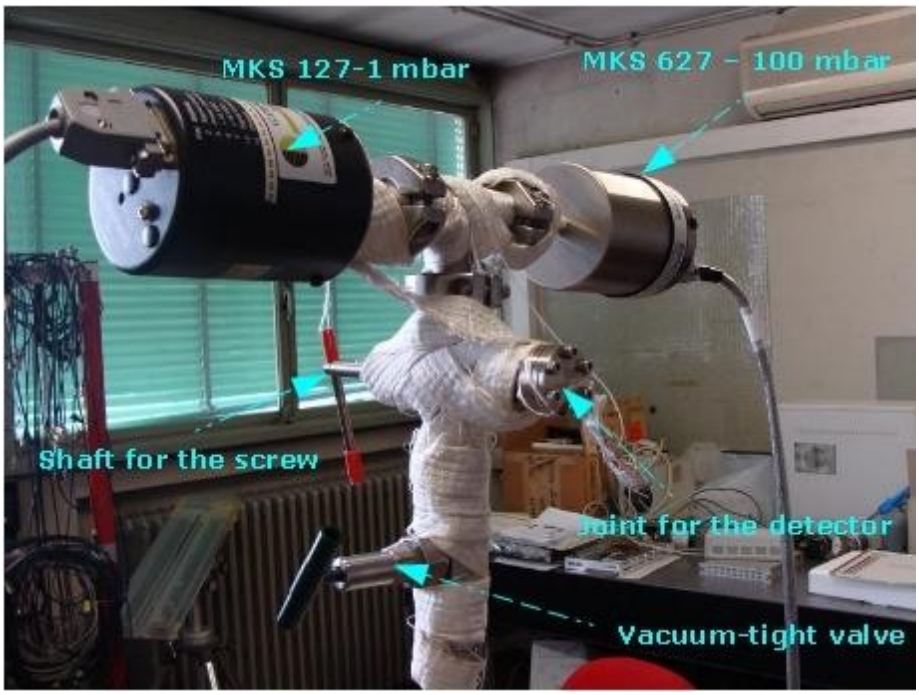

Figure 6.13 – Joint system used for the Vacuum System test with the connection for the Vacuum System. It is also showed the special shaft used for screw up the screw with the stainless steel tempered sphere.

The pumping system described in paragraph 4.2 has been updated with two manometers: the MKS 127 Baratron (with full scale range of 1 mbar) for measuring the pressure in the vacuum phase and the MKS 627 Baratron (with full scale range of 100 mbar) for measuring the pressure in the gas filling-up phase. The first manometer has a higher sensitivity and for this reason has been used for measuring the degassing rate. To speed up the degassing of the steel pipes the joint system has been heated with a special thermic strip at a temperature of about 70 °C (visible in figure 6.13). The rate of degassing has been thus measured and reported in figure 6.14.

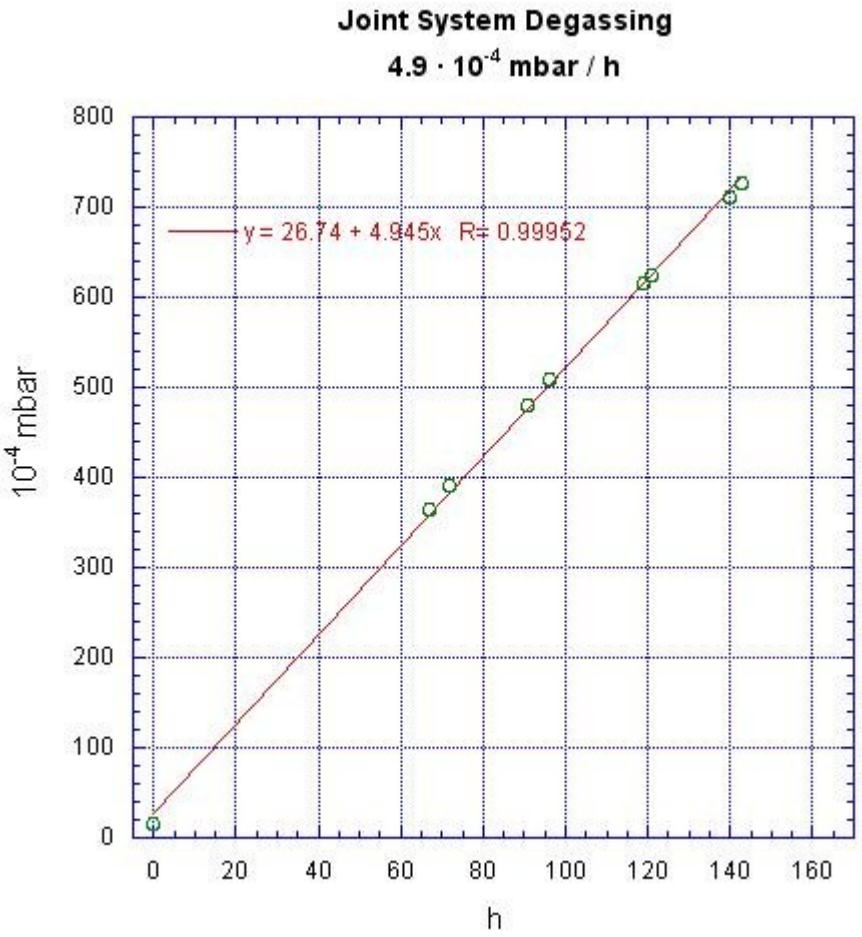

Figure 6.14 – Degassing rate of the joint system. Measurements has been made with the MKS 127 Pressure measurement

The degassing rate of the joint system is of about $4.9 \cdot 10^{-4}$ mbar/h. This is the background of degassing inherent to the system of measurement. In the measurement of the outgassing of the detector's sphere inside the Vacuum System the background must be subtracted in order to obtain the degassing of the detector alone.

a) Test of the Vacuum System

The sealing between the mounting plate and the vacuum housing has been tested with the Balzers Helium leak detector. An O-Ring (made of Viton®), seated in a groove of the mounting plate, is compressed by means of twelve screws creating a seal between mounting plate and vacuum housing. No leakage has been detected. Figure 6.15 shows the Vacuum system connected to the Balzers detector.

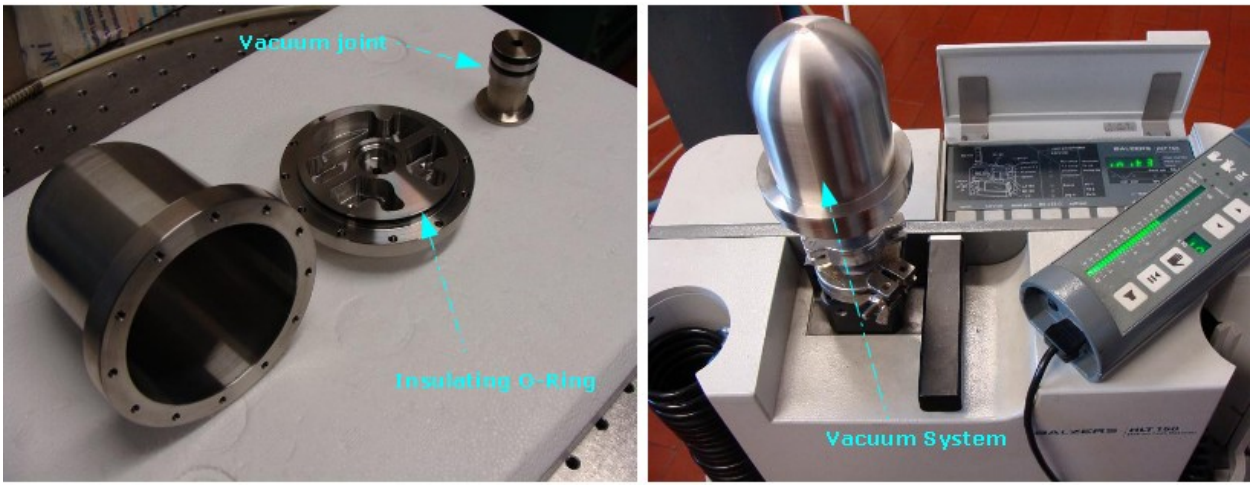

Figure 6.15 – The Vacuum System unmounted on the left and the Vacuum System connected to the Balzers detector on the right

b) Test of the outgassing of the Vacuum System with the feed through

The next step of the degassing measurements has been performed on the Vacuum System with the feed through mounted and soldered with tin (Castoline 157). The mounting plate (figure 6.2) host the hole for the six Micromin connectors. As showed in figure 6.16 the connectors have been positioned accurately on the mounting plate and subsequently soldered with the tin. The process of soldering has been performed heating the mounting plate (the temperature of soldering has been kept around 240-250 °C) with an electric plate and measuring the temperature with a thermometer (figure 6.17). Subsequently, a possible leakage around the connectors, due to an uncorrected soldering, has been tested with the Balzers Helium leak detector. No leakage bigger than about

4.4 10^{-9} mbar·l/s is present, which is anyway the Helium background average level observed during the test. After that, the insulation of the connectors and the maximum voltage applicable to them without provoking discharges (figure 6.18) have been subsequently tested. Each connector has been tested and the high voltage supplied to each connector has been raised slowly by means of a High Voltage supplier (Bertan Associates – Series 225). With a current limit of 0.15 μA, discharges have not been detected up to a feeding voltage of about 900 V. Since the detector will not work with voltage higher than 800 V, this test should assure that connectors will not cause discharge problems. But the same test must be achieved also in low pressure condition, in order to guarantee full reliability.

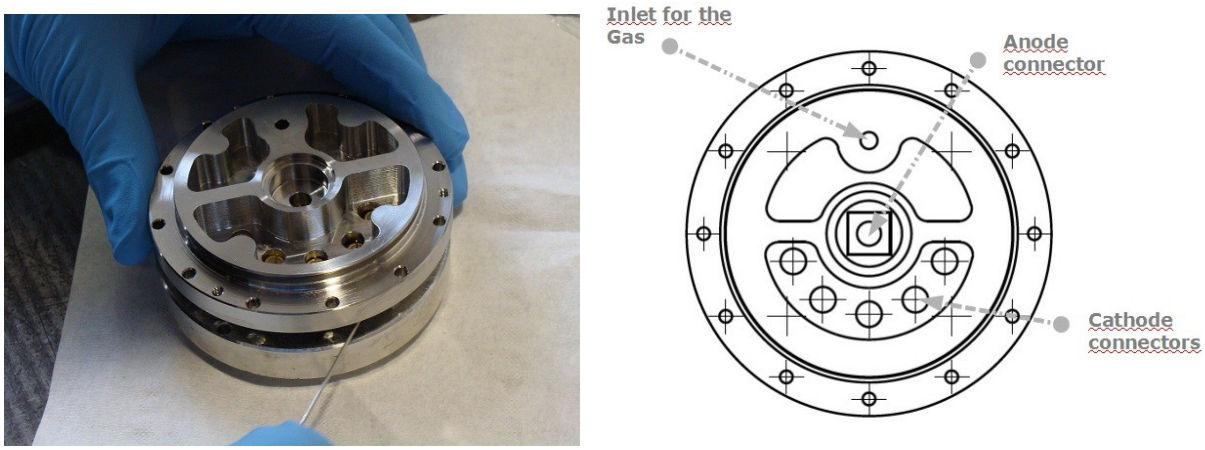

Figure 6.16 – The process of positioning of the connectors (left) and the sketch of the mounting plate top-view (right).

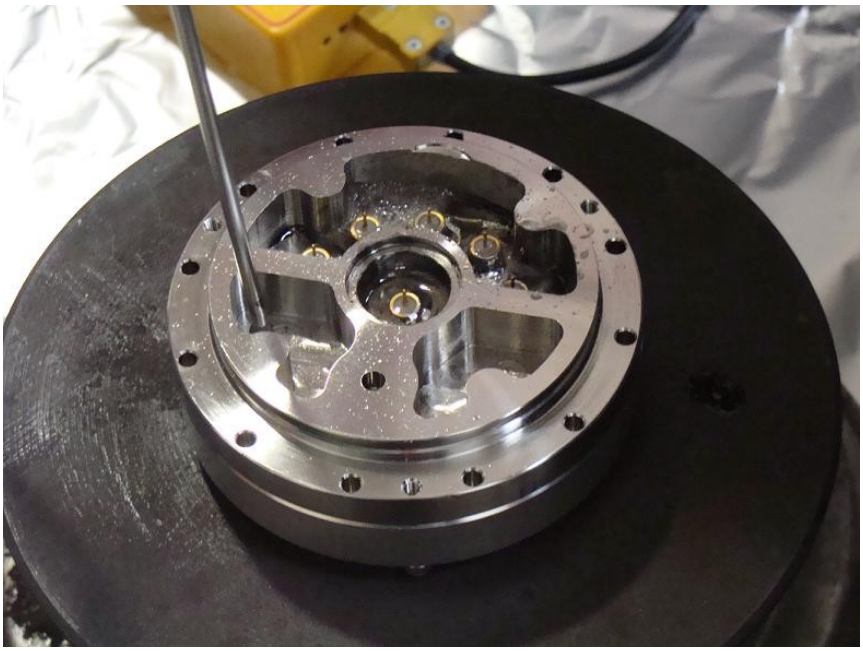

Figure 6.17 – The six connectors soldered on the mounting plate. In the figure the electric heating plate and the thermometer are also showed.

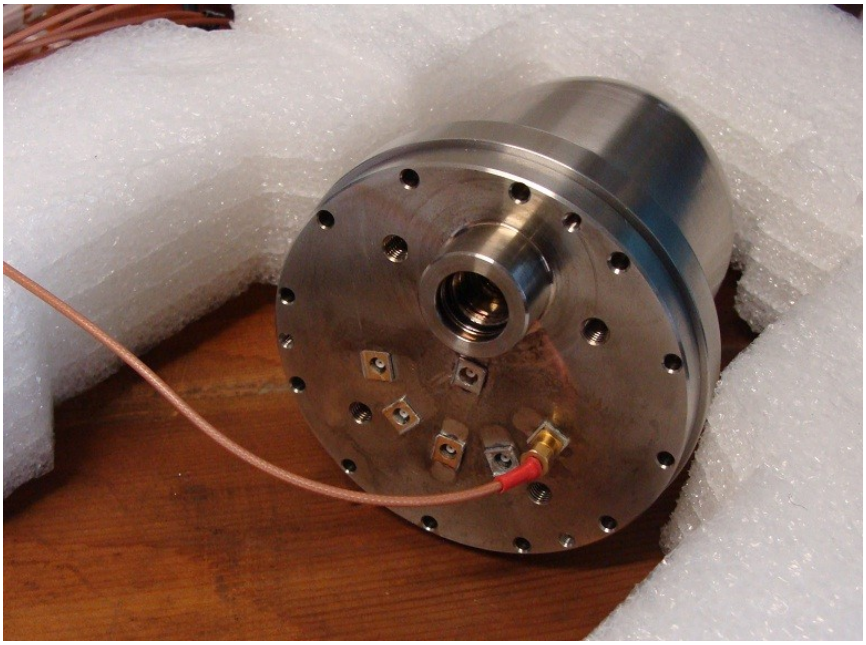

Figure 6.18 – Discharge testing of the Vacuum System's connectors with the High Voltage supplier.

Conclusions

The segmentation of the cathode sphere in rings with biased voltage has been fundamental to obtain uniform electric field along the anode. Simulations have showed the equivalence of the electric potential between the spherical counter and the cylindrical counter. This equivalence has been useful for the calculations of the gas gain using a model for cylindrical counters. These calculations have revealed that the best choice of the anode diameter is of 100 μm. Besides the sparking voltages for C_3H_8 gas, both simulating 1 μm or 2 μm, are always well above the voltage difference between the anode and the cathode C1 and between two consecutive cathodes, at least in the considered values of the cathode voltage simulated. This result entails the possibility to work with gas pressure both simulating 1 μm or 2 μm with different voltages. The choice of which gas gain adopt will be a future matter of discussion, according to the results of the first measurements once that the detector will be completed.

Outgassing effects and gas leakage are all drawbacks that must be minimized. It has been chosen to use C_3H_8 instead of C_3H_8-TE since it performs better gain at the same cathode voltage and in function of its lower gas deterioration. Test of the Vacuum System leakage and sealing methods have been performed in laboratory, together with discharge tests of the micromin connectors. A special vacuum sealing system has permitted to fix the upper limit of the Vacuum System leakage at about 0.35 mbar/y, and therefore it guarantees stability of the detector measurements for about 2-3 years.

The EuTEPC construction and assembling phase has not yet be completed. Construction of the Detector System is the most critic part, since cathode rings need accuracy in the turning and assembling. The first results of the assembling process of the detector sphere with mock-up rings and shells have showed also that in order to avoid vibration problems all the parts have to be tightly mounted and must fit accurately. Subsequently the cathode rings have to be fixed and connected to the micromins of the mounting plate in order to feed the cathodes with the high voltages. After that the final test of connections and cathode rings discharges will be performed for different gas pressures in order to verify what

are the better condition the detector will work with. Prototype of pre-amplifier and voltage divider will be constructed for laboratory test and subsequently electronic boards for space environment will be built with the same specifics of the previous one. After the final work of assembling finally the detector will be characterized with radiation sources and calibrated in energy in order to be ready for radiation measurements.

During the next work the better setting for the TEPC will be defined in order to fit with the ISS's radiation environment. But future implementation aboard spacecraft missions scheduled for interplanetary travel, where different radiation conditions compared with LEO are present, will be also possible.

Appendix I

Microdosimetric quantities

The concept of site size in term of energy deposition is of fundamental importance in the definition of what microdosimetry measures. The energy deposition in the matter is a function of the site size in which we perform the measurement. The deposition of energy occurs along the track of the particles that across this site. The quantity that defines an appropriate measure of the ionization density is called *Linear Energy Transfer*, or LET [ICRU, 1970]. More precisely the LET is defined as the quotient of the energy *dE* imparted to the matter by a charged particle of energy *E* and the path length *dx* that the particle traverses within the matter: *LET= dE/dx* [keV/μm] [1]. The measure of the LET is a mean value and doesn't take into account any stochastic property of the energy imparted. Moreover, it is not sufficient to determine the quality of the raditation. In microdosimetry the energy deposition, ε_i, is a stochastic quantity and is referred to a single interaction of a ionizing particle in a volume of matter of micrometric size. The single energy deposition ε_i can be written as:

$$\varepsilon_i = T_{in} - T_{out} + Q_{\Delta m}$$

where T_{in} is the kinetic energy of the ionising particle, T_{out} is the sum of kinetic energies of all the products of ionization and $Q_{\Delta m}$ is the change of the rest mass energy of all the particles involved. The sum of all the single energy depositions ε_i in a volume *V* of matter of mass *m* is the energy imparted ε:

$$\varepsilon = \sum_i \varepsilon_i$$

which is a stochastic quantity as well. The two new quantities that have been defined in microdosimetry by the International Commission Radiation Units and Measurements in 1983 [ICRU, 1983] are: the *specific energy z* and the *lineal*

1 LET can be defined as a total LET, L_∞, or as a restricted LET, L_Δ, where Δ is an energy cutoff, which means that are considered only particles with energy above.

energy y. The specific energy is defined as the ratio between the energy imparted and the mass of the volume considered:

$$z = \frac{\varepsilon}{m}$$

and is measured in Gray (Gy) [J/Kg]. If instead we take the imparted energy and divide it by the mean chord length *l* across the volume considered we obtain the lineal energy:

$$y = \frac{\varepsilon}{\bar{l}}$$

The mean chord length is the mean length of all randomly oriented chords in the volume considered[2]. The lineal energy is expressed keV/μm. We can relate the specific energy to the lineal energy through the relation:

$$y = \frac{z\,m}{\bar{l}}$$

Given that the lineal energy has a stochastic behaviour, one can obtain its distribution functions. The *distribution function F(y)* defines the probability of a single event having lineal energy equal to or less than *y*, whereas the *dose distribution* of lineal energy *D(y)* represents the fraction of absorbed dose with lineal energy equal or less than *y*. It is possible to derive with respect to *y* both the quantities obtaining the density distributions, which are respectively the *frequency probability density f(y)*:

$$f(y) = \frac{dF(y)}{dy}$$

and the *dose probability density d(y)*:

2 The Cauchy's theorem states that for a convex body $\bar{l}=4\cdot V/A$, where *V* is its volume and *A* its surface area. For a spherical body of diameter d the mean chord length is $\bar{l}=d\cdot 2/3$.

$$d(y) = \frac{dD(y)}{dy}$$

f(y) represents the probability of having an event occurring with lineal energy between *y* and *y+dy*, and *d(y)* represents the probability of deliver absorbed dose with lineal energy between *y* and *y+dy* by a single event.

The relation between the dose probability and the frequency probability is expressed as:

$$d(y) = \frac{y}{\bar{y}_F} f(y)$$

where y_F is the frequency-mean lineal energy:

$$\bar{y}_F = \int_0^\infty y \cdot f(y) \cdot dy$$

The same relation can be obtained for the dose, obtaining the dose-mean lineal energy:

$$\bar{y}_D = \int_0^\infty y \cdot d(y) \cdot dy$$

List of abbreviations

CPDS	Charged Particle Directional Spectrometer
CPE	Charged Particle Equilibrium
ER	Earth Radii
EuCPAD	European Crew Personal Active Dosimeter
EuCPD	European Crew Passive Dosimeter
EV	Extra-Vehicular
EVA	Extra-Vehicular Activities
GCR	Galactic Cosmic Ray
ICRP	International Commission on Radiological Protection
ISPR	International Standard Payload Rack
ISS	International Space Stationù
IV	Intra-Vehicular
LEO	Low Earth Orbit
LET	Linear Energy Transfer
MFC	Mass Flow Controller
PNTD	Plastic Nuclear Track Detector
PSD	Personal Storage Device
SAA	South Atlantic Anomaly
SPE	Solar Particle Event
STS	Space Transportation System
TEPC	Tissue-Equivalent Proportional Detector
TLD	Thermoluminescent Detector

References

[Alkaa, 2000] Alkaa, A. Bordage M.C. Cesari, P. Colautti, V. Conte, V. De Nardo, L. Segur, P. Magrin, G and Tornielli, G. A code for modelling cylindrical TEPCs. *Radiation quality assessment based on physical radiation interaction at nanometre* level. Ed. Colautti P. LNL-INFN report 161 (2000)

[Armstrong, 1998] T.W. Armstrong, B.L. Colborn, Science Applications International Corp. Repot No. SAIC-TN-9528 (1998)

[Armstrong, 2001] T.W. Armstrong, B.L. Colborn, Predictions of secondary neutrons and their importance to radiation effects inside the International Space Station. *Radiat. Meas.* 33 229-234 (2001)

[Attix, 1986] F.H. Attix, Introduction to radiological physics and radiation dosimetry, ed. *Wiley VCH* (1986)

[Badhwar, 1994] G.D. Badhwar, F.A. Cucinotta, P.M. O'Neill, An analysis of interplanetary space radiation exposure for various solar cycle. *Radiat. Res.* 138 201-208 (1994)

[Badhwar, 1997] G.D. Badhwar, The radiation environment in Low-Earth Orbit. *Radiat. Res.* 148 S3-S10 (1997)

[Badhwar, 2001] G.D. Badhwar, Radiation measurements on the International Space Station. *Physica Medica* vol. XVII supplement 1, 287-291 (2001)

[Badhwar, 2001] G.D. Badhwar, J.E. Keith, T.F. Cleghorn, Neutron measurements onboard the space shuttle. *Radiat. Meas.* 33 235-241 (2001)

[Badhwar, 2002] G.D. Badhwar, Shuttle radiation dose measurements in the International Space Station orbits. *Radiat. Res.* 157 69-75 (2002)

[Badhwar, 2002] G.D. Badhwar, W. Atwell, F.F. Badavi, T.C. Yang, T.F. Cleghorn, Space radiation absorbed dose distribution in a human phantom. *Radiat. Res.* 157 76-91 (2002)

[Badhwar, 2002] G.D. Badhwar, W. Atwell, G. Reitz, R. Beaujean, W. Heinrich, Radiation measurements on the Mir Orbital Station. *Radiat. Res.* 35 393-422 (2002)

[Benton, 2001] E.R. Benton, E.V. Benton, Space radiation dosimetry in Low-Earth Orbit and beyond. *Nuc. Inst. Meth. Phys. Res. B* 184 255-294 (2001)

[Berger, 2008] T. Berger, Radiation dosimetry onboard the International Space Station ISS. *Z. Med. Phys.* 18 265-275 (2008)

[Bottolier-Depois, 2002] J. F. Bottolier-Depois, M. Siegrist, V. M. Petrov, V. V. Shurshakov, V. Bengin, S.B. Koslova, TEPC measurements obtained oh the Mir space station. *Radiat. Meas.* 35 485-488 (2002)

[Braby, 1995] L.A. Braby, G.W. Johnson, J. Barthe, Practical considerations in the design and construction of tissue-equivalent proportional counters *Rad. Prot. Dos. 61* 351-379 (1995)

[Braby, 2008] L.A. Braby, D. Perez-Nunez, Design, construction, and implementation of spherical Tissue-Equivalent proportional counter. *Nuclear Technology* 168 21-28 (2008)

[Braby, 2010] L.A. Braby, D. Perez-Nunez, Replacement Tissue-Equivalent Proportional Counter for the International Space Station. *Rad. Prot. Dos.* (2010)

[Burlaga, 1991] L. Burlaga, F. McDonald. N. Ness, A. Lazarus, Cosmic ray modulation: Voyager 2 observations, 1987-1988. *J. Geophys Res.* 96 3789-3799 (1991)

[Cucinotta, 2006] F. A. Cucinotta, M. Durante, Cancer risk from exposure to galactic cosmic rays: implications for space exploration by human beings. *Lancet Oncol.* 7 431-435 (2006)

[Cucinotta, 2008] F.A. Cucinotta, Myung-Hee Y. Kim, V.Willingham, K.A. George, Physical and Biological Organ Dosimetry Analysis for International Space Station Astronauts. *Radiat. Res.* 170 127-138 (2008)

[Dettmann, 2007] J. Dettmann, G. Reitz, G. Gianfiglio, MATROSHKA-THe first ESA external payload on the International Space Station. *Acta Astronaut. 60* 17-23 (2007)

[Feynman, 1993] J. Feynman, G. Spitale, J. Wang, S.Gabriel, Interplanetary proton fluence model. J. Geophys. Res. 98 13281 (1993)

[Feynman, 1996] J. Feynman, S.B. Gabriel, High-energy charged particles in space at one astronomical unit. *IEEE Trans. On Nucl. Sci.* 43*, No. 2,* 344-352 (1996)

[Gabriel, 2003] S.B. Gabriel, G.J. Patrick, Solar energetic particle events: phenomenology and prediction. *Sp. Sci. Rev.* 107 55-62 (2003)

[Getselev, 2004] I. Getselev, S. Rumin, N. Sobolevsky, M. Ufimtsev, M. Podzolko, Absorbed dose of secondary neutrons from galactic cosmic rays inside the international space station. *Adv. Sp. Res.* 34 1429-1432 (2004)

[Heylen, 2000] Heylen A.E.D., The relationship between electron-molecule collision cross-sections, experimental townsend primary and secondary ionization coefficents and constants, electric strength and molecular structure of gaseous hydrocarbons. *Proceedings: Mathematical, Physical and Engineering Sciences,* 456 3005-3040 (2000)

[ICRP, 1978] International Commission on Radiological Protection, Recommendations of the International Commission on Radiological Protection, Report 26, Oxford: Pergamon Press (1978)

[ICRP, 1991] International Commission on Radiological Protection, Recommendations of the International Commission on Radiological Protection, Report 60, Oxford: Pergamon Press (1991)

[ICRU, 1970] Lineal Energy Transfer, Report 16, Washington DC: ICRU Publications (1970)

[ICRU, 1983] International Commission on Radiation Units and Measurements, Report 36, Microdosimetry (1983)

[IPE, 1988] J. Feynman, S. Gabriel, Interplanetary Particle Environment. Proceedings of a Conference. *JPL Publication 88-28* (1988)

[Kliauga, 1995] P. Kliauga, A.J. Waker, J. Barthe, Design of Tissue-Equivalent Proportional Counters. *Rad. Prot*. Dos. 61 309-322 (1995)

[Lee, 2007] K. Lee, J. Flanders, E. Semones, T. Shelfer, F. Riman, Simultaneous observation of the radiation environment inside and outside the ISS. *Adv. Sp. Res.* 40 1558-1561 (2007)

[Loncol, 1994] Loncol et al, Radiobiological effectiveness of radiation with broad let spectra: microdosimetric analysis using biological weighting functions. *Radiat. Prot*. *Dos*. 52 347-352 (1994)

[Lyagushin, 1998] V.I. Lyagushin, V.E. Dudkin, Y.V. Potapov, V.D. Savastianov, Proceeding of workshop, predictions, and measurements of secondary neutrons in space, Houston, TX, 28-30 September 2008

[Mewaldt, 1998] R.A. Mewaldt, Solar energetic particle composition, energy, spectra and space weather. *Sp. Sci. Rev*. 124 303-316 (2006)

[Mewaldt, 2006] R.A. Mewaldt, A.C. Cummings, J. Adams, O. Evenson, W. Fillius, J. Jokipii, R. McKibeen, P. Robinson, Toward a descriptive model of Galactic Cosmic Rays in the Heliosphere. *Interplanetary Particle Environment, JPL Publication*. 88-28 (1988)

[Mitev, 2005] Mitev K, Ségur P, Alkaa A, Bordage MC, Furstoss C, Khamphan C, De Nardo L, Conte V, Colautti P. Study of non-equilibrium electron avalanches, application to proportional counters. *Nuclear Instruments and Methods in Physics Research A* 538, 672-685 (2005)

[Moro, 2006] D.Moro. Development of Tissue Equivalent Proportional Counters for BNCT microdosimetry, PhD Thesis – University of Ferrara (2006)

[NCRP, 1989] National Council on Radiation Protection and Measurements, Guidance on Radiation Received in Space Activities. *Report Nr*. 98, Bethesda, MD

(1989)

[NCRP, 2000] National Council on Radiation Protection and Measurements, Radiation protection guidance for activities in Low Earth Orbit . *Report Nr*. 132, Bethesda, MD (2000)

[NGDC, 2001] NGDC (2001) National Geophysical Data Center on line archive. http://www.ngdc.noaa.gov/stp/GOES

[O'Sullivan, 2004] D. O'Sullivan, D. Zhou, E. Semones, W. Heinrich, E. Flood, Dose equivalent, absorbed dose and charge spectrum investigation in Low Earth Orbit. *Adv. Sp. Res.* 34 1420-1423 (2004)

[Rossi, 1959] H.H. Rossi, M. Zaider, Specification of radiation quality. *Radiat. Res*. 10 522-531 (1959)

[Rossi, 1991] H.H. Rossi, M. Zaider, Elements of microdosimetry. *Med. Phy*. 18(6) 1085-1092 (1991)

[Ségur, 1995] P. Ségur, P. Olko, P. Colautti, Numerical modelling of tissue-equivalent proportional counter. *Rad. Prot. Dos*. 61 323-350 (1995)

[Waker, 1995] A.J. Waker, Principles of experimental microdosimetry. *Rad. Prot*. Dos. 61 297-308 (1995)

[Wilson, 1995] J.W. Wilson, F.F. Badavi, F.A. Cucinotta, J.L. Shinn, G.D. Badhwar, HZETRN: Description of a free-space ion and nucleon transport and shielding computer programm, NASA TP 3495, Langley Research Center, Hampton, VA

(1995)

[Zhou, 2007] D. Zhou, E. Semones, M. Weyland, S. Johnson, Radiation measured with TEPC and CR-39 PNTDs in Low Earth Orbit. *Adv. Sp*. *Res*. 40 1571-1574 (2007)

[Zhou, 2008] D. Zhou, D. O'Sullivan, E. Semones, N. Zapp, S. Johnson, M. Weyland, Radiation dosimetry for high LET particles in Low Earth Orbit. *Act. Astro*. 63 855-864 (2008)